Zero-Echo Time MR imaging of the pelvis as prior for PET reconstruction

Febe Brackx

Supervisor: Prof. dr. Stefaan Vandenberghe
Counsellor: Ester D'Hoe

Master's dissertation submitted in order to obtain the academic degree of
Master of Science in Biomedical Engineering

Department of Electronics and Information Systems
Chair: Prof. dr. ir. Rik Van de Walle
Faculty of Engineering and Architecture
Academic year 2016-2017

GHENT
UNIVERSITY

Zero-Echo Time MR imaging of the pelvis as prior for PET reconstruction

Febe Brackx

Supervisor: Prof. dr. Stefaan Vandenberghe
Counsellor: Ester D'Hoe

Master's dissertation submitted in order to obtain the academic degree of
Master of Science in Biomedical Engineering

Department of Electronics and Information Systems
Chair: Prof. dr. ir. Rik Van de Walle
Faculty of Engineering and Architecture
Academic year 2016-2017

GHENT
UNIVERSITY

Acknowledgements

Medical imaging has always been a strong interest of mine. It amazes me how we can reach further and further, and help more and more patients. It is a field where so many sciences join together: physics, chemistry, biology, informatics, electronics,... All of these play an important role in acquiring the images that can eventually help us save lives. Doing a thesis on PET/MR imaging, a new multimodal imaging modality that has not yet been established in daily clinical settings, was therefore a chance I didn't want to miss.

This master dissertation is the result of one year of work, and it would not have been possible without the help of some people. First of all, I would like to thank my counselor Ester, who has helped me throughout the process, provided useful insights, gave feedback and joined me on trips to Gasthuisberg. Secondly, I want to thank my promotor, professor Stefaan Vandenberghe, for the support and the opportunity. A special thanks goes to my boyfriend Dennis, who had my back at all times, showed sincere interest in what I was working on and solved most of my computer-related issues. Without him, my computer would probably have exploded. Finally, I want to thank my friends and family for the support and love I received in this very interesting but challenging year.

Zero-Echo Time MR imaging of the pelvis as prior for PET reconstruction

Febe Brackx

Supervisor: Prof. dr. Stefaan Vandenberghe
Counselor: Ester D'Hoe

Master's dissertation submitted in order to obtain the academic degree of Master of Science in Biomedical Engineering

Department of Electronics and Information Systems
Chair: Prof. dr. ir. Rik Van de Walle
Faculty of Engineering and Architecture
Academic year 2016-2017

Abstract

Recent work has shown that in brain imaging, the ZTE intensity of bone voxels is inversely proportional to the bone density. Therefore, it can be used to obtain a continuous patient-specific pseudo-CT of bone tissue. In this work, we aim at testing whether including the ZTE sequence in pelvic PET/MR protocols can improve the attenuation correction step and therefore the PET reconstruction. At first, the ZTE sequence was adapted to pelvic imaging. Due to limited access to the parameters of the sequence and the fact that the sequence is optimized for brain imaging only, no ZTE pelvic images with sufficient contrast were obtained. This complicated the process of image segmentation, where an algorithm based on symmetry and similarity values was implemented in Matlab, but no sufficiently good bone masks were obtained. Two case studies were done to investigate the relationship between ZTE and CT intensities in bone voxels: one study on a cervical patient and one study on a pig bone. In both cases, it was concluded that the inversely proportional relationship between CT and ZTE intensities for bone voxels is clear, but a larger clinical study is needed to obtain a reliable two-segment model that can be applied on new datasets.

Zero-Echo Time MR imaging of the pelvis as prior for PET reconstruction

Febe Brackx

Supervisor(s): Stefaan Vandenberghe, Ester D'Hoe

Abstract—**In this work, we aim at testing whether including the ZTE sequence in pelvic PET/MR protocols can improve the attenuation correction step and therefore the PET reconstruction.**

Keywords—**PET/MR imaging, Zero-Echo Time, bone segmentation, attenuation correction**

I. INTRODUCTION

THE work presented in this paper is situated in the field of multimodal medical imaging, more specifically the combination of PET imaging and MR imaging (simultaneous PET/MR imaging).

MRI (Magnetic Resonance Imaging) is a medical imaging technique that offers high resolution and superior soft tissue contrast, without administering ionizing radiation to the patient. By applying magnetic fields and acquiring radio-frequency signals from protons, a 3D anatomical image can be obtained.

PET imaging (Positron Emission Tomography) is a functional imaging technique used to visualize metabolic processes in the body. A positron-emitting radionuclide, called the tracer, is linked to a biologically active molecule and administered to the patient. The labeled molecules are distributed throughout the body and taken up in certain cells or organs. Gamma cameras detect pairs of 511 keV photons emitted when a positron annihilates. Using image reconstruction techniques, a 3D image of the distribution of the biological molecule can be obtained.

A PET/MR scanner combines the functional information obtained by PET imaging and the anatomical information obtained by MR imaging. The technical challenges to integrate both imaging modalities have been overcome the past years and the first PET/MR scanner in Belgium is installed in the university hospital of Leuven. Nevertheless, research is still ongoing on how a major artifact of PET imaging, the attenuation of the 511 keV photons, can be overcome in an efficient and accurate way. The attenuation map, which contains the distribution of attenuation coefficients throughout the imaging volume, can be derived in different ways. In a simultaneous PET/CT scanner, the attenuation map can easily be obtained from the CT image, since both attenuation coefficients and CT intensities are related to the electron density. In simultaneous PET/MR, this is a more challenging task, since MR intensities are related to proton density and relaxation properties. One possibility is to label different regions in the image based on MR intensity (image segmentation) and assign a predefined attenuation value to the different tissue types. This can be done without making assumptions on the anatomy of the patient. A major drawback of the segmentation methods is the inability to account for inter-patient variability and variations of the attenuation coefficients within one tissue type in the body. Another problem is that lung tissue and cortical bone are not visible on images acquired with conventional MR sequences and are therefore hard to distinguish.

Dedicated MR sequences have been developed that make visualization of bone and lung tissue possible. One of them is the Zero-Echo Time sequence (ZTE), shown in figure 1 ([1]), which is designed to start acquisition of the signal as fast as possible after the excitation RF pulse. Recent research ([2], [3]) has shown that the signal intensity of bone in ZTE images is inversely proportional to the bone density and can directly be linked to the corresponding Hounsfield unit. Therefore, ZTE images can be used to obtain a continuous patient-specific pseudo-CT in bone tissue.

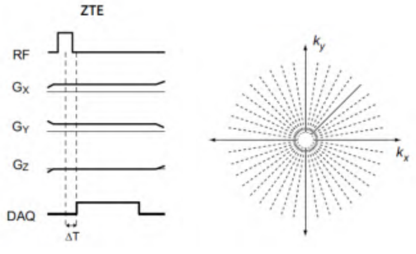

(a) (b)

Fig. 1. (a) A single repetition time of the ZTE sequence, (b) the corresponding k-space coverage.

PET/MR imaging has been used mostly in brain imaging, where attenuation correction techniques are well developed and applied. Therefore, in this work, the focus is on another body part: the pelvis. This is a region with a high portion of bones and therefore accurate attenuation correction is crucial. Among others, PET/MR imaging in the pelvic region has been applied for patients with prostate cancer, gynecologic cancer, and rectal cancer. The goal of this work is to obtain ZTE images of the pelvis with sufficient contrast, using the integrated 3 tesla TOF PET/MRI system (SIGNA PET/MR, GE Healthcare, Waukesha, WI, USA), to develop a method that is able to segment bone from pelvic ZTE images and to verify that for bone voxels, the ZTE intensity is indeed inversely proportional to the CT intensity.

II. DATA ACQUISITION

Since no ZTE hip images were acquired before at the PET/MR scanner in Leuven, the first step was to optimize the ZTE sequence parameters in order to obtain an acceptable image quality. Since the ZTE sequence is designed for head imaging and only a few parameters were adaptable, a lot of difficulties were met during this process. It was concluded that, using the

ZTE sequence from GE and a body coil to acquire the image, it was not possible to obtain a ZTE image with sufficient contrast. This is shown in figure 2, where a pelvic ZTE slice is shown with an isotropic resolution of 2 mm. It is clear that the head of the femur cannot be differentiated from the surrounding soft tissue. When a pig bone was scanned using a head coil with a resolution of 1 mm and NSA (Number of Signal Averages) set to 16, images with good quality were obtained. This is shown in figure 3.

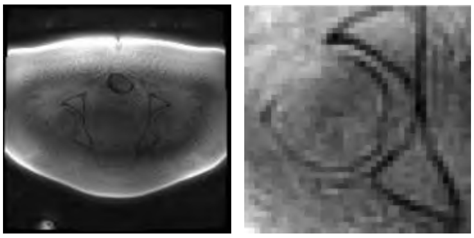

(a) (b)

Fig. 2. (a) Slice of a pelvic ZTE image with isotropic resolution of 2 mm, (b) zoom-in on a bone structure with low contrast.

Fig. 3. ZTE image of a pig bone with a resolution of 1 mm and NSA = 16. The image is acquired with the head coil.

III. ZTE BONE SEGMENTATION

The low quality pelvic ZTE images complicated the process of bone segmentation. A number of different segmentation methods were implemented. When applying simple thresholding or thresholding in combination with image enhancement techniques, the number of wrongly segmented pixels was too large to further use the results. Also the use of Markov random fields and multiscale edge detection led to insufficient results. The best bone segmentation was obtained by an algorithm based on symmetry and similarity information from bone regions. This idea was based on the fact that bone structures in general are symmetric while air cavities are not. The downside of this method is that asymmetric anatomical abnormalities in bone will be classified as air instead of bone, which makes it less generally applicable. After image enhancement and thresholding, the different objects in the binary image are separated. For each object, the symmetry, similarity, size and distance to the edge of the body are taken into account. The symmetry measure is obtained by flipping the image in the left-right direction and calculating the number of overlapping pixels. The similarity measure is obtained by calculating the maximum of the 2D cross-correlation. This way, objects with similar shapes can be recognized as bone, regardless of symmetry. Due to the low contrast between bone tissue and soft tissue in some regions, it was concluded that none of the mentioned segmentation methods provided sufficiently good results. An example is shown in figure 4.

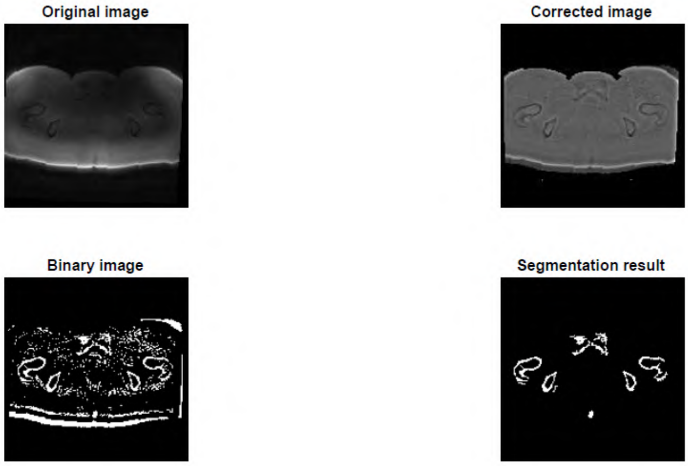

Fig. 4. The symmetry- and similarity-based segmentation algorithm applied on a pelvic ZTE image.

IV. CASE STUDIES

Two case studies were done to verify the inversely proportional relationship between ZTE and CT intensity in bone voxels and to see if it is possible to obtain an attenuation map purely based on MR images. In both cases, the CT-based attenuation map was used as reference. The first dataset was from a cervical patient. For image registration, the built-in Matlab functions, the MIRT package and the ITK toolbox were applied. Since we were dealing with multimodal imaging, multimodal image registration needed to be applied. As similarity metric, mutual information was used. None of these methods provided a good registration result; this because the patient walked from the PET/CT to the PET/MR scanner and the two beds have a different shape. To overcome this problem, similar slices were manually selected, bone was segmented and 2D image registration was applied on the binary bone masks. Eventually, 31 slices were selected to obtain the relationship between ZTE and CT intensities in bone voxels. The Shape Language Modelling toolkit (SLM) was used to fit a continuous two-segment piecewise linear model to the joint histogram of this subset. This model was used to calculate a pseudo-CT from the ZTE data for bone voxels. From the pseudo-CT, a 511 keV attenuation map was obtained by applying a bilinear transformation. The root-mean-squared error between the CT-based attenuation map and ZTE-based attenuation map for bone pixels was 8.94%, which is large compared to the errors presented in [3] (4.64%). Due to the limited amount of data available, the results cannot be used to draw general conclusions on the relation between ZTE and CT bone intensities.

A second case study was done on the leg of a dead pig. Since the bone parts in the leg of the pig have a simple geometry, 3D image registration was possible. For the bone pixels, a continuous two-segment piecewise linear model was fitted in a similar way as the human dataset. The fit is shown in figure 5. For non-bone pixels, the pseudo-CT was obtained by calculating water-fat fractions from Dixon images. 511 keV attenuation coefficients were calculated from the pseudo-CT using a bilinear transformation. The CT-based attenuation map and the MR-based attenuation map are shown for one slice in figure 6. The root-mean-squared error between the CT-based attenuation map and ZTE-based attenuation map for bone pixels was 12.864%, which is again large compared to the errors presented in [3]. In general, the results obtained in from this study are a proof-of-principle and cannot be used directly to draw conclusions about the use of ZTE in human PET/MR imaging. First of all, the pig was dead for about a week when the images were made. This led to higher bone densities and different tissue properties. Secondly, a head coil was used instead of a body coil, which resulted in higher image quality. Finally, the limited size of the bone enabled ZTE images with higher resolution, which facilitated image processing.

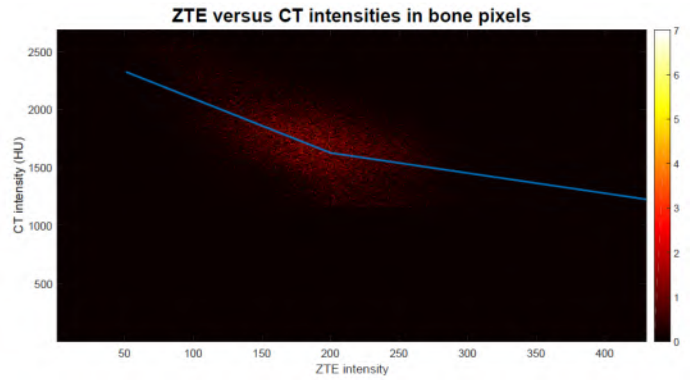

Fig. 5. A continuous two-segment piecewise linear model is fitted to the joint histogram of the ZTE and the CT bone intensities.

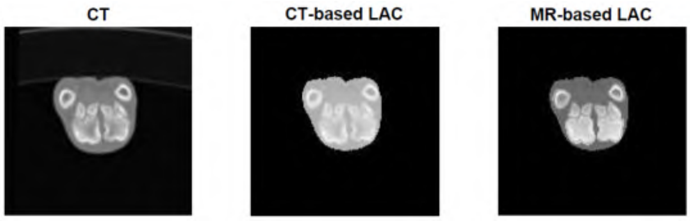

Fig. 6. The CT image, CT-based attenuation map, and MR-based attenuation map for one slice of a pig bone.

V. CONCLUSION

It can be concluded that the use of the ZTE sequence can result in more accurate attenuation maps, and therefore shows a lot of potential for implementation in PET/MR pelvic imaging. Nevertheless, the sequence that is currently used in the university hospital in Leuven is optimized for brain imaging only and provides insufficient image quality when used in the pelvic region. Further collaboration with GE, the vendor of the clinical scanner, is needed in order to obtain good image quality to further investigate the full potential of the ZTE sequence and its applications in pelvic PET/MR imaging.

REFERENCES

[1] Peder EZ Larson, Misung Han, Roland Krug, Angela Jakary, Sarah J Nelson, Daniel B Vigneron, Roland G Henry, Graeme McKinnon, and Douglas AC Kelley, Ultrashort echo time and zero echo time mri at 7t. *Magnetic Resonance Materials in Physics, Biology and Medicine,* pages 1-12, 2015.

[2] Tetsuro Sekine, Edwin EGW ter Voert, Geoffrey Warnock, Alfred Buck, Martin W Huellner, Patrick Veit-Haibach, and Gaspar Delso, Clinical evaluation of zte attenuation correction for brain fdg-pet/mr imaging— comparison with atlas attenuation correction. *Journal of Nuclear Medicine,* pages jnumed-116, 2016.

[3] Andrew P Leynes, Jaewon Yang, Dattesh D Shanbhag, Sandeep S Kaushik, Youngho Seo, Thomas A Hope, Florian Wiesinger, and Peder EZ Larson, Hybrid zte/dixon mr-based attenuation correction for quantitative uptake estimation of pelvic lesions in pet/mri. *Medical Physics,* 2017.

Contents

List of acronyms

A

AC	Attenuation Correction
APD	Avalanche photodiodes

B

BPH	Benign Prostatic Hyperplasia

C

CT	Computed Tomography

D

DCE	Dynamic Contrast Enhanced
DRE	Digital Rectal Examination
DWI	Diffusion Weighted Imaging

F

FDG	Fluorodeoxyglucose
FID	Free Induction Decay
FOV	Field-Of-View

G

GE	Gradient Echo

H

HU	Hounsfield Unit

I

ITK	Insight segmentation and registration toolbox

L

LSO	lutetium oxyorthosilicate
LYSO	lutetium-yttrium oxyorthosilicate

M

MICO	Multiplicative Intrinsic Component Optimization
MLAA	Maximum Likelihood reconstruction of Attenuation and Activity
MR	Magnetic Resonance
MRI	Magnetic Resonance Imaging
MRS	Magnetic Resonance Spectroscopy

P

PD	Proton Density
PET	Positron Emission Tomography
PMT	Photomultiplier tubes
PSA	prostate-specific antigen
PSMA	Prostate Specific Membrane Antigen

R

RF	Radio Frequency
RMSE	Root-mean-squared error

S

SFCM	Spatial fuzzy c-means
SNR	Signal-to-noise ratio
STE	Short Echo Time
SUV	Specific Uptake Value
SV	Similarity Value

T

TOF	Time-Of-Flight
TR	Repetition Time
TRUS	Transrectal Ultrasound
TSE	Turbo Spin Echo

U

UTE	Ultrashort Echo Time

Z

ZTE	Zero-Echo Time

Chapter 1

Introduction

1.1 Situation

The work presented in this master dissertation is situated in the field of multimodal medical imaging, more specifically simultaneous PET/MR imaging. MRI (Magnetic Resonance Imaging) is a medical imaging technique where no ionizing radiation is applied to the patient and a wide range of contrasts can be obtained. PET imaging (Positron Emission Tomography) is a functional imaging technique used to visualize metabolic processes in the body. A PET/MR scanner combines the functional information obtained by PET imaging and the anatomical information obtained by MR imaging. In 2015, the first Belgian PET/MR scanner was installed in the university hospital of Leuven. Nevertheless, research is still ongoing on how a major artifact of PET imaging, the attenuation of the 511 keV photons, can be overcome in an efficient and accurate way. One option is to do image segmentation, where different regions are labeled differently, based on their intensity, and a predefined attenuation value is assigned to the different tissue types. One of the problems of segmentation-based attenuation correction using MR images, is the fact that lung and cortical bone tissue are not visible on conventional MR images and are therefore hard to distinguish. Dedicated MR sequences have been developed to make visualization of bone and lung tissue possible. One of them is the Zero-Echo Time sequence (ZTE), which is designed to start acquisition of the signal as fast as possible after the excitation RF pulse. It has been shown that the intensity of bone voxels in brain ZTE images is inversely proportional to bone density and can therefore be linked to the intensity in CT images. When this relationship can be derived, ZTE images can be used to obtain a continuous patient-specific pseudo-CT in bone tissue.

PET/MR imaging has been used mostly in brain imaging, where attenuation correction techniques are well developed and applied. Therefore, in this thesis, the focus is on another body part: the pelvis. This is a region with a high portion of bones and therefore accurate attenuation correction is crucial. Among others, PET/MR imaging in the pelvic region has been applied for patients with prostate cancer, gynecologic cancer, and rectal cancer. The goal of this thesis is to obtain ZTE images of the pelvis with sufficient contrast, using the integrated

3 tesla TOF PET/MRI system (SIGNA PET/MR, GE Healthcare, Waukesha, WI, USA), to develop a method that is able to segment bone from pelvic ZTE images and to verify that for bone voxels, the ZTE intensity is indeed inversely proportional to the CT intensity.

1.2 Outline

In chapter 2, a general introduction is given on PET imaging, MR imaging and simultaneous PET/MR imaging. In the first section on PET imaging, the principle of tracer imaging is discussed, together with the components of gamma detectors and the workings of current PET scanners. Also the different imaging degrading effects are shortly explained. In the section on MR imaging, an introduction is given on the spin physics behind MR, the imaging principles, the hardware components and the applications of MRI. In the section on simultaneous PET/MR imaging, the focus is on attenuation correction and the different methods to do so.

In chapter 3, segmentation-based attenuation correction is discussed. Specialized MR sequences have been developed in order to discriminate different tissue types based on their MR intensities. First of all, the requirements for these methods are discussed. Secondly, the different challenges that occur during segmentation are presented. Additionally, three different MR sequences that are used for segmentation are discussed.

As already explained, the focus of this thesis is on ZTE imaging of the pelvis and its use for attenuation correction. PET/MR imaging in the pelvic region has been applied for patients with prostate cancer, gynecologic cancer, and rectal cancer. These applications and the current status of pelvic PET/MR imaging are given in chapter 4.

In chapter 5, the different datasets that were obtained are discussed. The MR datasets are acquired by the integrated 3 tesla TOF PET/MRI system (SIGNA PET/MR, GE Healthcare, Waukesha, WI, USA) in the university hospital of Leuven, using a body coil. By altering the parameters of the ZTE sequence while a volunteer was in the scanner, the image quality was optimized.

Image registration is an essential step before the CT and ZTE datasets can be compared. This is discussed in chapter 6. Multimodal 2D and 3D image registration is applied and mutual information is used as similarity metric. A wide range of image registration techniques exist and multiple software packages and toolboxes provide this option. In this thesis, the built-in Matlab registration functions, the MIRT package and the ITK toolbox were applied.

In chapter 7, the different segmentation methods are described to obtain a bone mask from the ZTE pelvic images. At first, two bias field correction techniques are explained and compared. Then, 5 image segmentation methods are described: thresholding, thresholding after image enhancement, Markov random fields, multiscale edge detection and finally symmetry and similarity based segmentation.

Two case studies are set up to verify that the ZTE and CT intensities of bone voxels are inversely proportional, to obtain an MR-based attenuation map and to compare this to a CT-based attenuation map. The first case study is on a human pelvic dataset, where only a small subset of the slices can be used due to failed image registration. The second case study is on a pig bone dataset, where 3D image registration was possible due to the simple geometries. Both are described in chapter 8.

A summary of the conclusions and future work are given in chapter 9.

Chapter 2

Multimodal imaging

2.1 PET imaging

2.1.1 Introduction

Positron Emission Tomography (PET) is a functional imaging technique used to visualize metabolic processes in the body. The obtained image shows the distribution of a certain molecule in the Field-Of-View (FOV). A positron-emitting radionuclide, called the tracer, is linked to a biologically active molecule and administered to the patient. The labeled molecules are distributed throughout the body and taken up by certain cells or organs. Gamma cameras detect pairs of photons emitted when a positron annihilates. Using image reconstruction techniques, a 3D image of the distribution of the biological molecule can be obtained. PET imaging is often used in the field of cancer detection and follow-up. Spatial and temporal resolution of PET images are lower than most other imaging modalities, but this is compensated by a higher sensitivity (in the order of picomolars). During a standard PET exam, a radiation dose of 3 to 20 mCi is administered to the patient.

2.1.2 Positron emitters

Radioisotopes used in PET imaging are positron emitters: a β^+-particle, or a positron, is emitted during decay. Positron emitters are characterized by an excess of protons. The decay scheme of β^+-decay is as follows:

$$^{A}_{Z}X \longrightarrow {}^{A}_{Z-1}X + e^+ + \nu_e$$

The isotope emits the positron with a certain kinetic energy. The positron then travels a random path and loses its energy in atomic collisions. When it has lost most of its kinetic energy, the positron will annihilate with an electron, its antiparticle, and two photons are emitted in opposite direction. These photons both have an energy of 511 keV, which can be derived using Einstein's formula $E = mc^2$.

^{18}F,^{13}N, ^{15}O and ^{11}C are the most used positron emitters. ^{18}F is for instance used in oncology to image tumors and to search for metastasis. It is bound to fluorodeoxyglucose (FDG), which is a glucose analog. Cancer cells are characterized by a higher glucose uptake and therefore tumors or metastasis appear bright on a PET image.

The positron emitters used in PET imaging are produced in a cyclotron, where stable nuclei are bombarded with protons. The most important practical disadvantage of most PET isotopes for clinical use is the short half-life, which makes production on site necessary. Only ^{18}F, with a half-life of 109.8 minutes, can be produced outside of the hospital.

2.1.3 Gamma detectors

The photon pairs emitted during PET imaging are detected by gamma cameras. A schematic drawing of such a camera is shown in figure 2.1. The gamma cameras consist of three layers. The first layer is a scintillation crystal, where the photon is converted into a visible light pulse. The intensity of the light pulse is proportional to the energy of the incoming photon. When designing the scintillation layer, a trade-off is made between stopping power and light output. The thicker the crystal, the higher the stopping power but the lower the light output. A fast rise time and the absence of afterglow allow high counting rate. NaI, CsI, lutetium oxyorthosilicate (LSO) and lutetium-yttrium oxyorthosilicate (LYSO) are commonly used scintillation materials. The second layer is a light guide, which spreads the light pulses to the third layer, the photomultiplier, where the light pulses are converted to an electric signal. Because photomultipliers are much larger than the crystals, Anger logic is used to obtain the two dimensional position of the incidence of the photon. Photomultiplier tubes (PMT's) are often used in stand-alone PET scanners. In more advanced PET systems, it is often possible to measure energy, time and depth of the scintillation in the crystal.

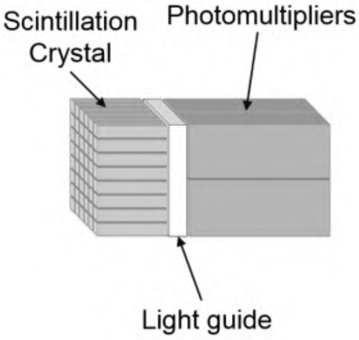

Figure 2.1: A gamma camera. [1]

2.1.4 PET scanners

Current PET scanners consist of a number of full rings of gamma detectors. Recall that annihilation of a positron and electron causes the emission of two 511 keV photons in opposite direction. Therefore, it can be assumed that the annihilation point is somewhere on the line connecting the two detection points (colinearity) and that the two photons arrive at the detector ring more or less at the same moment in time (simultaneity). When a first photon is detected, a coincidence circuit is opened. An event or coincidence is registered only if another photon is detected within a very short time. By acquiring a large number of events, an image can be formed by applying reconstruction techniques. Current PET scanners operate in full 3D mode, which means that coincidences can be detected between different rings. This increases the sensitivity, but also the amount of image degrading effects. Nowadays, the information on the time difference between two detections can be used to make an estimation on the position of the annihilation along the path. This is called Time-Of-Flight (TOF) PET and is made possible by fast PMTs, high density scintillators, modern electronics and higher computing power [2]. Using TOF in a clinical setting significantly improves the image quality. The principle of TOF is shown in figure 2.2.

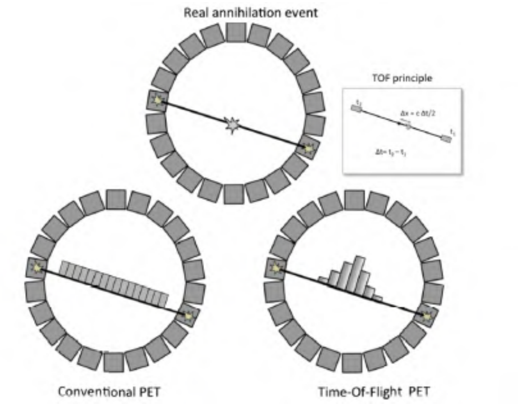

Figure 2.2: In non-TOF PET imaging, no information is known on the location of the event along the path of the photons. In TOF PET, an estimation Δt of the time difference between arrival of the two photons is made. This can be used to calculate the position of the annihilation by the formula $\Delta x = \frac{c\Delta t}{2}$. [2]

2.1.5 Image degrading effects

Attenuation

The 511 keV photons have to travel a certain distance through the body before they reach the detector ring, and therefore have a chance to undergo attenuation. This attenuation effect is more pronounced for the center of the body, since the photons that are emitted there have to travel a longer distance. The probability that a photon will be attenuated when passing through a unit thickness is called the attenuation coefficient $\mu(cm^{-1})$. Correcting for the attenuation effect is a necessary step in the reconstruction phase to obtain an image with acceptable quality. The attenuation map, which contains the distribution of attenuation coefficients throughout the imaging volume, can be derived in different ways [3]. In stand-alone PET, an extra transmission source can be used. In a simultaneous PET/CT scanner, the attenuation map can easily be obtained from the CT image. In simultaneous PET/MR, this is a more challenging task. More details on attenuation correction will be given in the next chapter.

Partial volume effect

The limited spatial resolution of a PET image leads to degradation of the image quality and is caused by different effects, together called the partial volume effect. In current PET systems, the detectors are the dominant factor, due to their relatively large size (4-6 mm). The scattering and light spread within the crystals that can lead to mispositioning as well. Additionally, the depth-of-interaction in the crystal is not measured, which further degrades the spatial resolution. Furthermore, there are limitations on spatial resolution caused by the physical principle of PET. First of all, the positrons that are emitted by the tracer travel a certain distance (≈ 1 mm for ^{18}F) before annihilation. Secondly, the photons will not be emitted in exactly opposed directions due to conservation of momentum.

Scattered and random coincidences

Compton scattering in the body can lead to detection of a wrong coincidence, since one of the photons has deviated from its path. In theory, it is possible to differentiate between real coincidences and scattered coincidences based on the energy of the detected photons, but limitations on energy resolution don't always allow to do this perfectly. To minimize the number of scattered coincidences, only photons that fall within a certain energy window are accepted. Random coincidences are detected when two separate annihilations each contribute a single photon which are both detected within the coincidence time window. The higher the activity within the patient, the higher the amount of random coincidences. Both scattered and random coincidences are estimated and corrected for in the reconstruction algorithm.

Countrate

The process of scintillation and calculation of the position and energy requires a certain time, called the dead time (30-200 ns). When other photons arrive within this dead time in a non-paralyzable detector, the system will register one single photon with an energy that falls outside of the energy window. This count rate loss is only important at high count rates and needs to be corrected, especially when quantification of the results is necessary. In a paralyzable detector, an event happening during the dead time is detected, but will restart the dead time. At high count rate, the detector will reach a saturation point where further detection of events is not possible. A semi-paralyzable detector exhibits an intermediate behaviour.

2.2 MR imaging

2.2.1 Spin physics

The physics behind MR imaging (Magnetic Resonance) is based on a quantum mechanical property called the spin angular momentum. Protons, neutrons and electrons all have a spin angular momentum and the total spin angular momentum of an atomic nucleus is determined by the spins of its protons and neutrons. Since the spin of a nucleus is used in MR imaging, only nuclei that posses spin can be imaged. ^{1}H (or a proton) is abundant in the human body and has spin 1/2, hence the main signal in MR imaging is coming from protons.

When an external magnetic field B_0 is applied, the protons will experience a torque. Due to the rules of quantum mechanics, the spins cannot align with the external magnetic field completely, but will precess around the axis of B_0 with a precessional frequency $\omega_0 = \gamma B_0$, where ω_0 is called the Larmor frequency and γ is the gyro-magnetic ratio. This is called the resonance condition, since all protons precess at the same frequency. There are two possible quantum states: protons in the spin-up state are almost aligned with $\overrightarrow{B_0}$, protons in the spin-down state are almost aligned opposite to $\overrightarrow{B_0}$. Both states are stable, but the spin-up state requires a little less energy than the spin-down. The number of protons in both states is determined by the Boltzmann distribution. Note that the quantum state of a proton will always be a linear combination of both possible states and dividing the spins in spin-up and spin-down is only a simplistic representation of reality.

Protons can switch between spin-up and spin-down state by gaining or losing a certain amount of energy in the form of a photon. This energy can be applied by electromagnetic radiation. The energy difference between the two states is proportional to the external magnetic field (Zeeman effect). It is found that the frequency of the electromagnetic field required to switch states is $\omega_0 = \gamma B_0$. Therefore, the precessional frequency of the protons is the same as the frequency of radiation required to switch states. In MRI systems, radio frequency (RF) waves are used.

Many individual spins add up to the net magnetization $\overrightarrow{M}$, which is aligned with $\overrightarrow{B_0}$. When $\overrightarrow{M}$ is aligned with $\overrightarrow{B_0}$, it cannot be measured since $\overrightarrow{B_0}$ is often 3 or 7 T, while $\overrightarrow{M}$ is in the order of μT. Therefore, an RF pulse at the Larmor frequency is used to flip the magnetization (partially) into the transverse plane. Using a detector which only measures the transverse magnetization, $\overrightarrow{M}$ is now a significant signal that can be recorded.

After the RF pulse, relaxation takes place. The net magnetization vector will gradually return to its equilibrium state and the measured signal in the receiver coil decays. This is called the Free Induction Decay (FID), and is governed by two phenomena: spin-spin relaxation and spin-lattice relaxation. When the magnetization is in the transverse plane, all spins are in-phase (this is called phase-coherence). Spin-spin relaxation causes a dephasing of the spins and a reduction in the transverse magnetization. It is caused by interactions between spins as they move around. These interactions cause small differences in the local magnetic field, therefore changing the precessional frequency of the spins and causing dephasing. Spin-spin relaxation is characterized by relaxation time T_2. Spin-lattice relaxation on the other hand can be thought of as the protons getting back in thermal equilibrium with their environment. As the protons lose their energy, the longitudinal magnetization is recovered. This process is characterized by relaxation time T_1. The T_1 and T_2 relaxation is shown in figure

2.3.

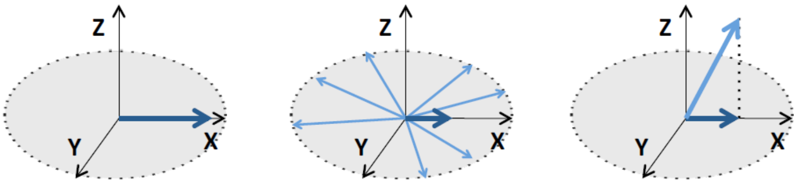

Figure 2.3: At the left, the magnetization is shown after a 90°RF pulse. In the middle, the T_2 relaxation is shown: small differences in local magnetic field cause dephasing of the spins and a decrease of the transverse magnetization. At the right, T_1 relaxation is shown: spins lose their extra energy and the initial number of protons in spin-up state is recovered.[3]

2.2.2 Imaging principle

In order to obtain an image, position-dependent information needs to be added to the signal.

Volume selection

By applying a linear gradient along the axis of the static magnetic field B_0 (z-axis), one volume slice can be selected. Since the magnetic field varies along the z-axis, the Larmor frequency also varies along the z-axis and therefore one slice can be excited.

k-space theorem

Spatial encoding within one slice is based on the k-space theorem, which is explained in every course on MRI, for example [4]. This theorem shows that by applying an inverse 3D Fourier transform, an image can be reconstructed from the recorded signal. The spatial frequency domain is called k-space and can be filled by manipulating the gradients.

MRI sequences

The signal acquired in MRI is dependent on the protons and their environment (proton density, relaxation properties and local field inhomogeneities), and the magnetic fields generated by the MR system (static magnetic field, gradient fields and RF excitation pulses). A large number of contrasts can be obtained by manipulating the RF and gradient fields. The signal that is transmitted by the spins after excitation quickly decays and is not sufficient to sample the entire k-space. Therefore, the spins are re-phased, thereby creating an echo. The main principles in which re-phasing is done are called spin echo and gradient echo. An explanation on these principles can be found in every course on MRI.

2.2.3 MRI hardware

In this section, the different hardware components that generate the magnetic fields are discussed.

- B_0 static magnetic field: this field is in most systems generated by a superconducting magnet. Currently, most clinically used MR systems have a static magnetic field of 1.5 or 3 Tesla.
- B_1 gradient fields: The gradient fields that are used for positioning encoding are generated by 3 perpendicular pairs of coils.
- RF excitation pulses: Both transmission and reception of signals is done by RF coils. A large integrated body coil is present in every MR system, but they are mostly used for excitation since specific RF coils exist for different body parts (brain, neck, chest, knee,...). These coils are much closer to the body and therefore obtain better signal quality.

The components that generate the magnetic fields are shown in figure 2.4.

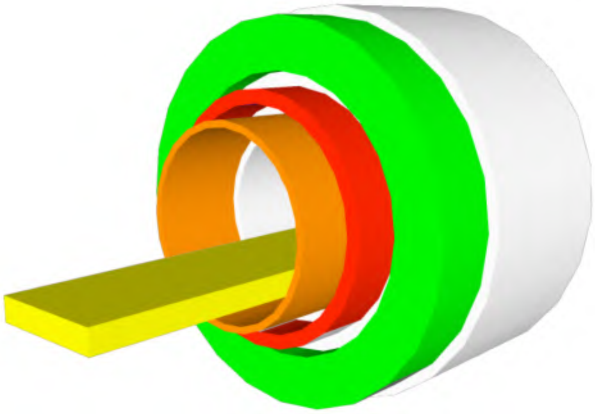

Figure 2.4: A cut through of an MRI scanner. Green: static magnet, red: gradient coils, orange: RF coils. [3]

2.2.4 Applications

MR imaging has a wide range of application, thanks to the excellent soft tissue contrast, the absence of ionizing radiation, the possibility to do functional imaging and the many different contrast possibilities. It is widely used in areas such as oncology, neurology and cardiology.

2.3 PET/MR imaging

The idea of combining PET and MR imaging was first suggested in 1990. The motivation was partly due to the success of PET/CT modalities, which provided a clear benefit in various applications but at the expense of a relatively high radiation dose. Since MR imaging does not apply ionizing radiation to the patient, has superior soft tissue contrast and provides the option of functional imaging (eg. fMRI, spectroscopy, diffusion weighted imaging), research on integration of PET and MR systems started. The first step was to fuse PET and MR data using dedicated registration software, but problems were encountered due to patient positioning and moving. Consequently, a PET and an MR scanner were placed in the same room and patients were imaged by the two scanners consecutively by moving the bed. This solution led to lengthy imaging protocols and the risk of misalignment due to patient motion in between the two imaging modalities was still present [5]. Before the development of a fully integrated PET/MR scanner was possible, a number of challenges needed to be overcome, on hardware level as well as software level. Both are described in this section. On software level, attenuation correction is the most important challenge and research is still ongoing on how this can be done effectively and accurate.

2.3.1 Technical challenges

Stand-alone PET and MR scanners both have an inner bore diameter of 60-80 cm, which made integrating both systems a challenging task. This integration was made possible by reducing the size of the PET detectors. During simultaneous operation, the PET hardware and MRI hardware affect each other. The PET system is affected by the static magnetic field, the rapidly changing gradient fields and RF interference of the MRI system. The magnetic field severely degrades the functioning of PMTs, since it changes the path of the electrons. Robust solid-state photodetectors such as the avalanche photodiodes (APDs) and silicon photomultipliers (SiPMs) have proven to function in a simultaneous PET/MR system. The gradient fields can induce Eddy currents in conducting components and can cause heating and mechanical vibrations. Redesigning the PET readout system minimized these effects. RF interference can be solved by enclosing the PET electronics in a conducting shield, since shielding is much more effective at high frequencies. To avoid susceptibility artifacts and maintain a homogeneous magnetic field, only nonmagnetic materials can be used for the PET electronics. Interference within digital electronics can cause RF signals that severely distort the measured signal in the receiver coils and thereby the final image. Therefore, the shielding of the electronics needs to happen with great care.

2.3.2 Attenuation correction

As described in the previous section, the attenuation of the 511 keV photons in PET imaging is a major artifact which has to be corrected for. This is done by deriving an attenuation map, which contains the distribution of attenuation coefficients throughout the imaging volume [3]. While this is straightforward in PET/CT imaging, there is no direct link between the measured MR signals and the attenuation coefficients in PET/MR imaging. Therefore, a large number of attenuation correction methods have been developed and tested, which are described below. An overview is shown in figure 2.5.

The robustness of the AC method is of major importance, since an error in the attenuation map could lead to a wrong diagnosis of the patient. This can be enabled by multiple techniques that depend on the attenuation correction method. In general, in a simultaneous PET/MR system, the MR hardware and the patient bed contribute to the attenuation of the 511 keV photons and should therefore be taken into account. Additionally, the total acquisition time and radiation dose should only be minimally increased by the attenuation correction [6].

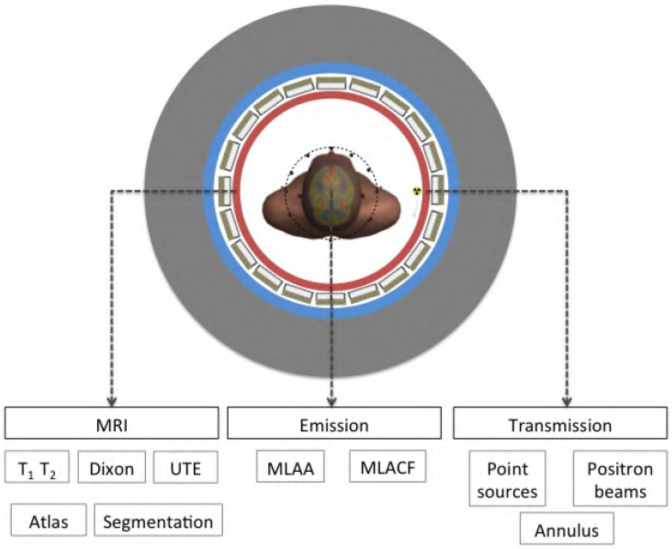

Figure 2.5: An overview of the different attenuation correction methods in PET/MR imaging. [6]

2.3.2.1 PET based methods

The first option is to derive the attenuation map from the PET measurements. Since the PET acquisition needs to happen anyway, this will not increase the total acquisition time. Several methods have been developed, based on transmission data as well as emission data.

Transmission based methods

A positron emitter, called the transmission source, is placed inside the FOV of the PET scanner. Two scans are acquired subsequently: a reference scan, where no patient or patient table is present inside the FOV, and a transmission scan, where the patient is placed on the table and positioned in the FOV. By comparing both scans and using an iterative algorithm, the attenuation map can be derived [1]. Some challenges occur by using this method. First of all, the extra dose administered to the patient is kept as low as possible, which results in a noisy transmission image with limited spatial resolution. Additionally, the limited space inside the scanner makes it difficult to introduce the transmission source. By acquiring the extra scans, time is added to the total acquisition time. This effect can be limited by acquiring the transmission data and emission data simultaneously, which is only possible when TOF information is available and complex reconstruction methods are used to account for crosstalk, count rate effects and scattering. [6]

Emission based methods

It has been shown that by using TOF emission data, the attenuation map can be derived up to a constant factor [7]. Algorithms like Maximum Likelihood reconstruction of Attenuation and Activity (MLAA) are incorporated in these methods. They can only be used with certain tracers, since activity is required in all regions of which one needs to know the attenuation. Their applicability is thus limited because of the fact that no emission is coming from the attenuating objects outside the patient. Finally, scatter correction becomes very complex when only emission data is used.

2.3.2.2 MRI based methods

When obtaining an MR image, the signal intensity depends on the proton density and relaxation properties. Therefore, there is no direct way to obtain the attenuation map from the MR signals, since attenuation coefficients depend on electron density. Additionally, tissue types with ultrashort T2 relaxation times (shorter than 1 ms) can not be visualized using conventional MRI sequences. This is caused by a limitation on the minimally achievable echo time. Using conventional MRI sequences, the signals from these tissues are decayed before they can be acquired by the scanner. The tissue types with ultrashort T2 relaxation times that are relevant for attenuation correction are lung tissue ($T_2^* \approx$ 0.5 - 3 ms) and cortical bone ($T_2^* \approx$0.4 ms). Due to their short T2 relaxation time, it is impossible to differentiate between bone, lung and air on a standard MR image, although their attenuation coefficients are very different.

Template and atlas based

In template and atlas based techniques, a large number of registered MR/CT datasets, called the atlas, are used to create a pseudo-CT template. This template can be formed by taking a weighted average of the images in the atlas, or by applying more complex techniques. Afterwards, transformations are applied to fit the template to an anatomical MRI of the patient. Besides the shorter acquisition time as a benefit of these techniques, more structural details can be taken into account and a continuous range of attenuation coefficients can be assigned to a region. A major drawback of these methods is the fact that anatomical abnormalities cannot be taken into account.

Segmentation based

Attenuation maps can be derived by labeling different regions in the image based on MR intensity and assigning a predefined attenuation value to the different tissue types. This can be done without making assumptions on the anatomy of the patient, which is a big advantage since anatomical abnormalities can be taken into account. A major drawback of the segmentation methods is the inability to account for inter-patient variability and variations of the attenuation coefficients within one tissue type in the body. Efforts have been made to directly link the intensity of the MR signal to the attenuation coefficient, but so far no consistent relationship has been found.

Chapter 3

Segmentation-based attenuation correction in PET/MR

3.1 Introduction

In this chapter, segmentation-based attenuation correction is discussed. Specialized MR sequences have been developed in order to discriminate different tissue types based on their MR intensities. First of all, the requirements for these methods are discussed. Secondly, the different challenges that occur during segmentation are presented. Additionally, three different MR sequences that are used for segmentation are discussed. The Dixon sequence is used to obtain a water-only and fat-only image, which enable discrimination of background, lung tissue, soft tissue and fat. An important limitation of this method is the fact that bone is not taken into account, which leads to underestimation of the PET activity, especially in osseous lesions. ZTE (Zero-Echo Time) and UTE (Ultrashort Echo Time) are two sequences that are designed to start acquiring data as fast as possible after RF excitation and therefore enable visualization of bone tissue.

3.2 Requirements

When segmentation techniques are applied, one of the questions that arises is the number of tissue types that should be distinguished. This was studied in detail using simulations in [3]. Since attenuation effects depend on the size of the imaging volume, a distinction was made between rat imaging, human brain imaging and whole-body imaging. The results indicated that when imaging a rat, discriminating air, lung and soft tissue leads to accurate quantitative results. During human brain imaging, air, soft tissue and bone tissue should be discriminated. The skull causes the proportion of bone to be quite large compared to other body parts. Accurate segmentation of bone, air and soft tissue is needed to detect very small legions in the brain. This is reported in multiple studies, like [3] and [8].

In whole body imaging, 5 tissue types should be discriminated according to [3]: air, lung tissue, soft tissue, spongious bone and cortical bone. When imaging the whole body, discriminating lung tissue is the most important, since lungs cover a large volume in the thorax. When lung tissue is misclassified, this has a large impact on attenuation correction. When misclassification occurs, it is preferable that the lung tissue is segmented as air, since the attenuation coefficient of air and lung are relatively close (difference of $0.027cm^{-1}$). Different studies publish contrary results on the influence of bone tissue on the whole body attenuation map. In [9] and [10], bone tissue was segmented as soft tissue and underestimations smaller than 8% for lesions were reported compared to CT attenuation correction, which is not clinically relevant. In [11], underestimations of 11% of PET activity were reported, which can lead to misdiagnoses. In [3], it was concluded as well that bone tissue should be discriminated in whole body PET/MR. Additionally, research was done on the impact of misclassification errors. Details on this can be found in [3].

3.3 Challenges

3.3.1 MR truncation correction

In a hybrid PET/MR system, the transaxial FOV is different for the PET imaging system and the MR imaging system. While the FOV of the PET system is slightly smaller than its ring diameter, the FOV of the MR system is limited by the homogeneity of the external magnetic field B_0. In PET/MR scanners, this is usually around 50 cm. This limitation can cause an artifact in the MR imaging: truncation of the arms in large patients. Using MR data with truncated body parts for attenuation correction leads to incomplete attenuation maps and underestimation of the PET activity [12]. The effect of this artifact has been investigated by different researchers and a number of solutions have been proposed. In [13], errors between 20 and 30% have been reported in heart and spine regions. The error can rise to 50% in the ribs. They propose a solution where the attenuation map is supplemented with a rough estimation of arm position. In [14], an algorithm is presented where PET emission data are used to estimate the missing parts in the attenuation map. Errors up to 25% are expected when truncated arms are not compensated.

3.3.2 Interpatient variability of attenuation coefficients

Segmentation based attenuation correction methods typically assign a predefined attenuation value to a certain tissue type, thereby not accounting for interpatient variability in tissue density and therefore attenuation coefficient. This can cause a potential PET bias. Interpatient variability of soft tissue is not significant, but the standard deviation of lung density is 20 times higher and not taking this into account can lead to errors up to 30% in PET quantification. A possible solution is proposed in [15], where the MR sequence establishes a relationship between MR intensity and lung density. For whole body imaging, [3] reported that interpatient variability of cortical bone density does not significantly effect PET quantification, while [16] reported that the HU of cortical bone variates up to 10% and different cortical bone tissue classes should be considered.

3.3.3 Ancillary objects in the PET FOV

Several objects like the patient bed, MR coils, positioning aids and medical probes can lead to underestimation of the PET activity when not taken into account in the attenuation map. These objects can be added to the attenuation map, but precise position information is needed since small errors can lead to a significant PET bias. Objects like small positioning probes, cardiac or respiratory probes,... do not need to be added to the attenuation map. [12]

3.3.4 Susceptibility artifacts

Metal objects present in the PET/MR scanner result in severe artifacts due to distortion of the local magnetic field. Since they cause a dropout of the signal, the tissues in the surrounding of the metal object can be misclassified as air during segmentation, which can generate significant errors in the attenuation map. Atlas-based attenuation correction methods are more robust to susceptibility artifacts, since prior knowledge on attenuation values in different regions can be used. [12]

3.4 Dixon sequence

The first method that was used to apply segmentation was based on chemical shift imaging, using the in-phase/out-of-phase cycling of fat and water. Two images were acquired, one in-phase image and one out-of-phase image. By combining these images, a water-only and fat-only image could be created. This can be explained as follows:

$$IP = W + F$$

$$OP = W - F$$

Where IP and OP represent the intensities in the in-phase and out-of-phase images. When the following combinations are made:

$$W = \frac{IP + OP}{2},$$

$$F = \frac{IP - OP}{2},$$

the image W is water-only and the image F is fat-only. Dixon sequences are much more complicated than presented here and a number of correction techniques need to be applied. Details on that can be found in [17]. In [18], a method was presented that uses a Dixon sequence for segmentation-based attenuation correction in whole-body PET/MR. Four tissue classes were discriminated: background, fat, soft tissue and lungs. The water and fat images were used to discriminate fat from soft tissue by determining thresholds. The lungs were segmented by using a connected-component analysis. By applying a morphologic closing filter to the binary tissue-air image, it was prevented that cortical bone was classified as air. Nevertheless, not discriminating cortical bone from other tissue types resulted in an underestimation of PET tracer uptake, especially in osseous lesions. In [18], 35 patients were imaged with PET/CT and PET/MR. The average reduction in SUV (Specific Uptake Value) for osseous lesions was 8%. It was shown that this reduction was mainly caused by not taking cortical bone into account in the attenuation map. Since small errors in SUV's can lead to wrong conclusions in patient follow-up, this method needs to be used with caution.

3.5 ZTE and UTE sequences

Dedicated MRI sequences have been developed to make visualization of bone and lung tissue possible. Ultrashort Echo Time (UTE) and Zero Echo Time (ZTE) are both designed in order to start acquisition of the signal as fast as possible after the excitation RF pulse. In UTE, the readout gradients are turned on once the acquisition starts. In ZTE, the readout gradients are turned on before the excitation RF pulse in a way that the center of k-space is crossed at the time of the excitation pulse. The transmit/receiver coils cannot switch from transmit to receive mode immediately and therefore, no data acquisition is happening for the center of k-space. This gap in k-space is filled afterwards using analytical reconstruction or other techniques. When the transmit/receiver switching time is $\delta T_{Tx/Tr}$ and the sampling time is Δt, the number of data points that are missing in radial direction is $\frac{\delta T_{Tx/Tr}}{\Delta t}$. Since the readout gradients are not ramped down in between acquisitions, the nominal echo time TE = 0s, hence the name Zero Echo Time. The nominal echo time is defined as the center k-space TE.[19] The ZTE and UTE sequences are shown in figure 3.1.

Typically, a 3D radial path is followed through k-space. In conventional MRI, where the k-space is sampled on a cartesian grid, a gradient is needed to get to the beginning of a line in k-space. Since this requires time, radial paths are used in ZTE and UTE. The sampling starts at the center and moves out radially. One radial line in k-space is called a spoke.

In conventional MRI, spin echo or gradient echo is used to refocus the spins. This is not possible when trying to measure signals coming from tissues with very short T2 relaxation time, since these signals would have decayed before the echo is formed. Therefore, the Free Induction Decay (FID) is sampled instead of an echo in ZTE and UTE.

In ZTE and UTE, special truncated RF pulses are used. Conventional 90 degree RF pulses can take up to 40 ms. In tissues with very short T2, relaxation happens so fast that it cannot be ignored during the application of the RF pulse. To obtain shorter RF pulses, high power is applied. However, due to hardware limitations and safety regulations, the output power of the RF coils is limited. Secondly, the short RF pulse results in a broader bandwidth which can lead to poor slice selection in 2D imaging. Therefore, mostly 3D imaging is used. Typically, a low flip angle (often smaller than 10°) is used. The minimal gradient ramping and short RF excitation pulses result in submillisecond repetition times and a relatively high SNR.[19]

After the RF excitation pulse, the energy in the transmit/receiver coils needs to ring down, which normally takes a few μs. This results in an extra delay on the start of acquisition. Another problem that arises when trying to image short T2 tissue types is their broad resonance peak compared to tissue types with longer T2. This causes them to respond to excitation pulses not only at the Larmor frequency, but also to excitation pulses with a slightly different frequency. This can lead to reduction in the signal when fat saturation pulses are applied

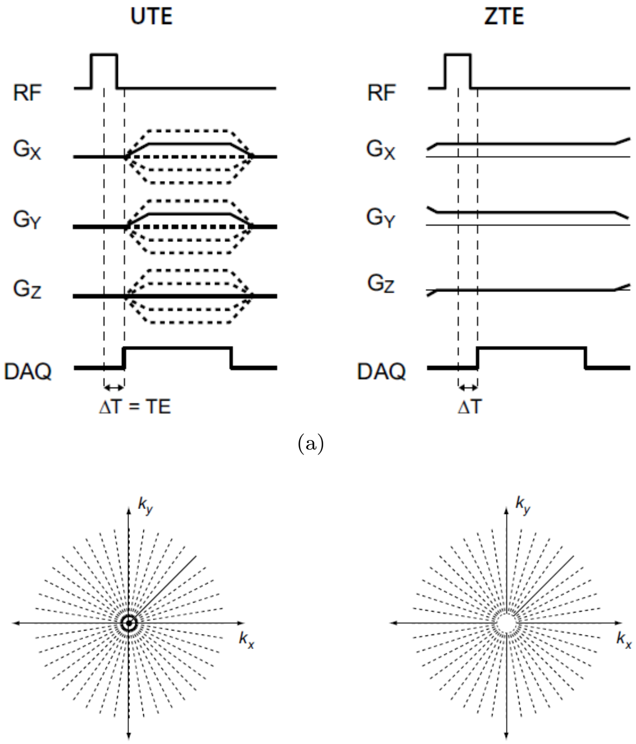

(a)

(b)

Figure 3.1: (a) A single TR of the UTE and ZTE sequences, (b) the corresponding k-space coverage. [20]

3.5.1 UTE-based segmentation

In [3], a method is described to do segmentation of air, bone and soft tissue based on an FID and gradient echo image obtained with the UTE sequence. Air will have low intensity on the FID as well as the gradient echo. Cortical bone will have high intensity on the FID but low intensity on the gradient echo, since the short T2 causes decay of the signal. Soft tissue will have high intensity on both images. Since the image intensity in MRI is strongly dependent on receiver gain settings, it is not possible to directly apply segmentation based on the image intensities. Therefore, the quantitative parameter $R_2 = \frac{1}{T_2}$, called the transverse relaxation rate, is calculated by comparing two measurements. R_2 can be calculated by assuming that the intensity of the signal only depends on transverse relaxation. This assumption is correct for short echo times. The following equations explain how the R_2-map can be calculated voxel by voxel. [3]

$$\vec{M}_{tr}(T_{E1}) = I_1 = \vec{M}_{tr} e^{\frac{-T_{E1}}{T_2}}$$

$$\vec{M}_{tr}(T_{E2}) = I_2 = \vec{M}_{tr} e^{\frac{-T_{E2}}{T_2}}$$

$$R_2 = \frac{1}{T_2} = \frac{ln(I_1) - ln(I_2)}{T_{E2} - T_{E1}} \tag{3.1}$$

Since the FID and gradient echo image are both obtained within the same sequence and with the same receiver gain settings, these two images can be used to calculate the R_2-map. An example of such an R_2-map and its corresponding histogram is shown in figure 3.2. On the joint histogram of the uncorrected R_2-map and the CT, it is clear that soft tissue and cortical bone can clearly be discriminated based on their R_2-value, but this is not the case for air. This is caused by the low quality of the FID image, which results in noise adding up to the intensities. Since air has low signal in the gradient echo image, noise in the FID image can cause a high R_2-value, based on equation 3.1. This can be resolved by applying an air mask outside of the body. Nevertheless, in the pelvic region, air is also present inside the body. Since discrimination between air and bone is crucial to obtain an accurate attenuation map, this method can only be used with caution.

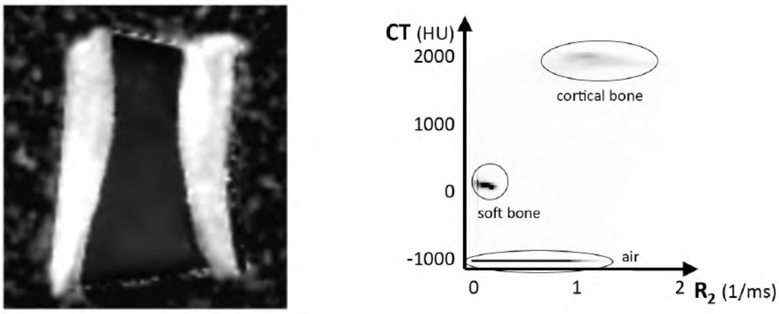

(a)

(b)

Figure 3.2: (a) Example of an R_2-map of the bovine femur bone, (b) the corresponding joint histogram of the uncorrected R_2-map and the CT [3]

3.5.2 WASPI

WASPI is a 3D radial ZTE sequence with fat and water suppression. In theory, the WASPI sequence provides better visualization of bone than the simple ZTE sequence, since the fluid and fat signals are suppressed, and can be used to obtain a patient-specific pseudo-CT in bone tissue in a similar way as the simple ZTE sequence [22]. In practice, a large part of the dense bone signal is attenuated as well, so ZTE should yield the strongest dense bone signal [23]. The sequence is shown in figure 3.3.

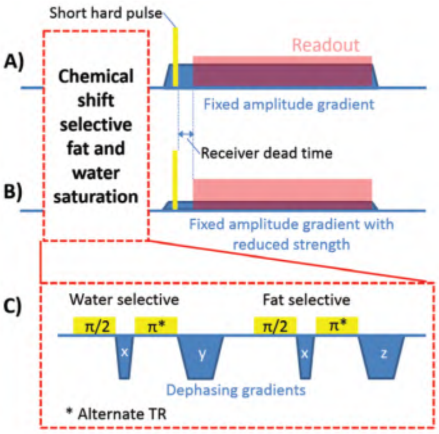

Figure 3.3: The WASPI pulse sequence. (A) main data set and (B) data set for a finer sampled k-space centre. (C) water and fat suppression (based on chemical shift). [22]

3.5.3 Benefits of ZTE over UTE

ZTE and UTE are similar techniques both used to visualize tissues with very short T2 relaxation times, but there are some clear indications why ZTE is more interesting for clinical use than UTE. First of all, the gradients are kept active during the RF pulsing and only small directional changes are made in between repetition times. This fastens up the scanning, reduces the acoustic noise and minimizes eddy currents, which results in a robust sequence. Measurements of the signal can be started faster after excitation, which increases the signal-to-noise ratio (SNR) compared to UTE. The zero echo time, short repetition time (TR) and small flip angle result in a proton density-weighted (PD-weighted) image, while UTE images are T2-weighted. The benefit of this is that no long T2 suppression techniques are needed, again increasing the speed and robustness of the sequence (inversely related to the sensitivity on gradient fidelity)[19]. UTE on the other hand offers more image contrast options and can function in 2D mode [20]. Recent research has shown that the signal intensity of bone in brain ZTE images is inversely proportional to the bone density and can therefore directly be linked to the corresponding Hounsfield unit [21]. Therefore, ZTE images can be used to obtain a continuous patient-specific pseudo-CT in bone tissue. In [23], a similar relationship is obtained for pelvic ZTE images.

3.6 Discussion

Different methods have been developed to provide attenuation correction in PET/MR imaging. The segmentation methods are relatively simple to implement in the imaging workflow and are robust to anatomical differences, since only the MR data of the patient are used to calculate the attenuation map. Nevertheless, significant errors can be made when not enough tissue classes are discriminated or voxels are misclassified. In brain imaging, bone discrimination is very important, since the skull attenuates a large part of the photons. In whole body imaging, lung tissue and trabecular bone need to be discriminated as well. Attenuation coefficient variability is not taken into account in most segmentation algorithms and can lead to significant errors. Atlas-based methods show promising results, especially in brain imaging, since small anatomical structures can be taken into account. Nevertheless, a database of CT/MR images is needed, the computational demands are high and anatomical abnormalities like tumors can cause problems. Attenuation correction using emission data only show promising results for TOF PET. All different methods have benefits and drawbacks, and further research is needed to overcome certain challenges [12]. This thesis is situated within the MR-based attenuation correction methods, more specific the use of the ZTE sequence to segment different tissue classes. ZTE has been clinically evaluated in [24] and [21]. In [24], it is concluded that PD-weighted ZTE is an efficient and robust method to obtain an accurate depiction of bone structures in the head and it provides good contrast between air, soft tissue and bone. In [21], it is shown that ZTE is more accurate than atlas-based attenuation correction for the head, but misclassification of small bone structures in the nasal region is a problem that needs to be tackled.

Chapter 4

Focus on the pelvis

4.1 Introduction

PET/MR imaging has been used mostly in brain imaging, where attenuation correction techniques are well developed and applied. Therefore, in this thesis, the focus is on another body part: the pelvis. This is a region with a high portion of bones and therefore accurate attenuation correction is crucial. Among others, PET/MR imaging in the pelvic region has been applied for patients with prostate cancer, gynecologic cancer, and rectal cancer. In 2017, a study on prostate cancer at the KULeuven is planned using PET/MR imaging. Another clinical study will use PET/MR for imaging of the cervix. In this chapter, some general information is given on the different applications of PET/MR of the pelvic region, recent research on pelvic PET/MR imaging and a paper published in January 2017 that proposes a technique to use a ZTE image for attenuation correction in the pelvis. Nowadays, CT, PET and MR imaging often are used as complementary imaging modalities. As further explained, the question rises whether PET/MR can be used for the diagnosis of these cancer without applying CT.

4.2 Prostate cancer

Prostate cancer is the development of cancer in the prostate gland, where seminal fluid is produced and stored. Normal semen-secreting prostate gland cells mutate into cancer cells. Over time, the cancer cells begin to multiply and spread to the stroma, the surrounding prostate tissue, and potentially to other organs. In most cases, prostate cancers grow quite slow and do not cause any symptoms in an early phase. Therefore, a lot of men have prostate cancer without knowing it, and without the cancer causing a direct risk to the health. But the prostate cancer can spread out to other parts of the body, mostly the bones and lymph nodes. When the cancer in the prostate gland has grown, it can press the uretha, the tube that carries urine during urination and semen during ejaculation, thereby causing urinary disfunction and problems with ejaculation. Prostate cancer can be treated with surgery, radiotherapy, brachytherapy, chemotherapy and hormone therapy. During surgery, the entire prostate gland plus some of the tissue around it is removed. This is called radical prostatectomy. Active surveillance can be chosen instead of more agressive local therapy. This way, the risks and side effects of these therapies can be avoided. The tumor is monitored for signs of growth by PSA measurements (prostate-specific antigen), Digital Rectal Examination (DRE) and/or biopsies. Prostate cancer is the cancer with the highest prevalence in men and the third most common cause of cancer death in men in Europe [25]. 20 to 30 percent of patients who have undergone prostatectomy relapse within 10 years and 53 percent of patients who have undergone external beam radiotherapy relapse within 5 years [26] [27]. Over the years, an increase in incidence is reported, but this is mostly due to the availability of PSA screening. A decreasing mortality trend has been observed in multiple European countries after 1996. However, the relative impact of curative treatment versus early detection by PSA measurements is still under debate. The distribution of the expected cases and deaths (per 100 000 inhabitants) for the 5 most common cancers in Europe 2012 in males is shown in figure 4.1. The age-standardised incidence and mortality rates by area and country in Europe anno 2012 are shown in figure 4.2. The difference between countries in incidence is mostly linked to the availability of PSA screening.

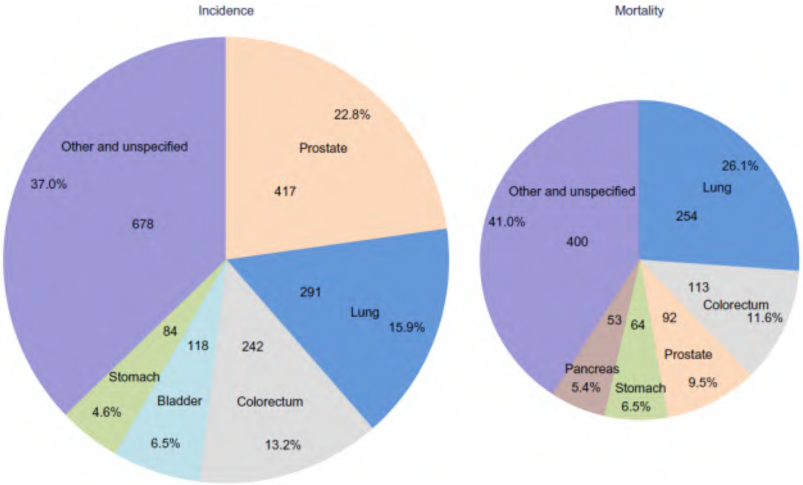

Figure 4.1: The distribution of the expected cases and deaths (per 100 000 inhabitants) for the 5 most common cancers in Europe 2012 in males.[25]

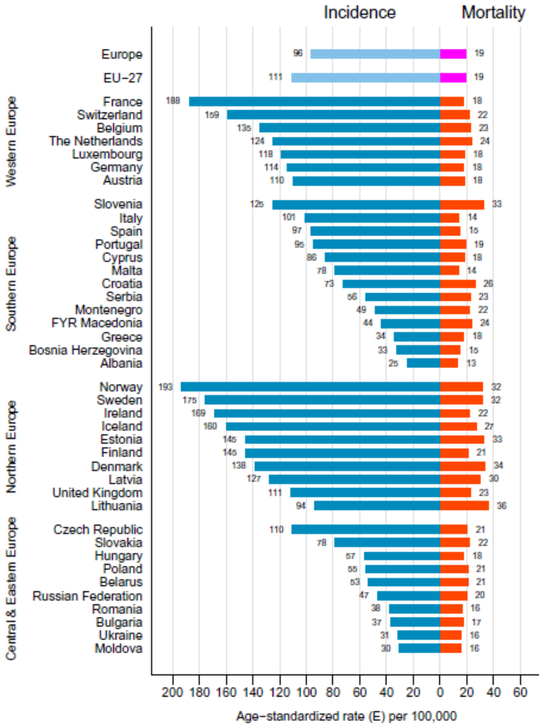

Figure 4.2: The age-standardised incidence and mortality rates for prostate cancer by area and country in Europe in 2012. [25]

4.2.1 Screening

Two common tests are used to screen patients for prostate cancer: a DRE and a PSA-test.

DRE

During a Digital Rectal Examination (DRE), a doctor enters the rectum of the patient with a finger, determines the size of the prostate and feels if there are any irregularities.

PSA test

Prostate cancer cells produce less PSA than healthy prostate cells, due to the disruption of their normal functioning. But, since prostate cancer causes an increased number of cells, there is an increased level of PSA in the prostate of these patients. This causes more PSA to diffuse into the blood and the level of PSA in the serum increases. Therefore, PSA can be used as a serum marker for prostate cancer.

A blood sample is taken from the patient and the total level of PSA is measured. A value over 4 ng/ml is considered to be 'abnormal'. But a high PSA level does not necessarily mean that the patient has prostate cancer, this can also be due to a benign enlargement of the prostate (Benign Prostatic Hyperplasia, BPH), a urinary tract infection or a prostate infection, and a normal PSA level can occur even when the patient has prostate cancer.

The most important limitation of PSA testing is its relative lack of specificity. Within the 4 to 10 ng/ml range, prostate cancer is only present in 25% of the patients. Most patients with PSA level less than 10 ng/ml with prostate cancer, are in the early phase of the disease and don't have any symptoms. More than half of the patients with PSA levels above 10 ng/ml are already in an advanced stage of the disease. Therefore, detecting prostate cancer in an early phase requires low cut-off values and this causes unnecessary worrying and further research for a lot of man where the elevated PSA level is caused by something else.

Using the PSA level in the serum as screening method is somehow controversial, since it causes the risk of over-diagnosis and over-treatment. Localized prostate cancer is mostly asymptomatic and does not form a direct threat to the overall health of the patient. The question rises whether having the diagnosis benefits the patient.

4.2.2 Diagnosis

When the PSA blood test and DRE indicate that the patient might have prostate cancer, a transrectal ultrasound (TRUS) guided biopsy is done and the tissue samples are checked for the presence of cancer cells. Dependent on the PSA levels, the DRE and the results of the biopsy, additional medical images can be made to see whether the cancer has spread to other body parts (mostly lymph nodes and bones), since PSA levels don't allow differentiation between local (cancer hasn't spread out to other body parts), regional (cancer has spread out to nearby regions) and distant disease (cancer has spread to distant lymph nodes, bones, or other organs). This differentiation is a requirement for effective disease management. Dependent on the stage of the disease, active surveillance can be chosen over radical (and possible morbid) treatment. Medical images can allow precise knowledge on the location and size of lesions. 11C-choline PET/CT is an often used imaging tool to detect metastatic sites in case of an increased PSA level in the serum after primary treatment. The detection rate of Choline PET/CT for the recurrence of prostate cancer shows a linear correlation with the PSA value. In patients with a PSA value above 3 ng/ml, the recurrence can be diagnosed in about 75% of the patients [28]. However, there are still patients with biochemical recurrence in whom no correlation for the increased PSA level can be found. For primary prostate cancer, using PET/CT has limited use since the uptake in BPH and prostatitis prevents discrimination from cancerous tissue. Furthermore, PET/CT images show low resolution of the prostate anatomy. Using PET/MR instead of PET/CT can improve the detection of metastasis and prostate cancers, since MR has a higher soft tissue contrast, can distinguish changes in the prostatic parenchyma from normal prostate tissue and can assess small structures in the inner pelvis. 35% of primary prostate cancers is missed on biopsies, so the need to improve the detection is high.

PET tracers used for prostate cancer

Since 18F-FDG has shown only limited sensitivity for the imaging of prostate cancer, other specific tracers have been developed, such as 18-fluorodihydrotestosterone (18FFDHT), 11C-actetate, 11C-methionine, and 11C-labelled or 19F-labelled choline derivatives. 11C-choline and 19F-choline are mostly used, especially for the diagnosis of recurrent prostate cancer. Its use is based on the increased uptake and turnover of choline in prostate cancer cells. New radiotracers such as 68Ga-labelled PSMA (prostate specific membrane antigen) show promising results.

4.2.3 PET/MR imaging for prostate cancer

In [29], two PET/MR acquisition protocols are described (one for primary prostate cancer and one for recurrent prostate cancer). The attenuation correction is done by acquiring a two-point Dixon VIBE sequence (Volumetric Interpolated Breath-hold Examination) in one breath hold during expiration. In MR imaging, a large range of different sequences are available and the protocol needs to be adapted to the clinical question asked. Next to evaluation of the prostate and prostate bed in the pelvis, the focus has to be on the search for bone and lymph node metastases in the region from the head until the pelvis (whole-body). The acquisition protocols are shown in figure 4.3. The acquisition protocol for the pelvis focusing on the prostate for patients with possible primary prostate cancer differs from the acquisition protocol for patient with recurrent prostate cancer. In case of primary cancer, an axial T1-weighted TSE (Turbo Spin Echo) and an isotropic T2-weighted sequence are applied. These allow more detailed imaging of the infiltration of the neurovascular bundle of the prostate and seminal vessels. In the case of recurrent cancer, a T2-weighted TSE sequence is applied. In both cases, an axial DWI (diffusion-weighted image) is acquired in combination with an axial T1 dynamic contrast enhanced sequence (for example TWIST). The total acquisition time for the pelvis region is between 15 and 20 minutes. During this time, the PET image can be acquired.

The T2-weighted images have a high spatial resolution and provide anatomical information. The prostate cancer usally appears dark compared to the bright peripheral zone of the prostate. A limitation is that benign abnormalities such as chronic prostatitis, scars, effects from radiotherapy or hormonal treatment, atrophy, hyperplasia and post-biopsy hemorrhage can resemble tumor tissue. The DCE (dynamic contrast enhanced) images help in detecting sites of prostate cancer, since angiogenesis results in changes in vascular characteristics. The sites of prostate cancer typically show an earlier and more intense enhancement of the signal and earlier, more rapid washout compared to normal prostate tissue. A limitation of DCE is the discrimination of cancer from prostatitis and BPH nodes. When DWI (Diffusion Weighted Imaging) is applied, the movement of the water molecules within the prostate gland are examined. Within tumors, the movement of water molecules is restricted. Research has shown that the intensity of cancerous tissue on DW images correlates with the cellular density of the cancer. Therefore, DWI can be used to characterize tumor aggressiveness. In the case of primary prostate cancer detection and staging, a

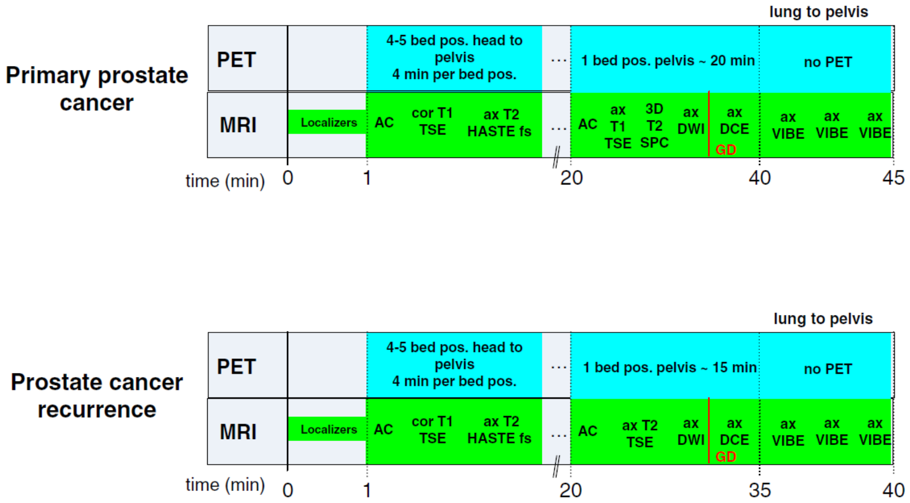

Figure 4.3: 2 PET/MR acquisition protocols (one for primary prostate cancer and one for prostate cancer recurrence).

T1-weighted anatomical sequence is acquired to recognize hemorrhagic regions in the prostate. The multiparametric approach where a combination of T2-weighted, DCE and DWI is made, has shown to have a sensitivity of 80% and a specificity of 97% for the detection of prostate cancer in the peripheral zone. In the transition zone, a sensitivity of 53% and a specificity of 83% has been reported [30]. MRS (Magnetic Resonance Spectroscopy) is another functional imaging technique that can be used to differentiate cancerous tissue from normal prostate tissue. In [31], it was observed that MRS has a sensitivity of 77%.

In [32], a sufficiently high correlation in SUVs between PET/MR and PET/CT has been reported so that PET/MR can be quantitatively used. [29] reports a better anatomical allocation of lesions of 11C-PET/MR compared to PET/CT, especially in the prostate and bone. An example is shown in figure 4.4. In [33], it was shown that the combined information of PET and MR data was better than the data from PET/CT or the data from PET or MR alone. In [34] and [35], the use of 11C-Acetate PET/MR showed an improved specificity compared to PET and MR alone. New radiotracers such as 68Ga-labelled PSMA (prostate specific membrane antigen) are more selectively accumulated in prostate cancer cells, which enables better discrimination from other pathologies [36]. In [32], 25 patients with rising PSA levels after definitive treatment of prostate cancer are imaged with 11C-choline PET/MR (T2, DWI and DCE) and 11C-choline PET/CT. It was observed that PET/MR detected more regions suspicious of local recurrence than PET/CT (10 versus 6 patients).

In [37], 20 patients underwent a PET/CT 1 hour after injection of the 68Ga-PSMA ligand followed by PET/MRI 3 hours after injection. The quantification accuracy of the PET/MR system was evaluated by comparing the differences in SUV between the PET/CT 1 hour after injection and the PET/MR 3 hours

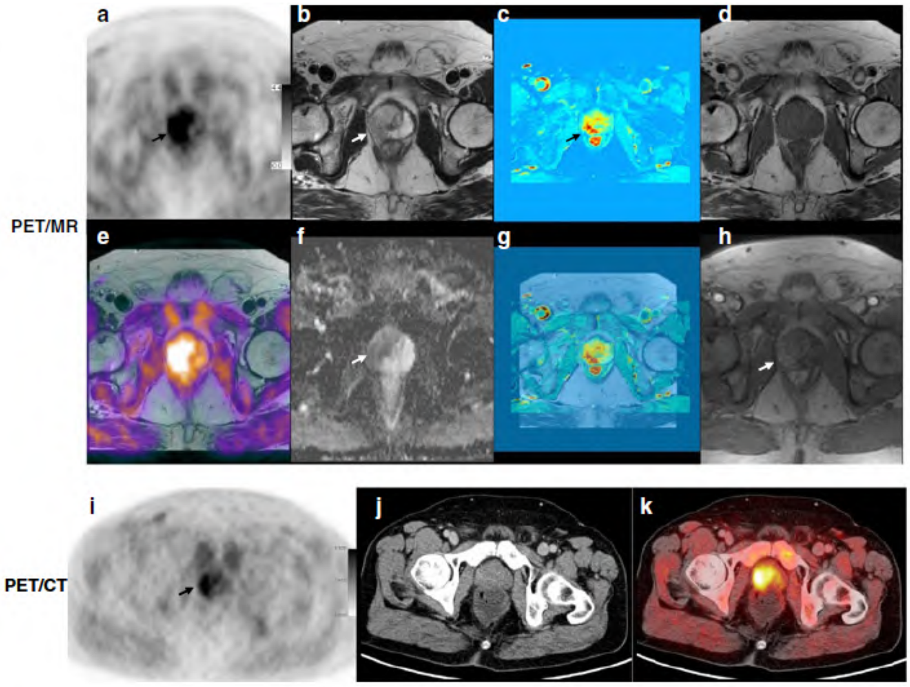

Figure 4.4: 11C-Choline PET/CT and PET/MR images of a 66-year-old patient with prostate cancer proven by biopsy. The images were performed consecutively using one injection. The black arrows in (a) and (i) show an increased focal 11C-choline uptake in the right side of the prostate, which suggests prostate cancer. On the different MR images, a lesion is seen in the right peripheral zone: a hypointense signal on the T2-weighted sequence (b), high ADC values (and therefore low signal) on the diffusion weighted image (f) and hypervascularity in the DCE image (h). The T1-weighted image in (d) did not show any evidence of haemorrhage. (e) shows the fused image of the PET and MR modalities. In (k) the fused image of PET and CT is shown while in (j) the CT image is shown. Note that the tumor cannot be differentiated from the CT image alone. [29]

after injection with the differences in SUV between a PET/CT 1 hour after injection and a PET/CT 3 hours after injection in another patient cohort. It was concluded that evaluation of tumors was subjectively easier in PET/MR due to higher contrast and resolution. In 4 patients, unclear findings on the PET/CT image could be clarified thanks to the PET/MR image. On the other hand, a reduced signal was observed at the level of the kidneys (15 patients) and urinary bladder (11 patients) in the PET image of the PET/MR scanner, which led to reduced SUV in 6 lesions.

In [38], 15 patients were examined with a PET/MR scanner. 18F-Choline was used as radiotracer and the MR protocol consisted of a T2-weighted and diffusion weighted sequence. 8 of the patients were diagnosed with prostate cancer after biopsy, 2 patients had negative results in repeated biopsies and 5 patients had increased PSA levels after being treated for prostate cancer but did not have a biopsy. 2 radiologists evaluated the image quality, while the PET images were also evaluated quantitatively. It was concluded that PET imaging adds diagnostic confidence to the MR images in identifying and localizing tumors in the prostate region. It was concluded that all three of the acquired images (T2-weighted MR, DWI and PET image) added up to the diagnostic power. In 3 patients with proven prostate cancer, the DWI did not show a lesion, while the PET image showed higher SUV. In 1 patient, the PET image did not show a higher uptake of choline, while the DWI did point in the right direction.

4.3 Gynecologic cancer

Gynecologic cancers include cancers of the ovaries and fallopian tubes, uterine corpus, uterine cervix and vagina, and vulva. Cervical cancer is the leading cause of cancer-related death in women worldwide. Most cervical cancers are caused by the HPV virus, which is transmitted through sexual contact. PET/CT and MR imaging play a complementary role in the diagnosis of cervical cancer. The most used treatments are surgery and concurrent chemotherapy, and radiotherapy. The tumor size and parametrial extension (best seen on MR images) combined with lymphadenopathy (best seen on CT images) are used to determine which therapy is most fitted. DCE MR imaging and DWI are included in the MR protocol and, similar to there use in prostate imaging, help to discriminate benign from malignant tissue and provide quantitative tissue characterization (SUV's, apparent diffusion coefficients and tumor volume).

Early experiences with the use of PET/MR for gynecologic cancers are encouraging. The resolution of MR is lower than CT, but it nevertheless can detect tumors below the resolution of PET. [39]

4.4 Rectal cancer

Colorectal cancer is the development of cancer from the colon or rectum. PET/CT imaging is the conventional imaging modality used in the diagnosis phase. Nevertheless, in [40], it was shown that PET/MR has a higher sensitivity to detect lesions (98.3% versus 84.2%).

4.5 Hybrid ZTE/Dixon MR-based attenuation correction for quantitative uptake estimation of pelvic lesions in PET/MR

A very recent paper ([23], accepted date: 18/01/2017) proposes an MR-based method for attenuation correction in pelvic PET/MR. The MR sequence consisted of two-point Dixon sequence and a ZTE sequence. The two-point Dixon images were used to provide a continuous-value fat and water pseudoCT. The ZTE image was used to segment the bone and convert the ZTE intensity of bone pixels to Hounsfield units (HU) using a continuous two-segment piecewise linear model. This way, a bone density estimation is made, which improves PET quantification. The method is shown in figure 4.5. Datasets from 6 patients with pelvic lesions were used to compare the attenuation map from the hybrid ZTE/Dixon MRAC to the CT attenuation map, which was taken as ground truth, by calculating the root-mean-squared error (RMSE). The methodology presented in this paper provides good results (RMSE of the standardized uptake values reduced from 11.02% to 3.28% for bone lesions), but includes some manual corrections in the segmentation step. In this section, the methodology of bone segmentation in [23] is explained.

Bone segmentation

The ZTE image displays cortical bone with moderate and air with low signal intensity. Different imaging techniques are applied to enhance bone:

- High-pass filtering: enhance the edges and therefore bone.
- Logarithmic intensity rescaling
- Top-Hat Morphological filtering: used to extract small elements from an image. This is done by computing the morphological opening of the image and subtract this from the original image. It is used to enhance the bone, which has sharp edges.
- Global thresholding: produce initial bone mask.
- Morphological area opening: Area opening is obtained by an erosion followed by a dilation. It is used to reduce noise in the image.
- Manual correction: eliminate non-bone structures. How the manual correction step is done in [23] is not explained.
- Filling operation: fill up mask. This operation is used to fill up holes (dark pixels surrounded by lighter pixels).

The result is shown in figure 4.6.

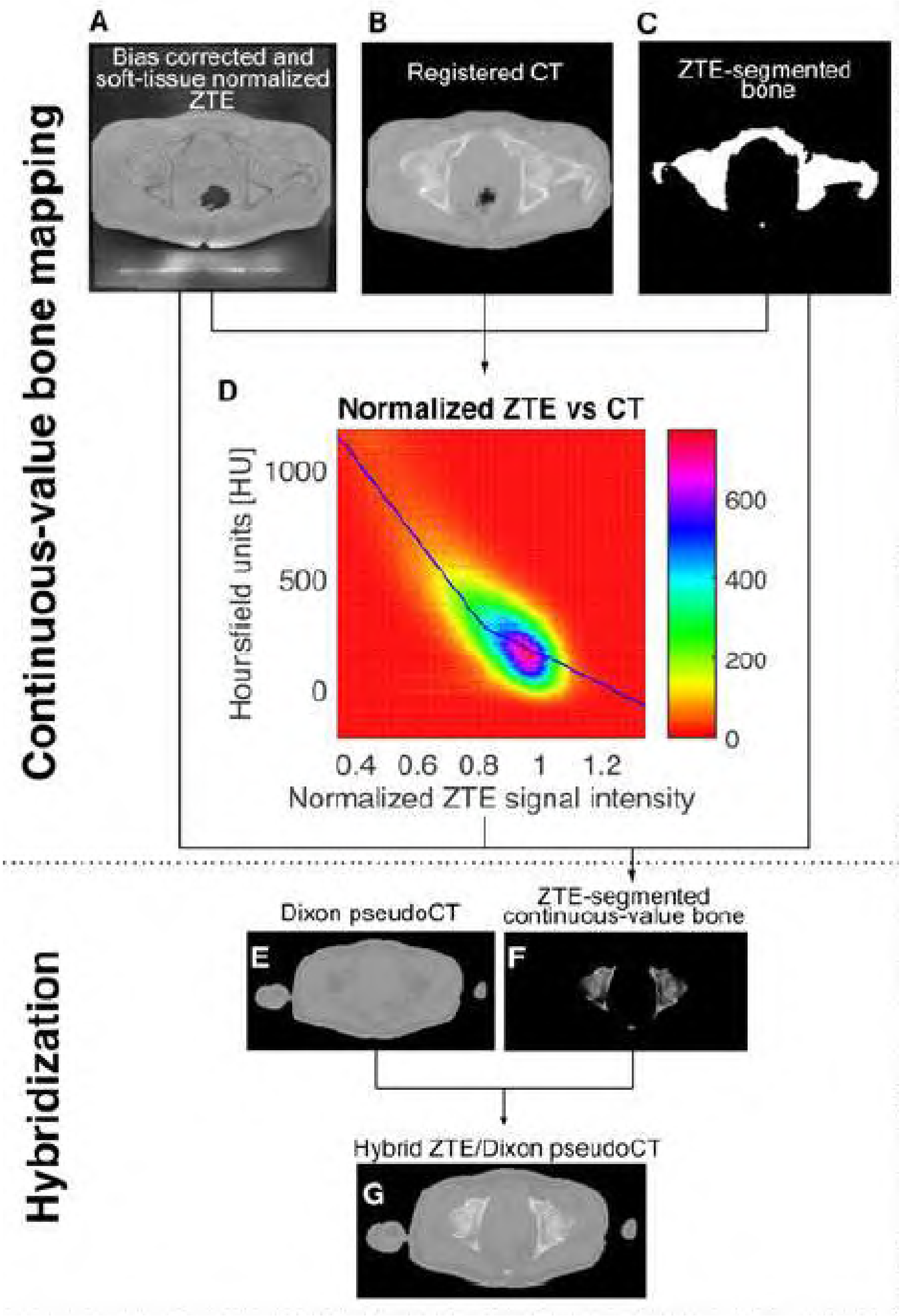

Figure 4.5: ZTE and CT images are coregistered to produce a linear model where normalized ZTE signal intensity is converted to Hounsfield units. Least squares fitting was used to obtain a two-segment piecewise linear model. In the hybridization step, the Dixon pseudo-CT and continuous-valued bone are combined. [23]

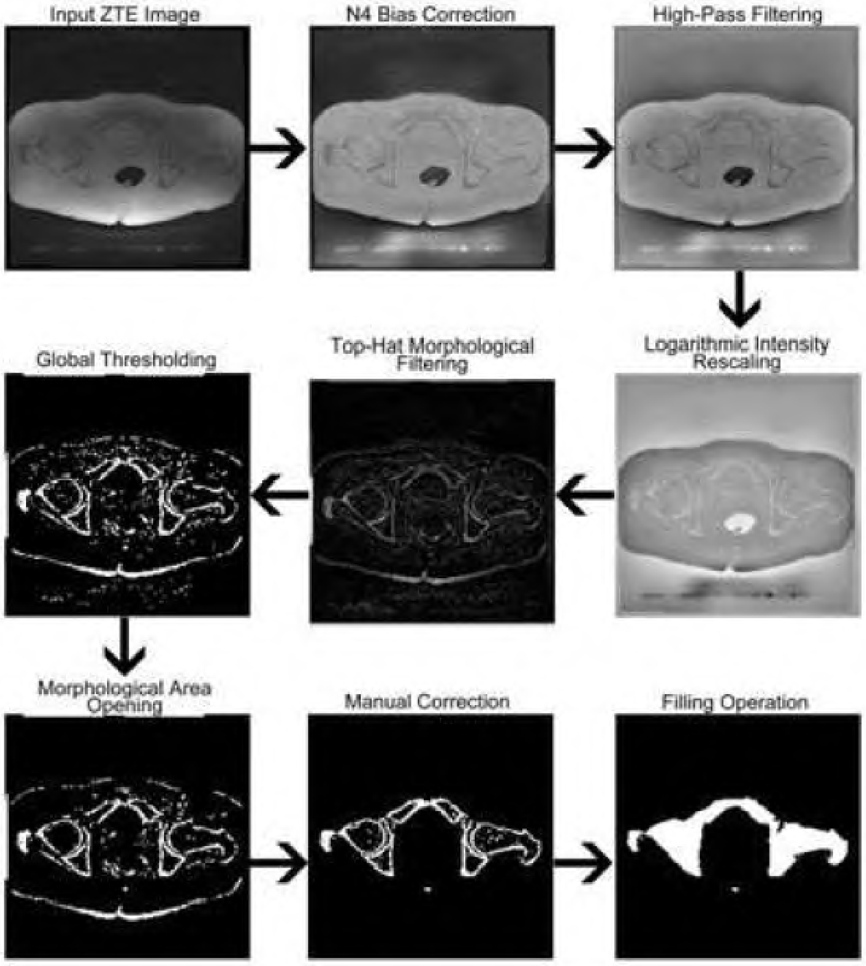

Figure 4.6: The bone segmentation process applied on one image. [23]

Chapter 5

Data acquisition and parameter optimization

5.1 Introduction

Multiple MR and CT datasets were obtained over the span of a few months. The MR datasets were acquired by the integrated 3 tesla TOF PET/MRI system (SIGNA PET/MR, GE Healthcare, Waukesha, WI, USA) in the university hospital of Leuven, using a body coil. By altering the parameters of the ZTE sequence while a volunteer was in the scanner, the image quality was optimized. Important to note is that we had very limited access to the core of this sequence and only a few parameters could be altered. Secondly, GE Healthcare clearly stated that the ZTE sequence available at the university hospital of Leuven is optimized for head imaging only, and that there is no guarantee that its use for other body parts would result in acceptable image quality. The CT images are acquired using the Siemens Biograph 40 PET/CT in the university hospital of Leuven, at 120 kVp.

5.2 Animal study 3/01

On the 3th of January, ZTE and CT images were obtained from the hip region of a dead sheep. The sheep was kept in a plastic bag, which might have decreased the image quality. Due to the size of the sheep, incomplete ZTE data were obtained. This can be seen in figure 5.1. Because of the poor quality of these images, they were not further used.

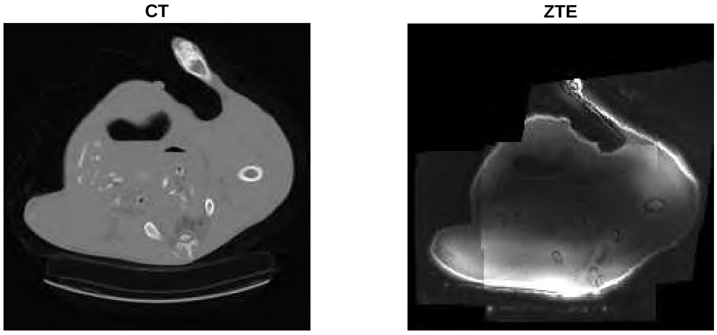

Figure 5.1: CT and ZTE image of the hip region of a sheep.

5.3 Volunteer study 4/04

On April the 4th, a healthy volunteer (female, 23 years old, 65 kg) was scanned. Different ZTE images were acquired, as well as two-point Dixon images. The original ZTE image has the original protocol parameters. In the second image, the parameters used in [23] are applied. The resolution is higher but the signal-to-noise ratio (SNR) is lower (74% of original ZTE image). The image parameters are described below. Two axial images are shown in figure 5.2. In this figure it is clear that the second image is of better quality.

- ZTE original: FOV = 320x320x360 mm, resolution = 2.9 mm, slice thickness = 3.1 mm, bandwidth =±62.5 kHz, flip angle = 1°.
- ZTE article ([23]): FOV = 340x340x220 mm, isotropic resolution = 2 mm, bandwidth =±62.5 kHz, flip angle = 1°.

In order to obtain hybrid ZTE/Dixon attenuation map, two-point Dixon images were acquired. Again, the original Dixon parameters as well as the parameters used in [23] were applied. The images are shown in 5.3.

- Dixon original: FOV = 380x380x447 mm, resolution = 1.17 mm, slice thickness = 2.6 mm, bandwidth = ±142.86 kHz, flip angle = 10°.
- Dixon article: FOV = 500x500x458 mm, resolution = 1.54 mm, slice thickness = 5.2 mm, bandwidth = ±166.67 kHz, flip angle = 10°.

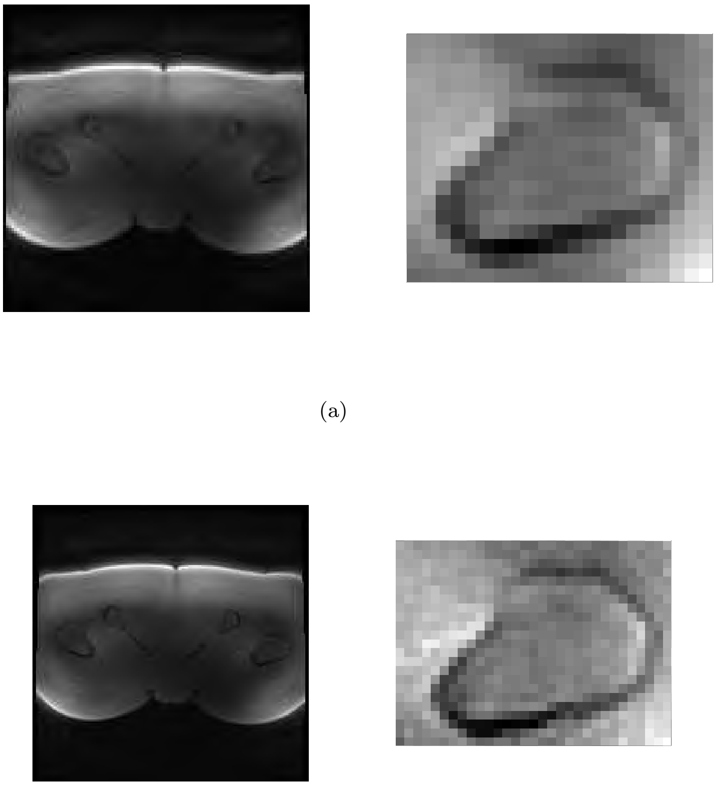

(a)

(b)

Figure 5.2: (a) Original ZTE parameters, (b) ZTE parameters used in [23].

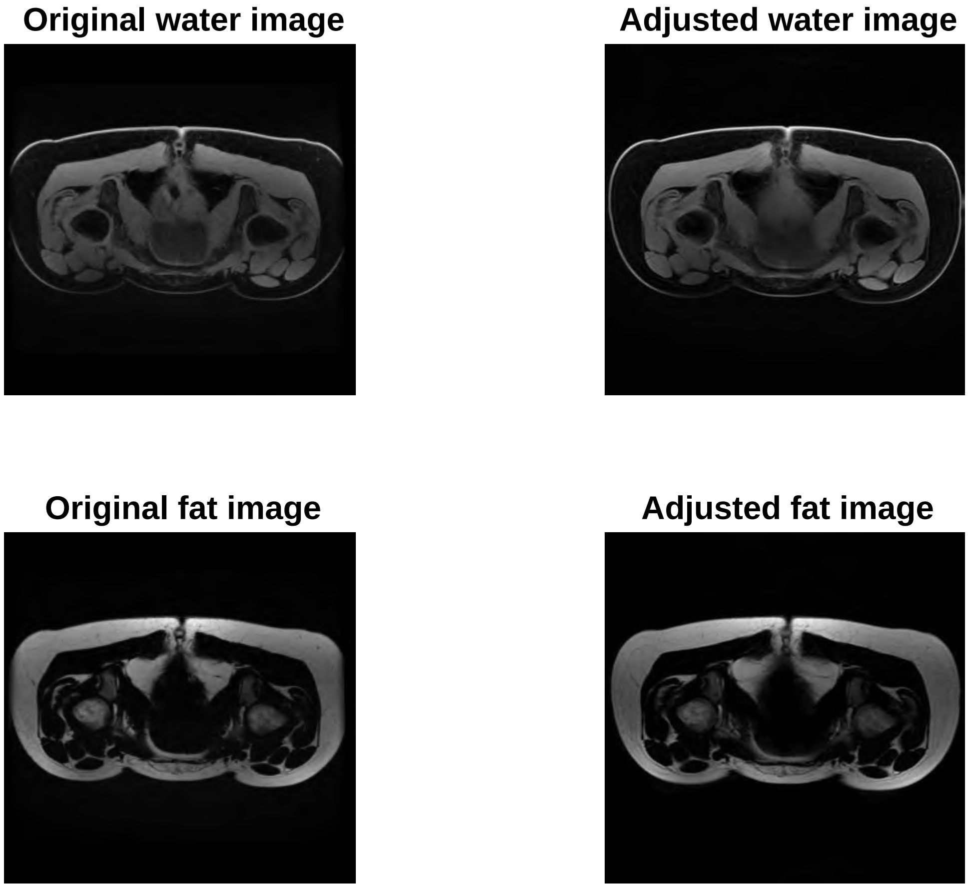

Original water image

Adjusted water image

Original fat image

Adjusted fat image

Figure 5.3: Two-point Dixon images, with the original parameters as well as the adjusted parameters used in [23].

5.4 Patient study 25/04

On april the 25th, the cervix of a patient was scanned in the PET/CT and afterwards PET/MR scanner. Both the CT and ZTE data are available. The scan parameters of the ZTE sequence are: FOV = 400x400x275 mm, resolution = 2.35 mm, slice thickness = 2.5 mm, bandwidth =±62.5 kHz, flip angle = 1°.

5.5 Volunteer study 5/05

On may the 5th, a volunteer (male, 70 kg) was scanned in order to further optimize the ZTE parameters. The following parameters were adjusted: resolution, number of averages, flip angle and the enabling of fat/water saturation (WASPI). Their impact on the quality of the ZTE images is described below.

5.5.1 Resolution

In addition to the previous patient study, a ZTE image with a 3D uniform resolution of 1.6 mm, 2 mm and 3 mm was obtained. The results are shown in figure 5.4 and 5.5. In figure 5.4, a slice is shown where the contrast between the cortical bones and their surroundings is sufficient to visually differentiate the bone for a resolution of 1.6 and 2 mm. In figure 5.5, a slice is shown where the bone structures cannot be differentiated from their surroundings for any of the resolutions. The sequence parameters for the different ZTE images are described below.

- 1.6 mm: FOV = 300x300x96 mm, isotropic resolution = 1.6 mm, bandwidth =±62.5 kHz, flip angle = 1°.
- 2 mm: FOV = 340x340x220 mm, isotropic resolution = 2 mm, bandwidth =±62.5 kHz, flip angle = 1°.
- 3 mm: FOV = 300x300x180 mm, isotropic resolution = 3 mm, bandwidth =±62.5 kHz, flip angle = 1°.

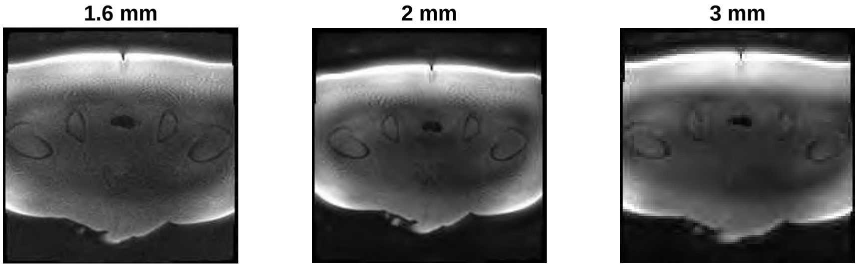

Figure 5.4: ZTE images of a hip slice with three different resolutions. The bone structures can be differentiated from soft tissue for a resolution of 1.6 and 2 mm.

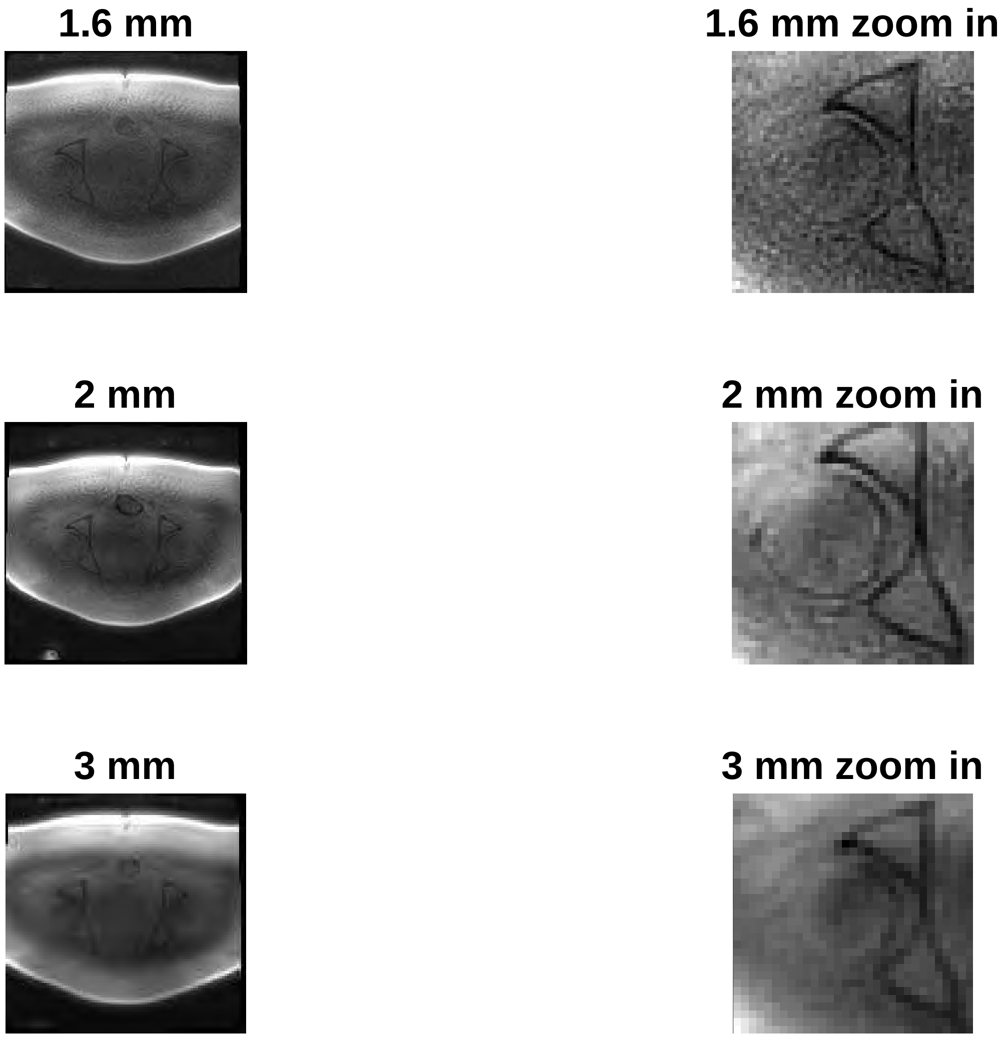

1.6 mm

1.6 mm zoom in

2 mm

2 mm zoom in

3 mm

3 mm zoom in

Figure 5.5: ZTE images of a hip slice with low contrast for three different resolutions. It can be seen that some of the bone structures cannot be differentiated from the soft tissue, independent on the resolution.

5.5.2 Filter

GE provides built-in filters to enhance the contrast in the acquired MR images. The options are: 'some sharpening, some smoothing', 'some sharpening, strong smoothing', 'strong sharpening, some smoothing' and 'strong sharpening, strong smoothing'. All these filters were applied on ZTE images, but neither of them made a significant difference. This can be seen in figure 5.6, where the third filter is applied on a ZTE slice with the following parameters: FOV = 340x340x136 mm, resolution = 2 mm, slice thickness = 3.4 mm, bandwidth =±62.5 kHz, flip angle = 1°.

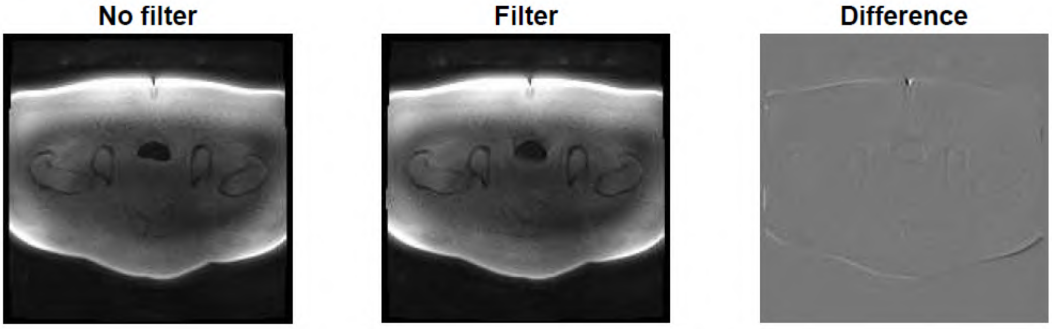

Figure 5.6: ZTE images of a hip slice with filtering applied (strong sharpening, some smoothing). The difference between the ZTE image without filter and the ZTE image with filter is not significant.

5.5.3 Number of signal averages

To suppress the effect of random variations, a larger number of repeated ZTE images can be acquired. By taking the average image, image noise should be reduced. In figure 5.7, it can be seen that increasing the number of signal averages (NSA) does not improve the image quality. The default value of NSA for the ZTE sequence is 4. The other sequence parameters are: FOV = 340x340x136 mm, resolution = 2 mm, slice thickness = 3.4 mm, bandwidth =±62.5 kHz, flip angle = 1°.

5.5.4 Flip angle

For completeness, the flip angle was adjusted to see the effect on the image quality. The result can be seen in figure 5.8. The parameters of the ZTE sequence were: FOV = 340x340x120 mm, isotropic resolution = 2 mm, bandwidth =±37.5 kHz, flip angle = 4°.

5.5.5 Fat and water suppression

As described in chapter 3, fat and water suppression can be added to the ZTE sequence for better visualisation of the bone. This is called the WASPI sequence, as described in [22]. In [23], it was already mentioned that adding fat and/or

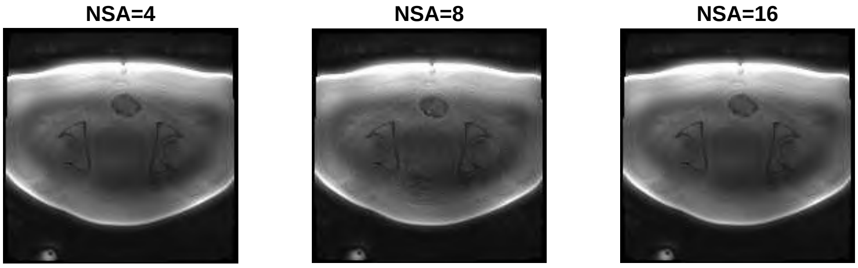

Figure 5.7: Increasing the number of signal averages (NSA) has little impact on the image quality.

water suppression severely attenuates the signal coming from bone, which makes the images useless. We verified this and the result can be seen in figure 5.9.

Figure 5.8: ZTE image of the hip with a flip angle of 4°.

Figure 5.9: ZTE image of the hip with fat suppression.

5.6 Animal study 10/05

On the 10th of May, the leg of a dead pig was scanned using a head coil. The motive of this study was twofold. First of all, the bone parts in the leg of the pig have a simple geometry, which allows better registration. Second of all, scanning smaller regions made it possible to test how small the resolution can be chosen without memory issues to pop up. The minimal resolution that was reached is 1 mm. When trying to scan with a resolution of 0.8 mm, the error 'Memory size too large' was given, independent on the FOV that was chosen. In figure 5.10, a slice of the ZTE image is shown for resolutions of 1.6 mm and 1 mm. It is clear that a resolution of 1 mm provides better results. The sequence parameters for the different ZTE images are described below.

- 1.6 mm: FOV = 140x140x192 mm, isotropic resolution = 1.6 mm, bandwidth =±62.5 kHz, flip angle = 1°.
- 1 mm: FOV = 140x140x180 mm, isotropic resolution = 1 mm, bandwidth =±62.5 kHz, flip angle = 1°.

In the patient study, it was concluded that increasing the number of signal averages did not significantly improve the quality of the image. This was repeated for the pig leg for a resolution of 1 mm. Here, increasing the NSA did improve the quality of the image. This is shown in figure 5.11. The exact reason that these images are of much higher quality than the ZTE images of the human pelvis, is not known. One possible explanation is the fact that the bone is much smaller and therefore the head coil was used instead of the body coil. Since the ZTE sequence is optimized for brain imaging using a head coil, this could lead to better images.

Figure 5.10: ZTE image of the leg of a pig with two different resolutions.

Figure 5.11: Increasing the number of signal averages (NSA) has a clear impact on the image quality.

5.7 Cortical bone properties in the pelvis

In figure 5.5, it can be seen that at some parts, the cortical bone in the proximal femur cannot be distinguished from it surroundings at any resolution. The explanation for this was found in literature, where studies have shown that the thickness of the cortical bone in the proximal femur can vary between 0.3 and 4 mm [41] [42]. Even with a resolution of 1 mm, partial volume effects will make thin cortical bones indistinguishable. When the ZTE sequence is used for brain imaging, this poses no problem since the resolution can be chosen smaller than 1 mm and the sequence is optimized for brain imaging. [19]

Chapter 6

Image registration

6.1 Multimodal field-of-view correction

An essential step before registration can be applied on two images of different imaging modalities, is to match the FOV's of the two images, since the two scanners work on imaging volumes with (slightly) different coverages. This is called FOV correction or coverage estimation. In most cases, this is applied when one image is full body and the other is of a specific anatomical region. In FOV correction, the best portion of a full body scan that is compatible with an anatomical specific second image is identified. In [43], this is done in three steps. First of all, symmetry based translation/rotation correction is applied. Secondly, a multi-modal feature descriptor is calculated. The final step consists of matching schemes using dynamic programming. An attempt to implement translation/rotation correction is described below.

6.1.1 Symmetry based translation correction

The symmetry of the human body in the left-right direction is used to correct for translation. This method is not modality specific and can therefore be applied to MR and CT images. Translation changes are calculated in one image and are corrected for along both axes separately. Consider a translation error along the left-right axis, which is denoted here as x-axis. This is a horizontal line in the center of the image when sliced axially. If there is no translational error along the x-axis, the image is symmetric about y, the anterior-posterior axis. Consider a translational error Δx. The image (IM1) is now symmetric about an axis $y*$ which lies at a distance Δx of y. We now exploit the symmetry of the image and flip the image about the central y-axis. The obtained image (IM2) is symmetric about an axis $y*_F$ that lies at distance $2\Delta x$ of $y*$. $y*$ and $y*_F$ are equidistant from y. When IM2 is translated over IM1, the left region of IM2 (which equals the right region of IM1) will align with the left region of IM1 at distance $2\Delta x$. Since we assume symmetry, this alignment will result in maximum correlation between IM1 and IM2. The flipping step and correlation step can be combined by convolving IM1 with itself. This can be done computationally efficient by using the Fast Fourier Transform (fft) in Matlab. The results of this algorithm are shown in figure 6.1.

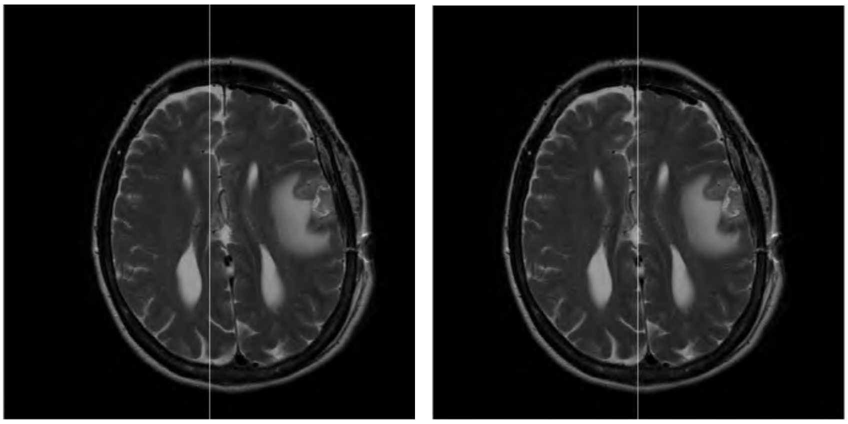
(a) (b)

Figure 6.1: (a) Translated image, (b) Image after translation correction.

Unfortunately, this algorithm did not provide good results in case of ZTE hip images used in this thesis. This is shown by using one slice of a ZTE hip image with a translation of 10 pixels, shown in figure 6.2. In figure 6.3, the calculated shift based on convolution for every line of the slice is plotted. It is clear that this method will not result in a translation correction of 10 pixels.

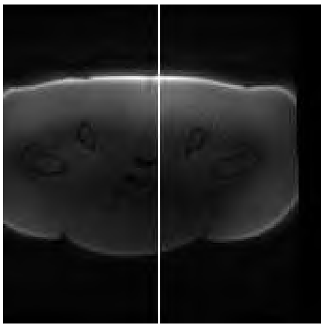

Figure 6.2: ZTE hip image with a translation of 10 pixels.

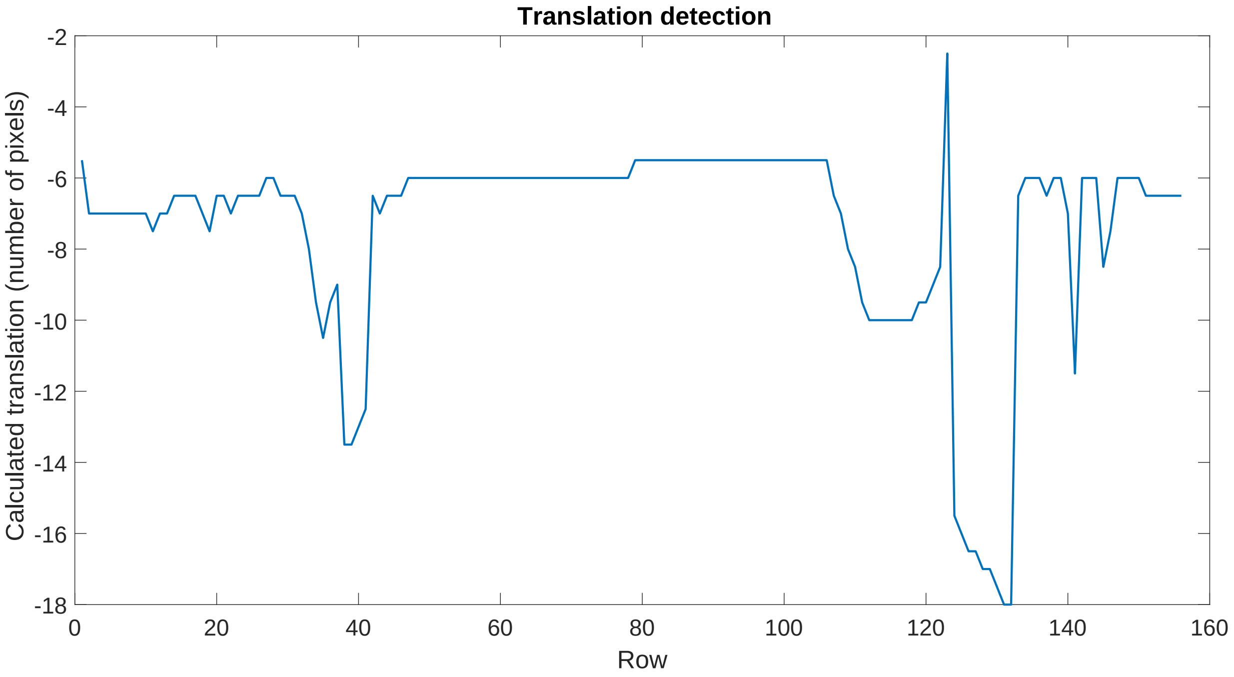

Figure 6.3: In the translation correction algorithm, the shift is calculated based on convolution in every line in every slice of the image. In this plot, it can be seen that for the ZTE hip slice with a translation of 10 pixels, the calculated shift based on convolution is not 10 pixels for most of the lines in one slice. Therefore, this algorithm will not result in a shift of 10 pixels.

6.1.2 Symmetry based rotation correction

Rotations can be corrected for in a similar way as translation, but in the polar co-ordinate system. This is explained in [44]. Consider an image IM2 that is rotated and translated compared to IM1. The first step is to take the absolute value of the Fourier transform of this image. Since translation in image space results in an imaginary exponent, taking the absolute value results in nullification of the translation. The absolute value of the Fourier transform of IM2 is now a rotated version of the absolute value of the Fourier transform of IM1. Therefore, when we change to polar co-ordinates, this translates into a translation shift: $IM1(\rho, \theta) = IM2(\rho, \theta - \theta_0)$. The rotation θ_0 can then be obtained by applying translation correction. Unfortunately, this is easier said than done. When applying this algorithm to the image used in the previous section (see figure 6.1), the results are not good. In figure 6.4, it is clear that the fft of the rotated image is the rotated version of the fft of the original image, but a lot of noise is present. When this image is then transformed to polar coordinates (see figure 6.5), it becomes impossible to calculate a translation.

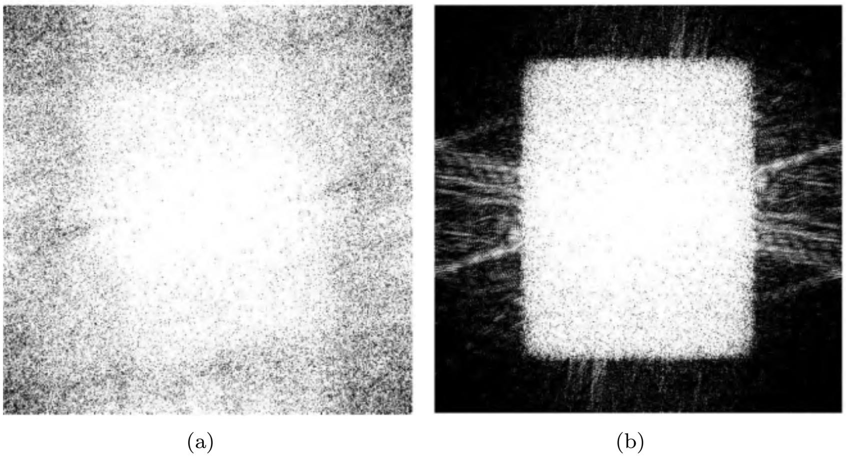

(a) (b)

Figure 6.4: Absolute value of the Fast Fourier Transform (fft) of a) the rotated image and b) the original image. The images are shown in logscale.

Calculating the angle between 2 images

In order to get more insight in rotation detection, an algorithm was implemented to calculate the angle between 2 images. The algorithm works as follows:

1. compute the absolute value of the FFT of both images
2. change to polar coordinates
3. apply filter (Blackman filter)
4. take the Fourier transform
5. calculate the phase correlation between both
6. take the inverse fourier transform
7. the location of the maximum is the angle of rotation

In figure 6.6, the results are shown for angles from 0 to 20 degrees. It is clear that the results are not accurate.

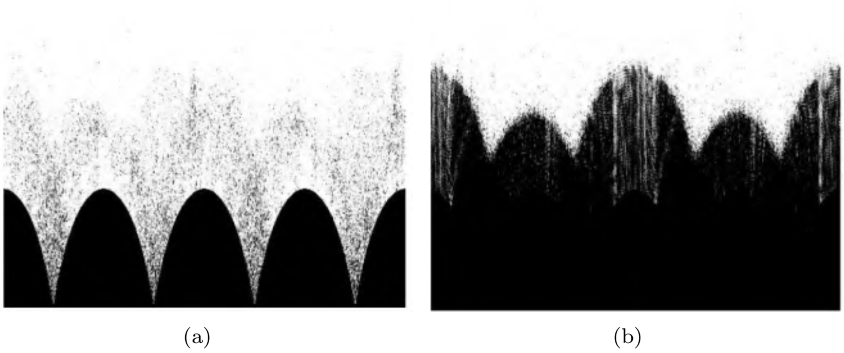

(a) (b)

Figure 6.5: Absolute value of the Fast Fourier Transform (fft) in polar coordinates of a) the rotated image and b) the original image. The images are shown in logscale.

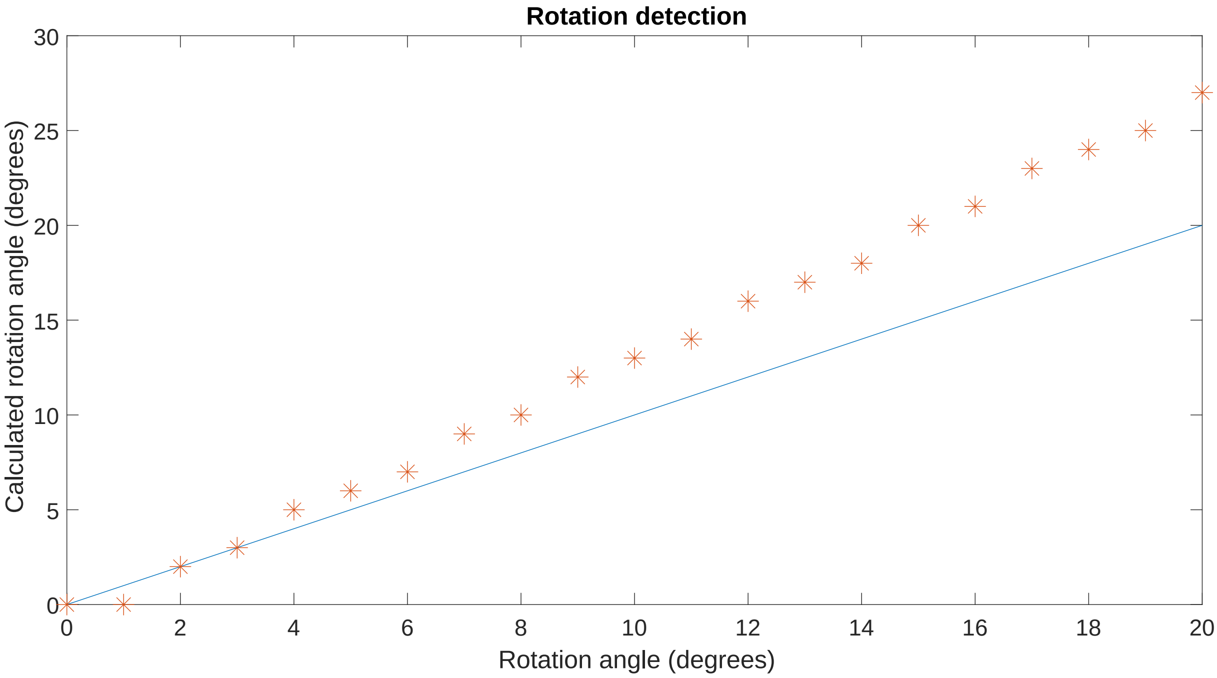

Figure 6.6: The detected angle of rotation.

6.1.3 Conclusion

Algorithms were programmed in Matlab for rotation and translation correction, but did not provide useful results in case of the ZTE hip images used in this thesis. Therefore, it was decided that these simple methods were insufficient for pre-registration purposes, and more advanced techniques should be programmed. Since image (pre-)registration is not the main topic of this thesis, translation and rotation correction as well as FOV correction were done manually, and pre-programmed toolboxes and freely available software were used to further register images.

6.2 Multimodal image registration

Aligning the ZTE and CT images is an essential step before obtaining an attenuation map. A wide range of image registration techniques exist and multiple software packages and toolboxes provide this option. In this thesis, the built-in Matlab registration functions, the MIRT package and the ITK toolbox were applied. Since we are dealing with multimodal imaging, multimodal image registration needs to be applied. As similarity metric, mutual information is used. Mutual information measures how much can be known from one image if only the other image is known. It can be calculated by using the joint entropy and the conditional entropy of the two images. It is based on the following formula:

$$I(R, T \circ \varphi) \equiv H(R) + H(T \circ \varphi) - H(R, T \circ \varphi),$$

where I is the mutual information and H is the complexity. In this formula, there are three components: the complexity of the reference image R; the complexity of the transformed image $T \circ \varphi$ and the complexity of the joint histogram. The registration process is than based on the maximization of the complexity of both image datasets while assuring that the complexity of one image dataset approaches the complexity of the other as much as possible. Intuitively, the clustering of the joint histogram is maximized and it will show certain clusters for gray tones of matching structures.

6.2.1 MIRT package

The MIRT package (2007-2010 Andriy Myronenko) is a Matlab software package for 2D and 3D non-rigid image registration which supports mutual information as similarity measure and uses cubic B-spline based transformation parametrization. In figure 6.8, the result of the 3D image registration is shown for 3 slices. It is clear that the registration is not sufficient. In figure 6.7, the result of 2D image registration is shown (applied on one slice). For clear visualisation, the CT bone mask is laid over the ZTE image. It is clear that the bone parts in both images do not overlap. Therefore, this registration result cannot be further used.

6.2.2 built-in Matlab functions

Using the functions $imregconfig$ with modality set to 'multimodal', mutual information based image registration is applied as well. This provides similar,

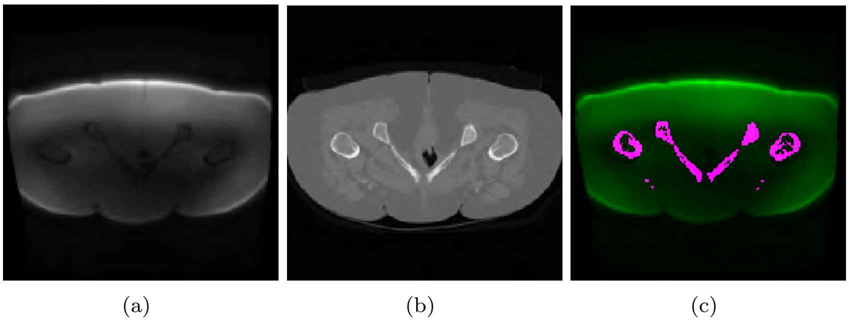

(a) (b) (c)

Figure 6.7: 2D registration of ZTE and CT image of the hip based on mutual information. (a) ZTE image, (b) CT image, (c) registration result.

insufficient results as the MIRT package. Affine (translation, rotation, scale, and shear) as well as similarity (translation, rotation, and scale) transformations are applied .

6.2.3 ITK

Insight Segmentation and Registration Toolkit (ITK) is an open-source system that provides an extensive suite of software tools for image analysis. Since ITK cannot be used in Matlab, Python was used instead. No sufficiently good registration results were obtained by using ITK.

6.2.4 Conclusion

The fact that the patient walked from the PET/CT scanner to the PET/MR scanner, resulted in two 3D images that are very difficult to register. Even the beds from the two scanners where the patient lay on, had a different shape. On top of that, it is crucial that the bone parts overlap, since this is necessary for investigation of the relationship between CT and ZTE intensity in bone voxels. It is concluded that none of the used methods resulted in sufficiently good registration. Therefore, another method is applied. First of all, bone segmentation is done for the ZTE and CT images individually. Afterwards, monomodal registration is done. Since both images are now binary, mean squares can be used as similarity metric. The result for one slice is shown in figure 6.9.

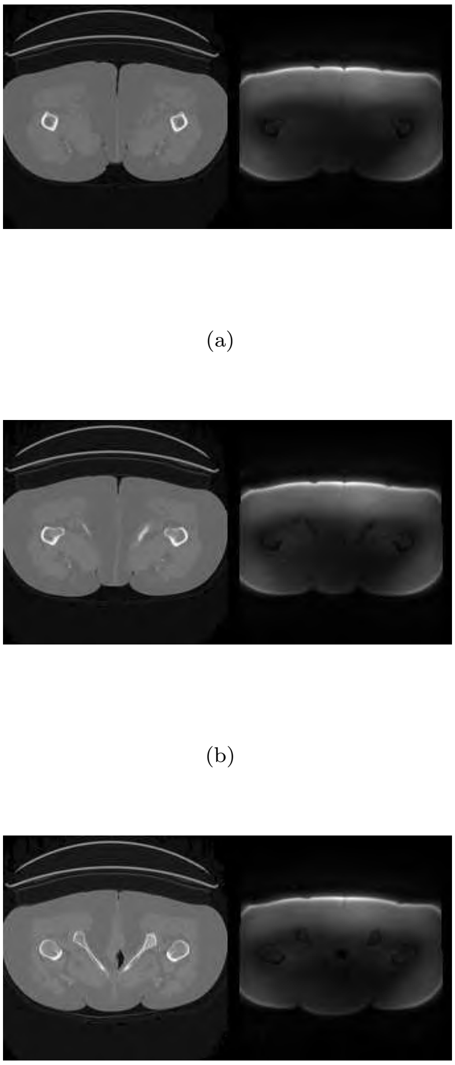

(a)

(b)

(c)

Figure 6.8: 3D registration of ZTE and CT image of the hip based on mutual information.

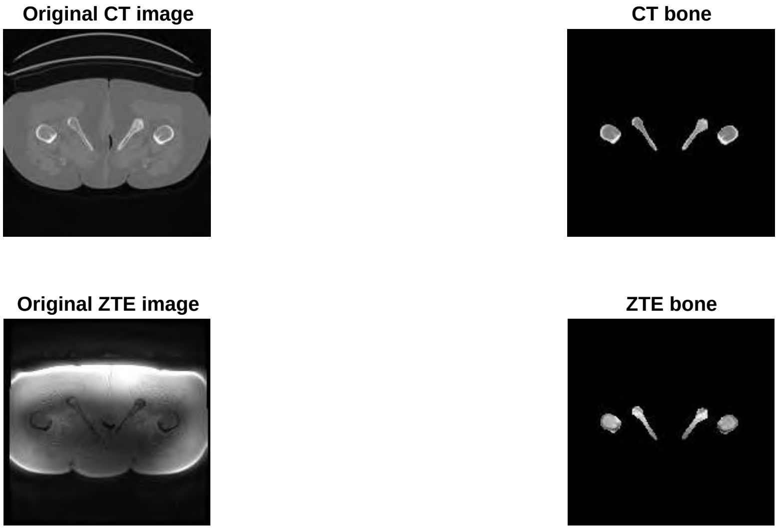

Original CT image

CT bone

Original ZTE image

ZTE bone

Figure 6.9: 2D monomodal image registration of bone masks.

Chapter 7

Pelvic ZTE bone segmentation

7.1 Introduction

In this chapter, the process of pelvic ZTE bone segmentation is described. First of all, two different bias field correction techniques are discussed and compared. Afterwards, an air mask is applied to the ZTE image. Thirdly, different segmentation strategies are considered and the results are presented. The goal is to obtain a mask that contains all the bone in the ZTE image.

7.2 Bias field correction

Image segmentation algorithms are based on the assumption that a uniform response is obtained in the entire FOV. Nevertheless, in MR images a spatially nonuniform bias is present due to sensitivity variation caused by the coil combination, RF transmit and receive non-uniformities and patient specific interactions. This can cause errors in image registration, segmentation, etc. In the past two decades, many bias field correction algorithms have been proposed. They can be categorized in prospective and retrospective methods. The prospective methods try to avoid intensity inhomogeneity during the acquisition process. These methods are of limited use, since they cannot correct for patient specific inhomogeneities. The retrospective methods on the other hand exclusively rely on information in the acquired image. In this thesis, two retrospective bias field correction techniques are applied and compared. The first one is multiplicative intrinsic component optimization, an energy minimization method for joint bias field estimation and segmentation of MR images. The second one is a histogram-based multiresolution correction technique. Both are described below and the results are presented.

7.2.1 Multiplicative intrinsic component optimization

The multiplicative intrinsic component optimization (MICO, [45]) decomposes the MR image into two multiplicative components: the bias field estimation and the true image. The bias field estimation and tissue segmentation is formulated as an energy minimization problem of seeking the optimal decomposition. In this method, the basic properties of both components are used. The true image is piecewise constant and the bias field is smoothly varying. The Matlab code for this method was downloaded from Mathworks (Copyright (c) 2016, Chunming Li, all rights reserved).

7.2.2 Multiresolution histogram-based intensity correction

In the histogram of the inverse log-scaled image, the soft-tissue peak is at low values and the noise peak is at high values. Signals from bone are smeared out in between these two peaks. The nonuniform bias causes the soft-tissue peak in the histogram to broaden, which can be seen in figure 7.2. When the histogram is taken from a small ROI (Region Of Interest) in the FOV, variation in the coil sensitivity profile is much less. Therefore, the soft-tissue peak is narrowed and the location of the signal can be located by the center of the peak. This observation led to a bias-correcting algorithm in two steps. First of all, the image dataset is divided into smaller 3D ROIs. Secondly, within each ROI, all pixels are normalized by the intensity of the soft-tissue peak. The algorithm is shown in figure 7.1. In the outer loop, the FOV is subsequently refined to smaller ROIs, starting from a ROI that covers the entire FOV. This is called a multiresolution approach. The inner loop shows the bias correction for one resolution. First of all, the FOV is divided in ROIs and the inverse log-scale image is obtained. Secondly, the soft-tissue peak is located. Only when sufficient signal statistics are present, the bias field in that ROI is updated. The bias factor $e^{-X(I)}$ is used since intensity $X(I)$ is log-scaled.

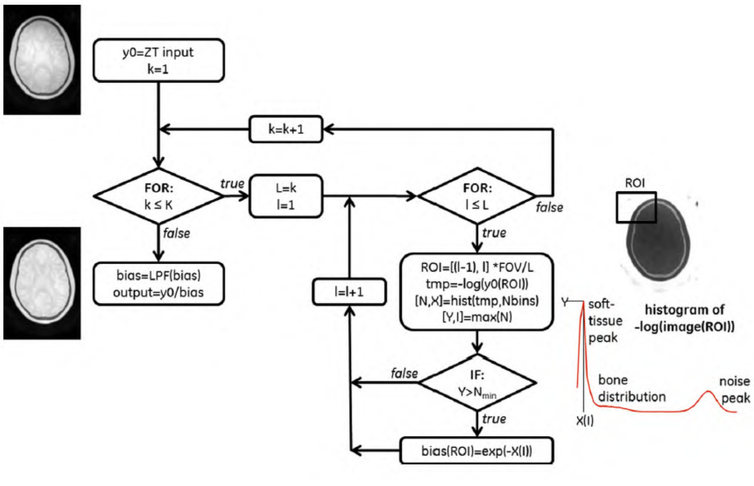

Figure 7.1: Schematic illustration of the histogram-based intensity correction, as explained in [19].

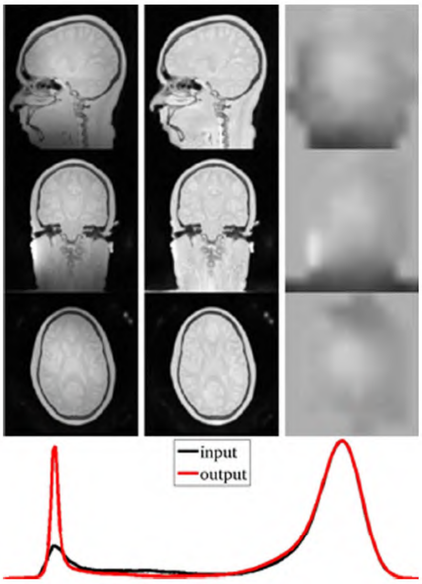

Figure 7.2: The uncorrected input image (left), the image after histogram-based bias correction (middle) and the corresponding bias field (right) for a ZTE image of the head. The histogram of the inverse log-scaled images shows how bias correction narrows the soft-tissue peak. [19].

This algorithm is implemented in Matlab and applied to ZTE hip images acquired at the PET/MR scanner in Leuven. In this algorithm, 4 parameters need to be chosen:

- K: Number of iterations in for loop. This parameter determines how small the ROIs get and is set to 20.
- g: The standard deviation of the Gaussian filter applied to smooth the bias field. g is set to 3.
- N_{fac}: This parameter is used to calculate the minimum number of pixels in the soft tissue peak. More specific: $= N_{min} = \frac{sizeROI}{N_{fac}}$. N_{fac} is set to 14.

The result can be seen in figure 7.3. It is clear that this algorithm results in an irregular signal in air regions. This is caused by the numerical instability of dividing small numbers by small numbers in regions where the intensity is zero or very close to zero. This problem is resolved by applying an air mask, as will be explained in the next section.

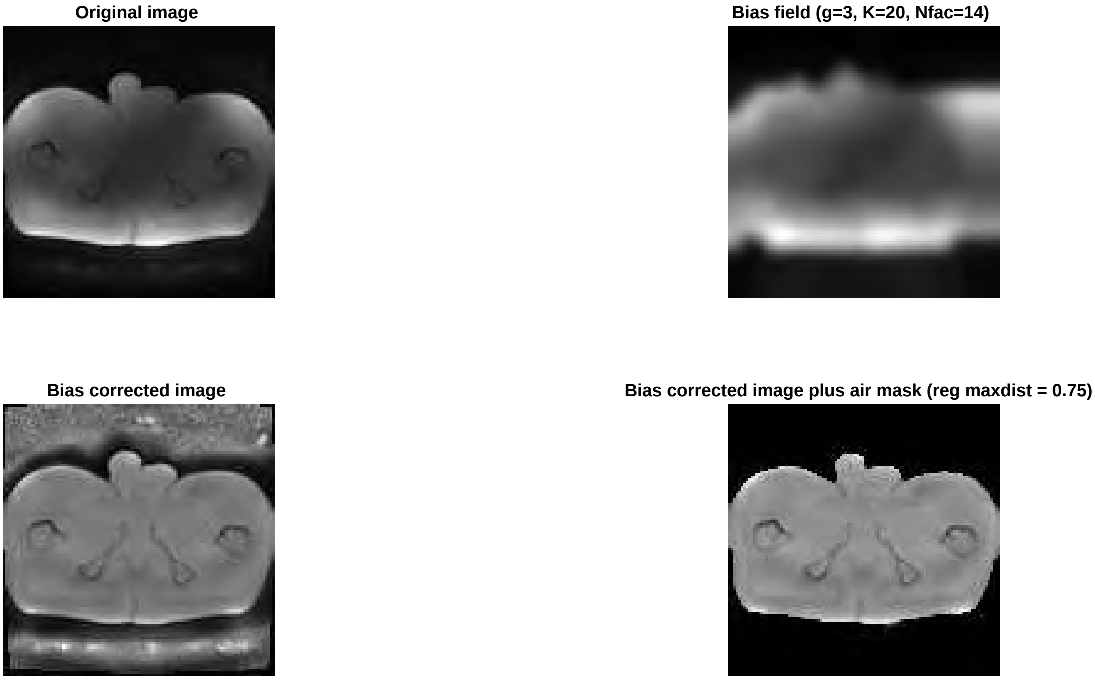

Figure 7.3: The bias field correction and air mask algorithm applied to a ZTE hip image.

7.2.3 Comparison

The two methods (MICO vs. multiresolution histogram-based intensity correction) are compared for two different ZTE images. The results are shown in figure 7.4 and 7.5. It is clear that the histogram-based method provides better results. In figure 7.6 and 7.7, it can be seen that applying the algorithm multiple times improves the result.

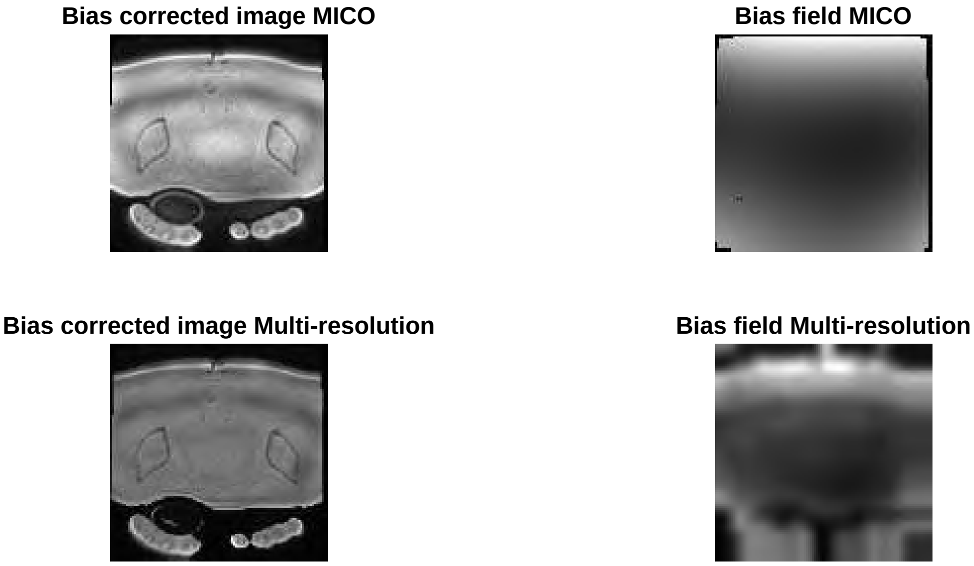
Bias corrected image MICO

Bias field MICO

Bias corrected image Multi-resolution

Bias field Multi-resolution

Figure 7.4: MICO and Multi-resolution bias correction compared.

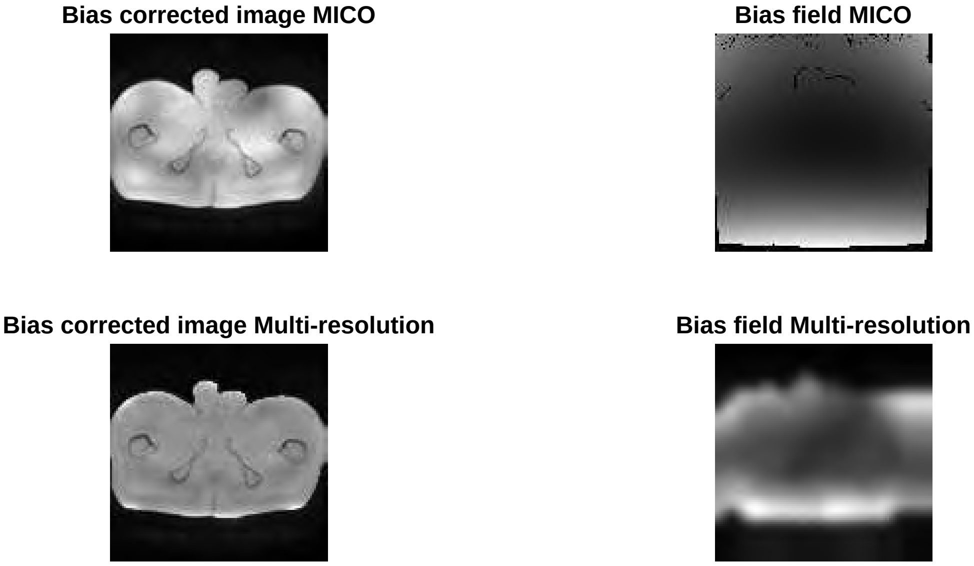
Bias corrected image MICO

Bias field MICO

Bias corrected image Multi-resolution

Bias field Multi-resolution

Figure 7.5: MICO and Multi-resolution bias correction compared.

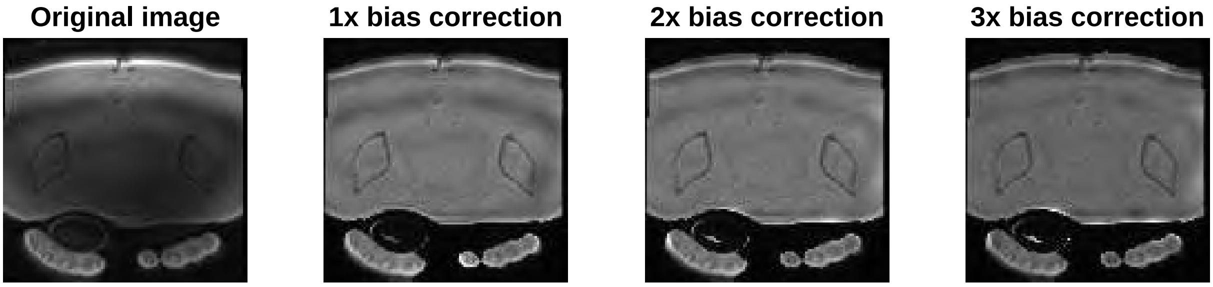

Figure 7.6: The effect of multiple bias-corrections.

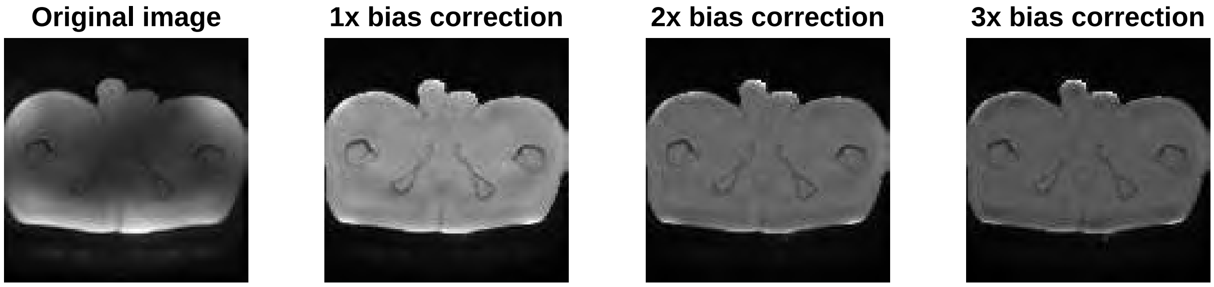

Figure 7.7: The effect of multiple bias-corrections.

7.3 Air mask

The air mask is calculated by growing a region based on the difference between the intensity of the new pixel and the mean of the region. The algorithm is started by choosing seed points. From each seed point, a region is grown. In the case of the ZTE hip images used in the previous section, two seed points are used: one in the upper left corner and one in the lower right corner, because these two points are air in every image of the dataset and the air region above and below the body are not connected. In every iteration step, all the neighboring pixels to the region are compared to the region. The pixel with the smallest difference in intensity is allocated to the region. The process stops when the intensity difference becomes larger than a specified threshold. This threshold (reg maxdist) is set to 0.2. The result of the region growing algorithm can be seen in figure 7.3.

7.4 Segmentation methods

7.4.1 Histogram-based segmentation (thresholding)

The most straightforward method to do segmentation is to apply thresholding on the ZTE image. Based on the histogram of the ZTE image, a threshold is chosen that separates bone tissue (with low intensity) from soft tissue (with high intensity). In [19], this leads to the result shown in figure 7.8. It is clear that in this image, it is possible to discriminate bone, air and soft tissue. Nevertheless, when this principle is applied to a ZTE image of the hip, this method does not work. This can be seen in figure 7.9. In this figure, a CT image is added to clearly see where the different tissue types are present. Air is present in the intestines. Thresholds are determined based on the histogram of the log inverted image. It can be seen that there are a lot of errors in the segmented image. Optimizing the threshold values can lead to a reduction of wrongly segmented pixels, but the overlap in intensities between soft tissue pixels and bone pixels is too large to accurately discriminate between these.

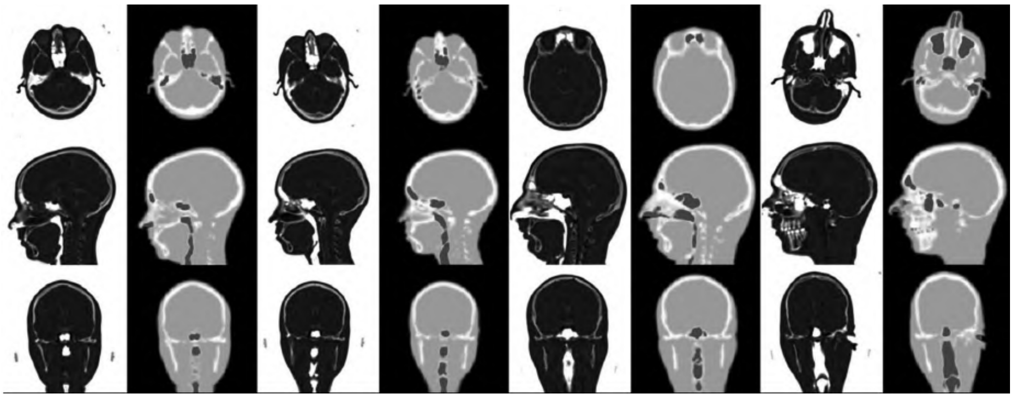

Figure 7.8: Illustration of histogram-based segmentation. [19].

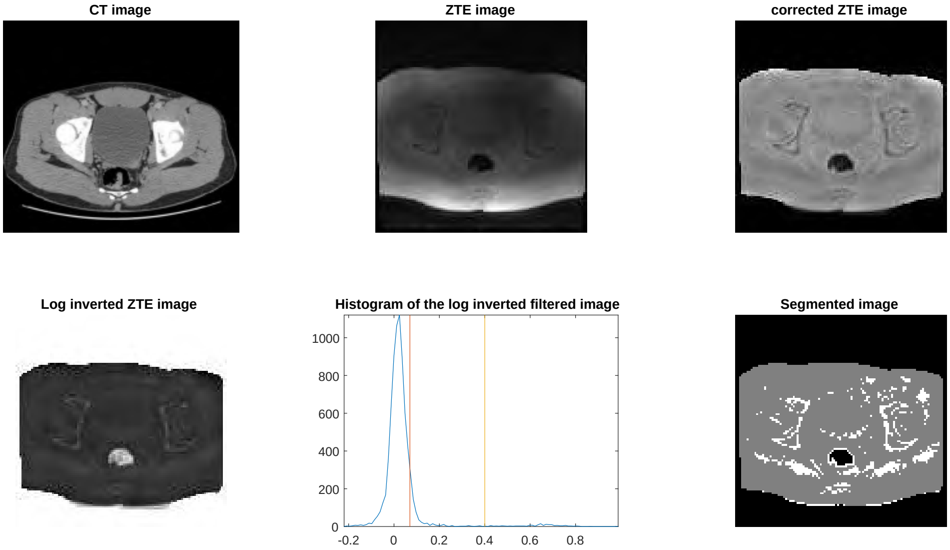

Figure 7.9: Thresholding applied on a ZTE image of the hip. A CT image from another person is added to show the air present in the intestines. The algorithm should therefore be able to discriminate this area of air from the bone. Thresholds are determined based on the histogram of the log inverted image. It can be seen that there are a lot of errors in the segmented image.

7.4.2 Thresholding after image enhancement

To facilitate the thresholding, several image enhancement techniques can be applied on the images. In this section, the same steps are followed as explained in section 4.5. In the top-hat morphological filtering step, a nonflat ball-shaped structuring element is used with radius 3 and maximum offset height 0.1. In the manual correction step, a contour is drawn that includes the bone segments. The result is shown in figure 7.10. It can be seen that there are a lot of errors in the segmented image. In this image, the algorithm is applied on a ZTE image with a resolution of 2.9 mm. For images with a resolution of 2 mm, the same conclusion can be drawn.

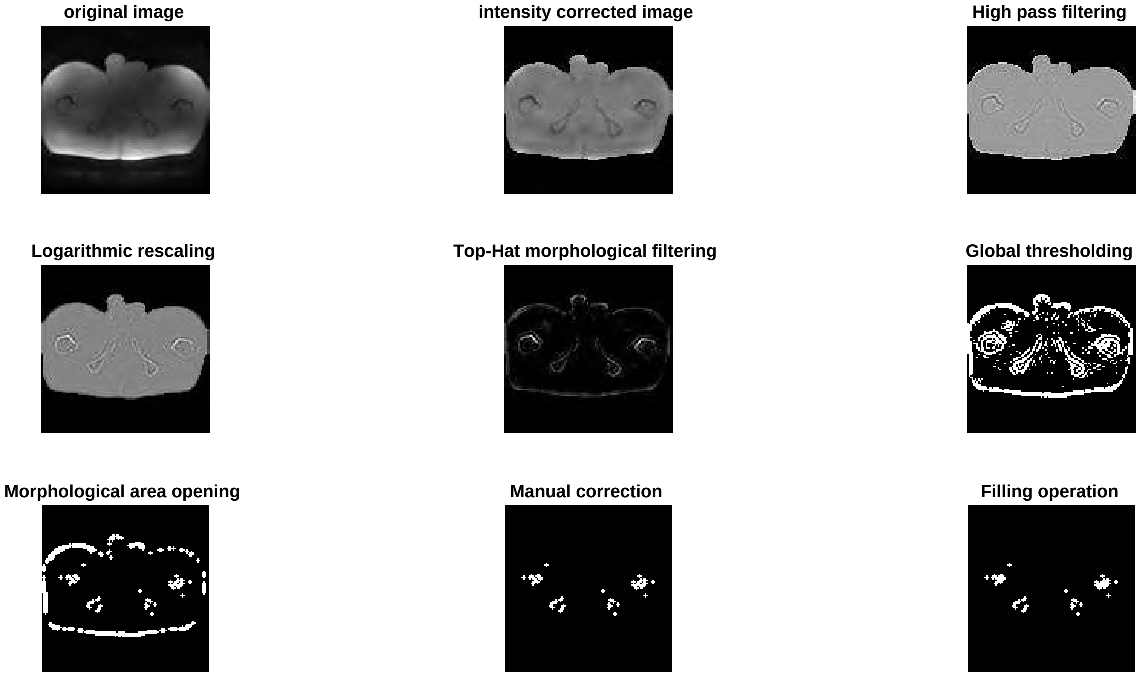

original image

intensity corrected image

High pass filtering

Logarithmic rescaling

Top-Hat morphological filtering

Global thresholding

Morphological area opening

Manual correction

Filling operation

Figure 7.10: Image enhancement and thresholding applied on a ZTE image of the hip. It can be seen that there are a lot of errors in the segmented image.

7.4.3 Markov

The use of Markov Random Fields for segmentation is included for completeness. The Matlab code is adapted from a download from unknown source. In figure 7.11, it can be seen that the algorithm is able to discriminate between bone, air and soft tissue when the image has sufficient contrast. When the algorithm is applied on ZTE images, the results were not good. This can be seen in figure 7.12.

Figure 7.11: Segmentation of a hip image ([46]) based on the hidden Markov random field model and its expectation-maximization algorithm.

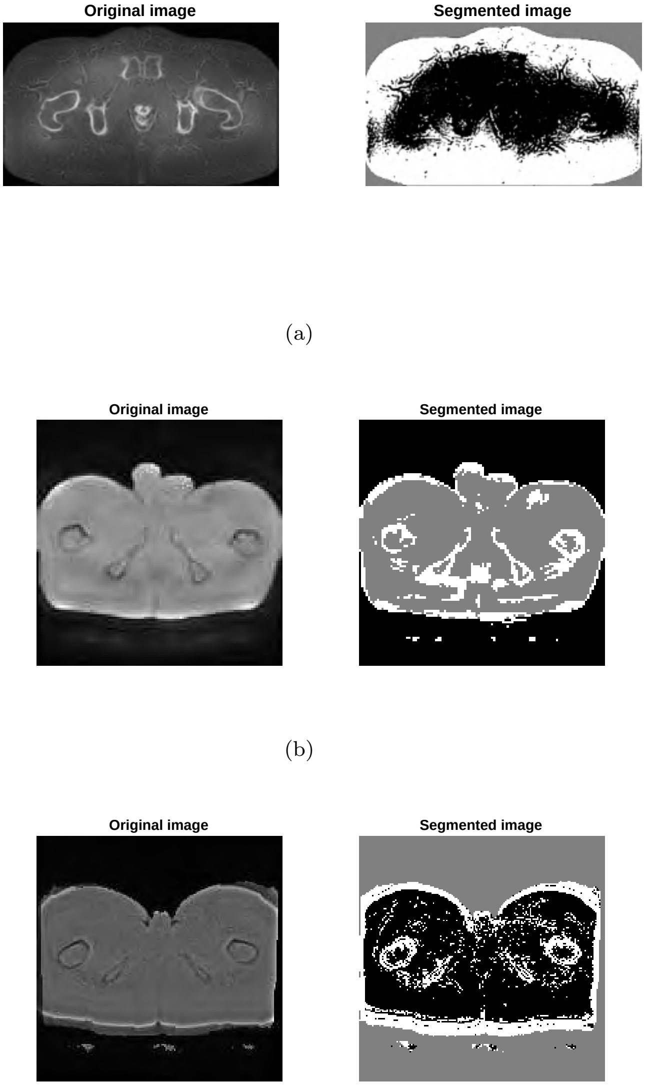

(a)

(b)

(c)

Figure 7.12: Markov segmentation applied on (a) log inverted ZTE of a human hip region, (b) ZTE of human hip region with a resolution of 2.9 mm, (c) ZTE of human hip region with a resolution of 2 mm.

7.4.4 Multiscale edge detection

In [47], a multiscale edge detection algorithm is proposed. This method combines the properties of edge- and region-based segmentation methods. Homogeneous regions are detected in the edge map derived from multi-resolution edge detection. Thresholding is applied to eliminate over-selected regions. In brain imaging, this method can be beneficial since the difference in gray level between white and gray matter is small. In hip ZTE imaging, the same is true for cortical bone and soft tissue. Therefore, a multi-resolution edge detection algorithm was implemented in Matlab based on the algorithm presented in this paper. In multi-resolution edge detection, the different edge images represent edges of different strength and accuracy. The smaller the scale, the more accurate the edges, but also the more sensitive the method is to noise. As edge detector, the Canny operator is used. This is the first derivative of the Gaussian and is a measure for the discontinuity. It is specified by its σ, the standard deviation of the Gaussian filter. The discontinuity measurement $T_{i,j}$ for image $f_{i,j}$ with size WxH and $i \in [1, W]$, $j \in [1, H]$ is:

$$T_{i,j} = G'_{\sigma_n}(f_{i,j}).$$

Based on the distribution of the discontinuity measurement, a threshold is selected. Pixels that have a discontinuity measurement higher than this threshold belong to an edge region, pixels with a discontinuity measurement below this threshold belong to a homogeneous region. The threshold therefore divides the image into 2 images: the edge map image and the homogeneous region map image. The threshold is chosen to be the peak of the distribution. This is shown in figure 7.13.

At the onset of the multi-resolution image decomposition, a candidate edge map image is obtained by using a small σ. In following steps, σ decreases, starting from a high value and based on the candidate edge map from step 1. The regions are recursively separated with a decreasing scale, meaning an increasing resolution. The result is shown in figure 7.14. Based on the finest edge map, segmentation can be applied using symmetry and similarity (see section 7.4.5). The result is shown in figure 7.15 and 7.16 for two different slices. It was concluded that the results are not better than the results using the methods described in section 7.4.5.

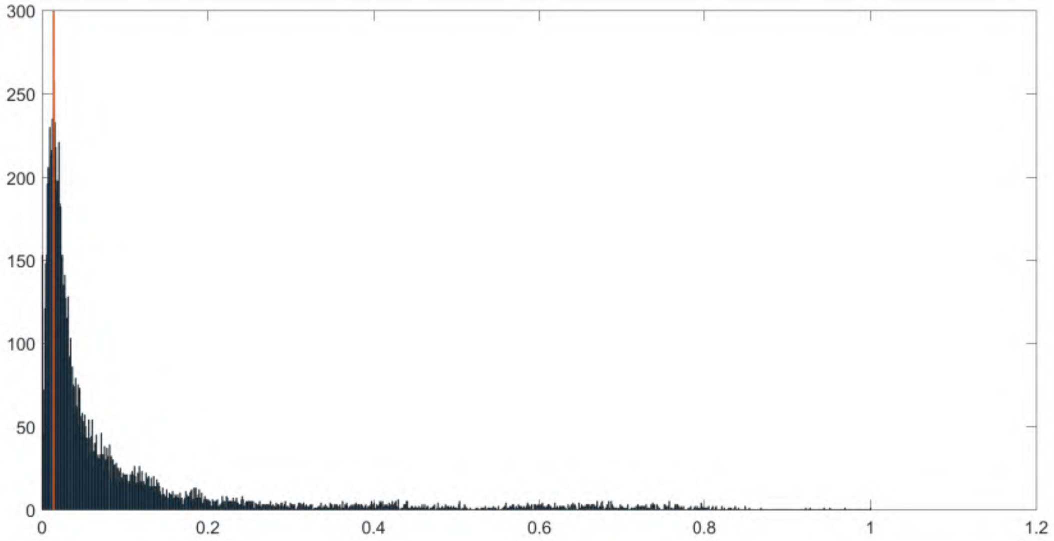

Figure 7.13: The distribution of the discontinuity measurement. The threshold is chosen to be at the peak of the distribution.

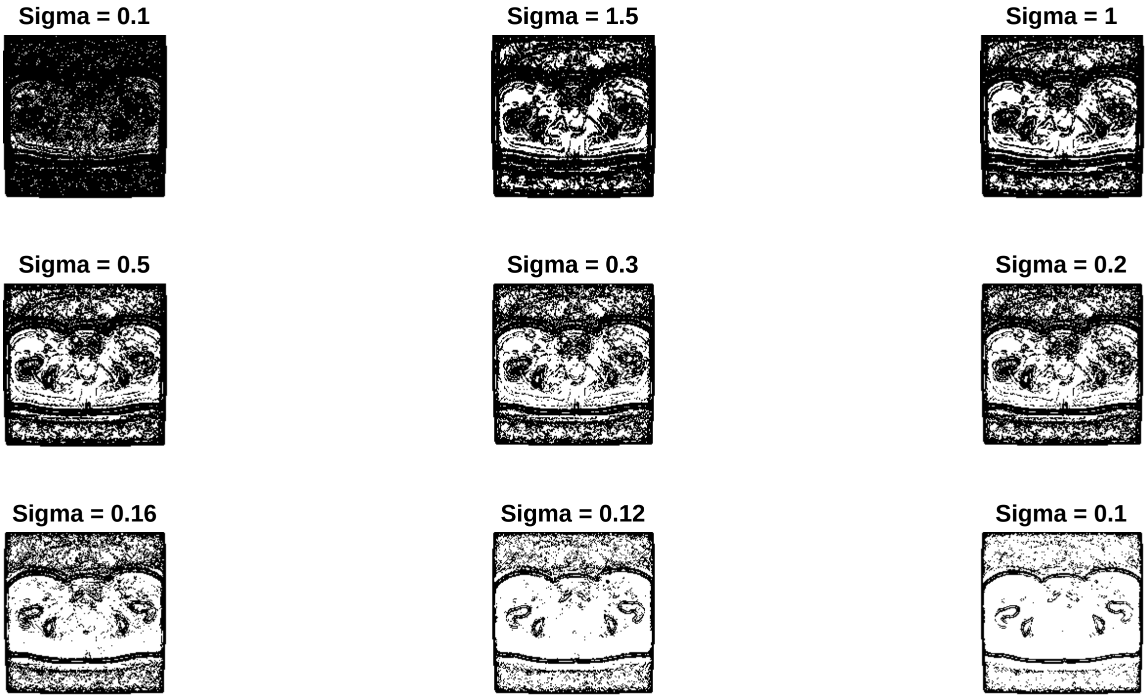

Figure 7.14: Multi-scale resolution representation of a ZTE hip image.

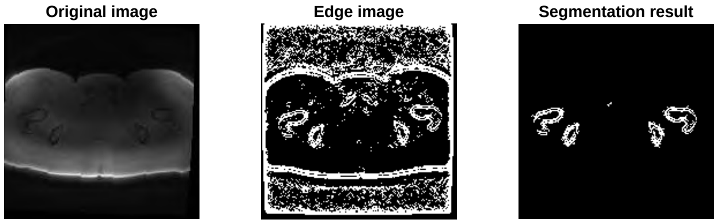

Figure 7.15: Segmentation based on a multi-scale edge approach for a ZTE hip image.

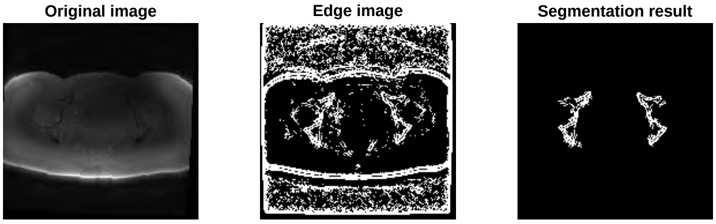

Figure 7.16: Segmentation based on a multi-scale edge approach for a ZTE hip image.

7.4.5 Symmetry- and similarity-based segmentation

One way to improve the thresholding algorithm, is to use symmetry and similarity measures. This idea is based on the fact that bone structures in general are symmetric while air cavities are not. The downside of this method is that asymmetric anatomical abnormalities will be classified as air instead of bone, which makes it less generally applicable. In [46], a method based on symmetry and similarity is proposed for generating a five-class attenuation map in the pelvic region. The different tissue types are cortical bone, air cavity, soft tissue, fat, and background air. In this paper, the used MR sequence is short echo time (STE). Spatial fuzzy c-means (SFCM) clustering is used to cluster the images into bone-air and soft tissue. Bone and air are classified in the same cluster, since both intensities are low. After clustering, the different objects are separated from each other. For each object in the bone-air cluster, symmetry and similarity are considered.

Symmetry

Since translation correction has been applied, the bone structures are symmetric along the midline. The objects are flipped in the left/right direction and the number of overlapping pixels between the flipped object and the other objects in the slice is calculated.

Similarity

Similarity can be used to improve object separation compared to only using symmetry. The similarity between two objects in the image can be measured by using the 2D cross-correlation index. Since the cross-correlation is independent on on the position of the objects, objects with similar shapes can be recognized regardless of symmetry. The similarity value (SV) is considered to be the peak of the 2D cross-correlation between 2 objects. In each slice, the maximum of SV is considered to be bone.

$$SV = max(C_{O1,O2}(i,j)) \tag{7.1}$$

Size

Since there are no small bone structures in the pelvis, the objects with a size smaller than a certain threshold are classified as not bone.

The algorithm is applied on the STE image used in [46]. In figure 7.17, it can be seen that this algorithm can cluster the different tissue types and can distinguish air from bone.

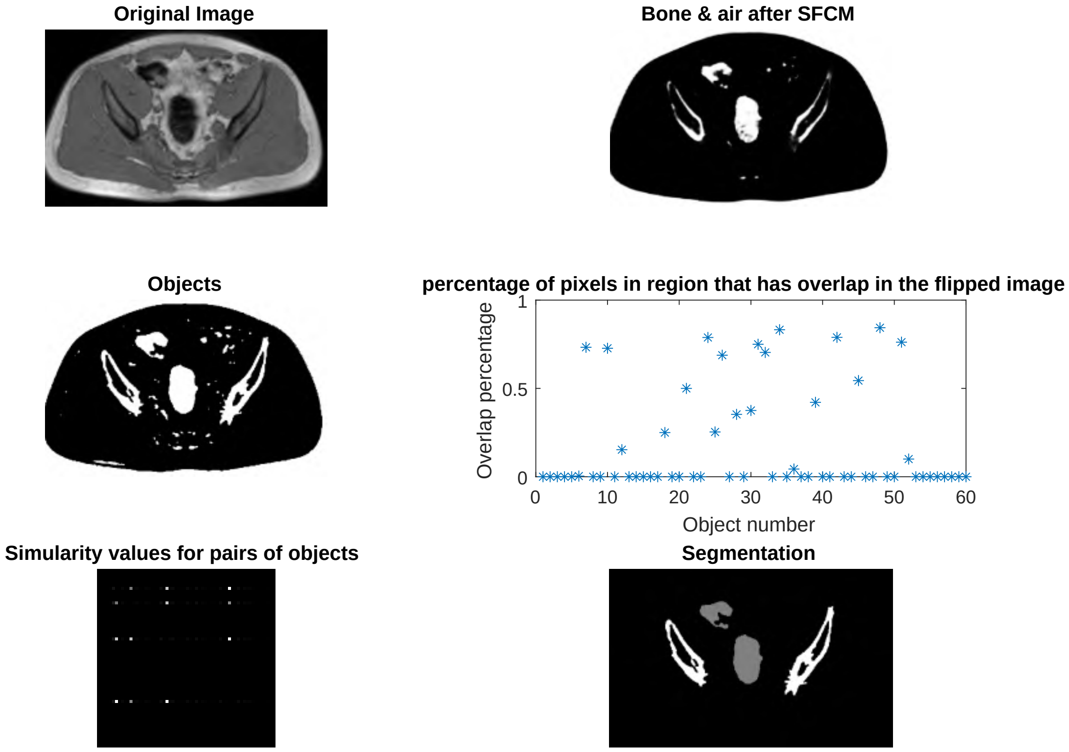

Figure 7.17: Symmetry- and simularity-based segmentation applied on an image of the pelvic region [46]. After SFCM, simularity and symmetry is calculated for every object in the bone-air cluster.

The same algorithm was applied on the ZTE image as well, but no good results were obtained. In figure 7.18, it can be seen that the cluster algorithm cannot clearly distinguish bone and air from soft tissue. Therefore, thresholding was applied instead of clustering. Two versions of an adapted algorithm were developed: one with 2D segmentation and one with 3D segmentation. Both are described below.

7.4.5.1 Version 1: 2D segmentation

A segmentation method is developed based on existing post-processing algorithms built-in in Matlab and the segmentation algorithm based on symmetry, similarity, size of objects and distance to edge. In this algorithm, segmentation is performed slice per slice. The different steps are described below.

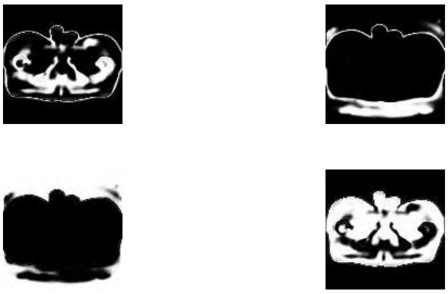

Figure 7.18: SFCM applied on the ZTE hip image.

Rotation and translation correction

Manual rotation and translation correction is applied.

Bias field correction and air mask

The bias field correction and air mask are performed as described in section 7.2 and 7.3.

Edge of body contour

The edge of the body contour is calculated in each slice by applying the built in Matlab function *edge* tot the air mask.

Image processing

A number of existing post-processing techniques are applied on the image. At first, the threshold to differentiate bone from soft tissue is automatically determined based on the histogram of the image. First, a Gaussian curve is fitted to the histogram. Next, the threshold is determined based on the maximum of the gaussian curve and the full width at half maximum. This is shown in figure 7.19. Thirdly, in each slice, the different objects are separated (connected component analysis) and the objects that are below a certain threshold size are removed. In a final step, morphological closing is applied, the gaps are filled with a maximum size gap of 5 pixels, followed by a filling operation.

Segmentation

The segmentation is done based on symmetry, similarity, size and the distance to the edge. This is done slice by slice. The distance to the edge is added since regions close to the edge are often wrongly segmented as bone.

The results are shown for three slices in figure 7.20, 7.21 and 7.22. It can be seen that the results are good for some slices, but in the third figure, the filling of the gaps between objects gives wrong results. Therefore, a second method was developed that does not fill gaps and includes 3D information.

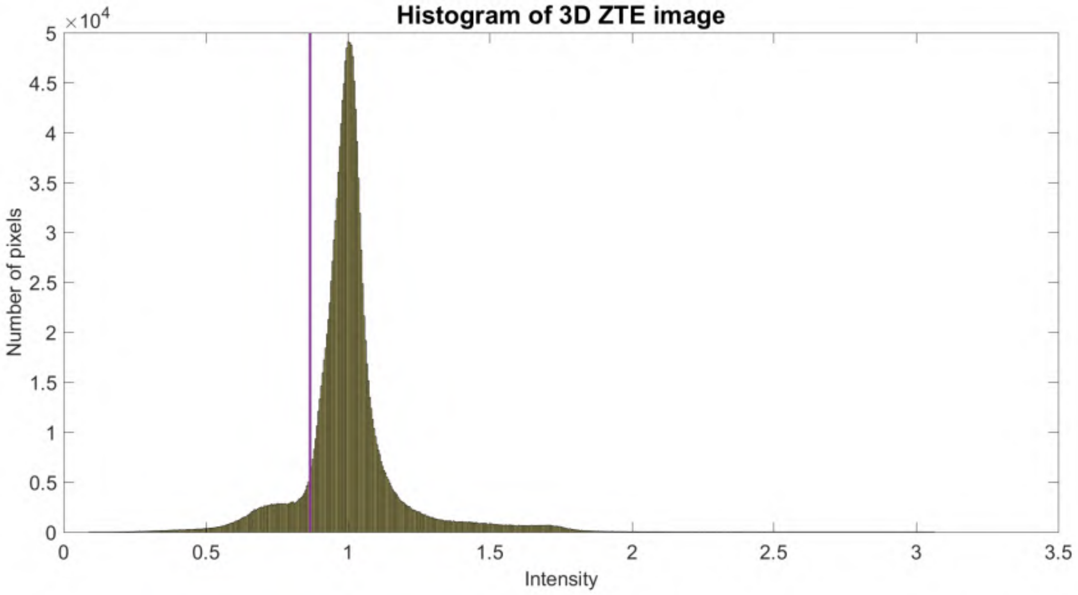

Figure 7.19: Histogram of a corrected 3D ZTE image. The threshold that separates bone from soft tissue is determined based on the Gaussian curve that is fitted to the histogram.

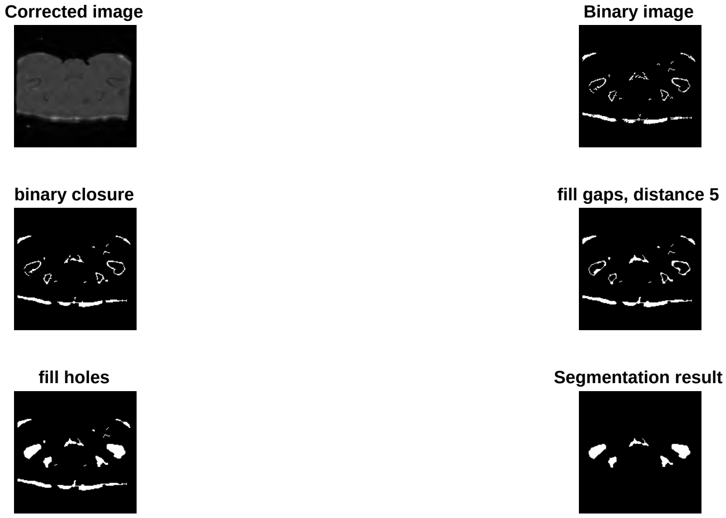

Figure 7.20: The first segmentation algorithm applied on one slice of the ZTE hip image.

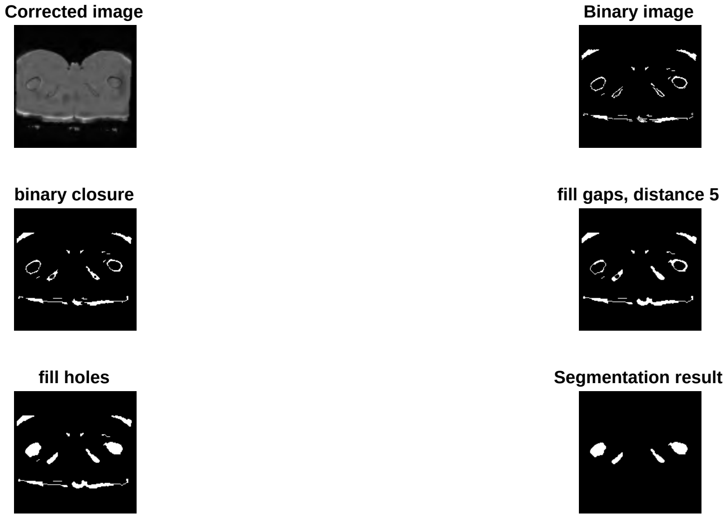

Figure 7.21: The first segmentation algorithm applied on one slice of the ZTE hip image.

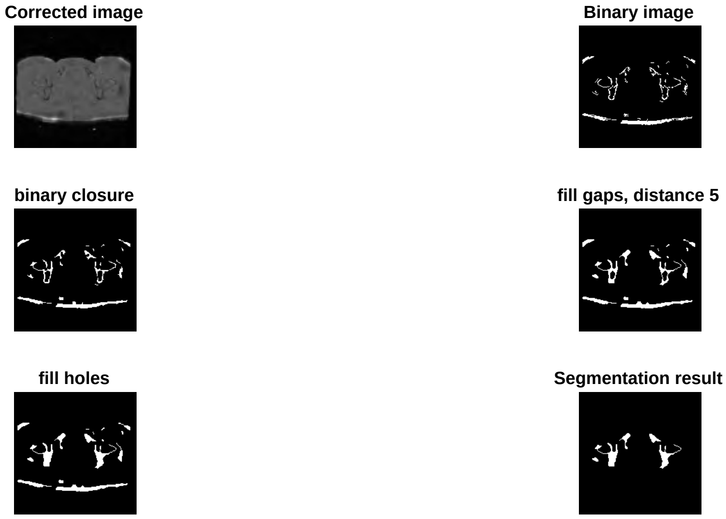

Figure 7.22: The first segmentation algorithm applied on one slice of the ZTE hip image.

7.4.5.2 Version 2: 3D segmentation

In the second version of the implemented symmetry- and similarity-based segmentation, no morphological closing and filling is applied and the connected component analysis is done in 3D, across the different slices. Another adaption to the first version is the bias field correction. It was noticed that dividing the image by a 2-D Gaussian filtered version of the image results in better elimination of unexpected dark or bright regions. This significantly improves the segmentation process, but low contrast between some bone components and soft tissue makes segmentation based on thresholding impossible. The standard deviation of the Gaussian filter is set to 3. In figure 7.23 and 7.24, most of the bony parts are segmented. In figure 7.25, two large bones are not correctly segmented as bone. The reason is the very low contrast between the bone and the soft tissue, which can be seen in figure 7.26.

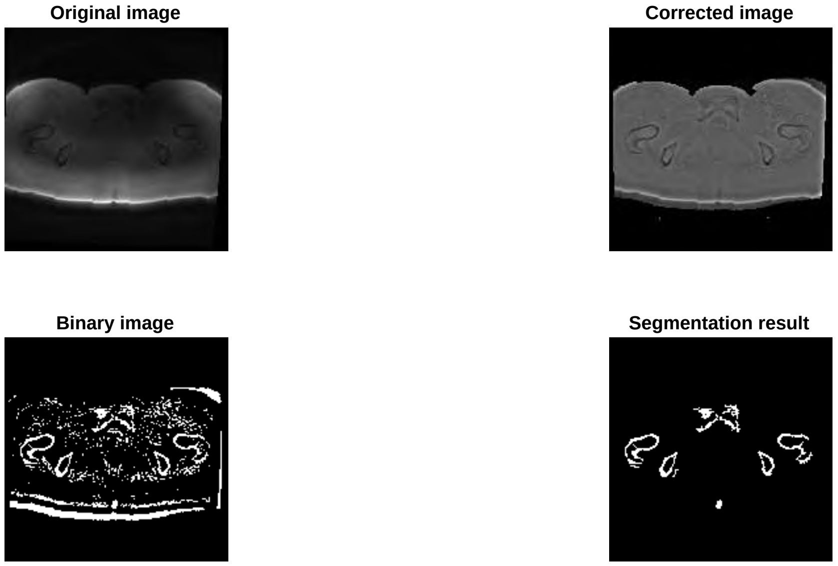

Figure 7.23: The second segmentation algorithm applied on one slice of the ZTE hip image.

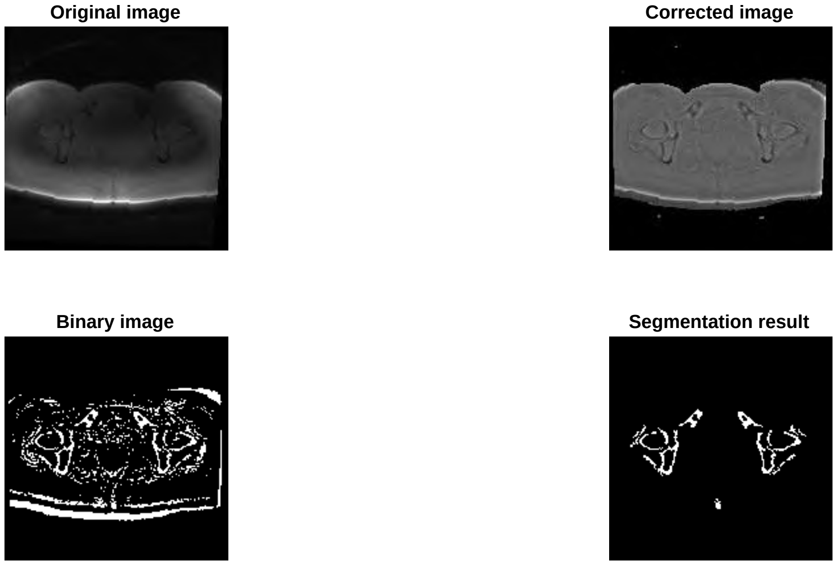

Figure 7.24: The second segmentation algorithm applied on one slice of the ZTE hip image.

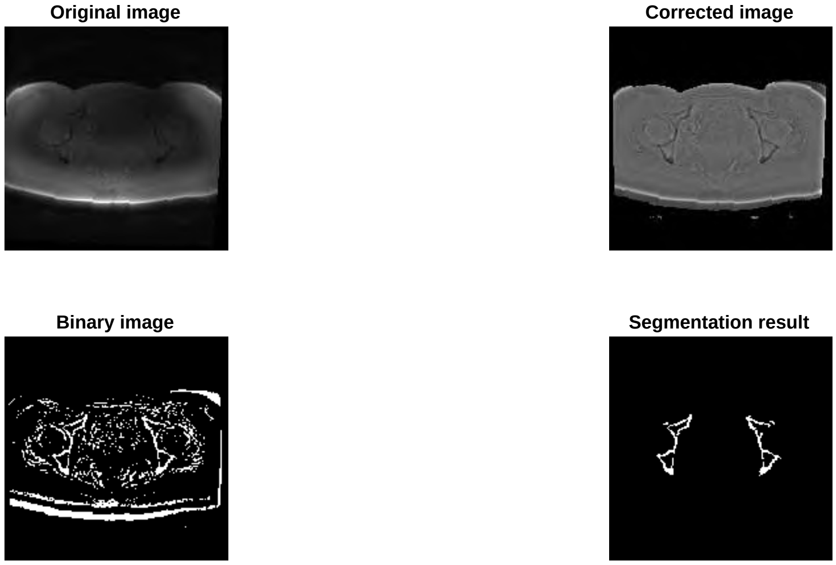

Figure 7.25: The second segmentation algorithm applied on one slice of the ZTE hip image.

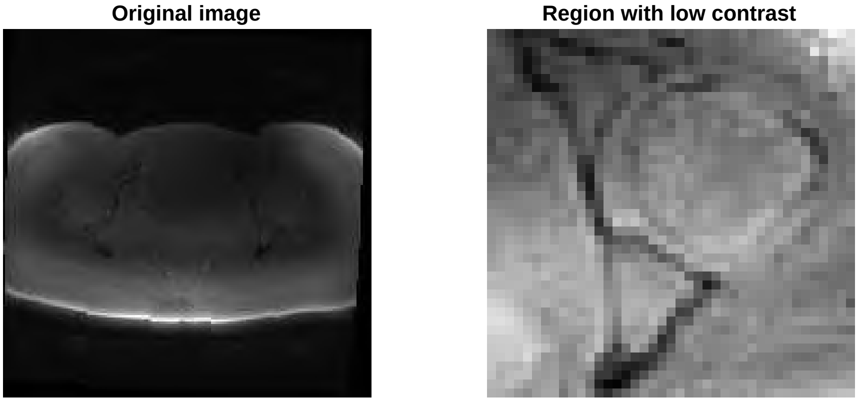

Figure 7.26: Close-up of a bone region with very low contrast.

7.4.6 Conclusion

It is concluded that the symmetry- and similarity-based method results in the best segmentation. Nevertheless, a lot of segmentation errors remain, since the ZTE sequence is developed for brain imaging only and some bone parts, like the head of the femur, are hardly visible on any of the acquired ZTE images. This problem has to be overcome before accurate segmentation of bone on pelvic ZTE images is possible.

Chapter 8

Case studies

8.1 Introduction

In this chapter, two case studies are discussed where MR images are used to obtain an attenuation map. The first case study is on a pig bone, the second case study is on one cervical patient. In both cases, a CT-based attenuation map is used as reference.

8.2 Hybrid ZTE/Dixon attenuation map of a pig bone

The first case study is on the use of MR images to obtain an attenuation map of a pig bone. The Dixon and ZTE images of a pig bone are used to obtain a hybrid ZTE/Dixon pseudo-CT. A CT-based attenuation map is used as reference. The Dixon pseudo-CT is obtained by calculating water-fat fractions and applying tissue-specific 511 keV attenuation coefficients. For the bone pixels, the pseudo-CT is obtained by determining a continuous two-segment piecewise linear model based on ZTE and CT intensities. A bilinear transformation is used to obtain a 511 keV attenuation map from the pseudo-CT. In general, the results obtained in this case study are a proof-of-principle and cannot be used directly to draw conclusions about the use of ZTE in human PET/MR imaging. First of all, the pig was dead for about a week when the images were made. This will lead to higher bone densities and different tissue properties. Secondly, a head coil was used instead of a body coil, which resulted in higher image quality. Finally, the limited size of the bone enabled ZTE images with higher resolution, which facilitated image processing.

8.2.1 Reference: CT-based attenuation map

When a CT image is obtained, the linear attenuation coefficient of the polychromatic x-ray bream is measured, expressed in HU. By definition, the CT system is calibrated so that water corresponds to 0 HU and air to -1000 HU. However, the physical meaning of other measured HU's is less well defined, since it strongly depends on the energy spectrum of the x-ray source. On the other hand, the photons emitted in PET imaging all have an energy of 511 keV.

Therefore, a bilinear transformation is needed to transform the CT image to a 511 keV linear attenuation map. In [48], it is concluded that the kVp setting strongly influences this transformation, while the difference between scanners is relatively insignificant.

The kVp-dependent transformation, appropriate for lung, soft tissue, and bone, is as follows:

$$\mu = 9.6 \cdot 10^{-5} \cdot (HU + 1000), HU < bp$$

$$\mu = a(HU + 1000) + b, HU > bp$$

Bp (breakpoint), a and b are kVp dependent values. Values below the breakpoint will correspond to soft tissue, values above the breakpoint will correspond to bone. For 120 kVp, the following values are used: $bp = 47HU$, $a = 5.10 \cdot 10^{-5} cm^{-1}$, $b = 4.71 \cdot 10^{-2} cm^{-1}$ [48]. The kVp-dependent bilinear transformation is shown in figure 8.1.

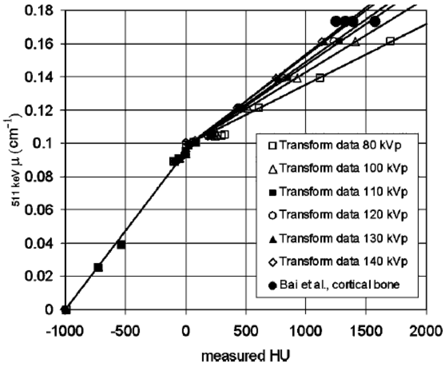

Figure 8.1: The known 511 keV linear attenuation values for the reference tissues as a function of the measured HU. [48]

8.2.2 Dixon based pseudoCT

To obtain a Dixon based pseudoCT, GE's LAVA-Flex sequence was used. This is a dual-echo Dixon-based 3D T1-weighted SPGR acquisition. An SPGR sequence (Spoiled Gradient Recalled Acquisition in Steady State) spoils the transverse steady state by semi-randomly changing the phase of the RF pulse, resulting primarily in T1 or PD contrast. By applying the LAVA-Flex sequence, a water image with water magnitudes M_w and a fat image with fat magnitudes M_f are obtained. From these, the water-fat fraction r can be calculated using following equation:

$$r = \frac{M_w - M_f}{M_f + M_w} \tag{8.1}$$

This fraction ranges continuously from -1 for purely adipose tissue to 1 for purely soft tissue. The attenuation coefficient for each voxel is calculated by:

$$\mu_r = \frac{1+r}{2} \cdot \mu_{soft} + \frac{1-r}{2} \cdot \mu_{adipose}$$

In this equation, μ_{soft} and $\mu_{adipose}$ are the tissue-specific linear attenuation coefficients extracted from literature. The following values are used: $\mu_{soft} = 0.1cm^{-1}$ [49] and $\mu_{adipose} = 0.09cm^{-1}$ [50] [51]. The result is shown in figure 8.2. Note that these attenuation coefficients are only valid for living human beings, and can therefore lead to wrong results when used on a dead pig bone.

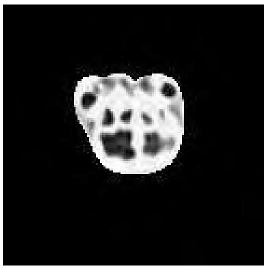

Figure 8.2: A pseudo-CT image of the bone obtained from a dual-echo Dixon-based acquisition.

8.2.3 ZTE based pseudoCT

8.2.3.1 Image registration

Multimodal affine 3D image registration of the ZTE and CT images was done in Matlab using the function $imregconfig$ and $imregtform$. Since the Dixon sequence is acquired the same day and the bone did not move in that time, the same geometric transformation can be applied to the Dixon images. The result is shown for one slice in figure 8.3. It can be concluded that the simple geometric form of the pig leg and the absence of movement leads to good registration results.

Figure 8.3: Result of the 3D registration process for ZTE and CT image for one slice.

8.2.3.2 Image segmentation

Bone was segmented from the ZTE image in a semi-automated fashion. Since there is no symmetry in the bone, the algorithm described in the previous chapter based on symmetry and similarity cannot be used. At first, a bandpass filter was applied. Secondly, a threshold was chosen manually to discriminate bone from soft tissue. Finally, small objects were removed and holes were filled. The segmentation result is not optimal, but sufficient.

8.2.3.3 Joint histogram

Based on the segmentation result, a bone window was applied on the ZTE and CT images. The joint histogram for bone pixels is shown in figure 8.4. It can be seen that some unexpected regions appear bright on the joint histogram (between 800 and 1000 HU). After investigation, it was clear that these pixels are mostly segmentation errors. An example of the pixels that appear in this region for one slice is shown in figure 8.5, where the wrongly segmented pixels are green. To eliminate the influence of these segmentation errors on further results, these regions in the joint histogram are cleared.

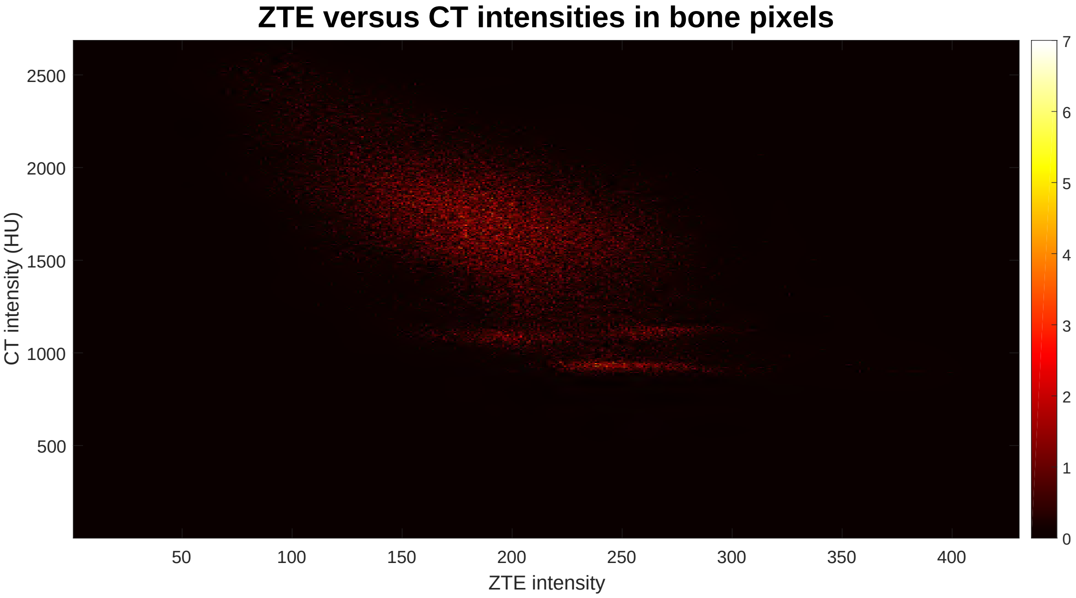

Figure 8.4: Joint histogram for bone pixels in ZTE and CT images.

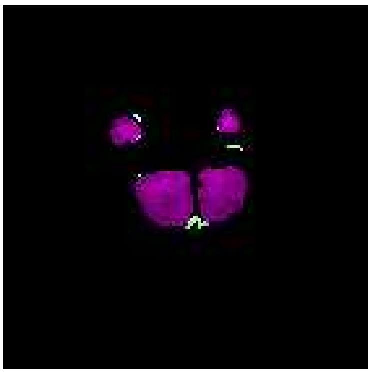

Figure 8.5: Segmentation errors in one slice leading to unexpected bright regions in the joint histogram.

8.2.3.4 Continuous two-segment piecewise linear model

The Shape Language Modelling toolkit (SLM) was used to fit a continuous two-segment piecewise linear model to the joint histogram. This toolbox uses least square splines, which offer a large flexibility to build a curve in any shape of form.

Density versus linear attenuation coefficient

Previous research has shown that the ZTE signal intensity in bone pixels is inversely proportional to the bone density. Since the HU of bone pixels is by definition above the breakpoint, the CT intensity of bone pixels is proportional to the 511 keV attenuation coefficient. Recall that the intensity of photons transmitted across some distance x is:

$$I = I_0 e^{-\mu x},$$

where μ is the linear attenuation coefficient, in cm^{-1}. μ is dependent on the density of a material and the probability of a photon being scattered or absorbed from the nucleus or an electron of one of the atoms present in the material. Therefore, μ can be split in two components:

$$\mu = \frac{\mu}{\rho} \cdot \rho,$$

where $\frac{\mu}{\rho}$ is the mass attenuation coefficient and ρ is the density. Bone consists of two types of material: cortical bone and spongious bone, with two different mass attenuation coefficients. It can be concluded that, since HU values in bone pixels are proportional to μ and ZTE values in bone are inversely proportional to ρ, a two-segment piecewise linear model needs to be used to fit the joint histogram. The two different pieces are explained by the two different mass attenuation coefficients for cortical and spongious bone. The two-segment piecewise linear model can be written as follows:

$$ZTEboneHU = \begin{cases} slope_1 \cdot ZTE + intercept_1, & \text{if ZTE} < \text{threshold.} \\ slope_2 \cdot ZTE + intercept_2, & \text{if ZTE} > \text{threshold.} \end{cases}$$

Results

The threshold between spongious bone and cortical bone was manually set to the intensity of 200 on the ZTE image. The knots are located at (51,2377), (200,1560) and (2430,780). The two slopes are -5.48 and -1.5 and the intercepts are 2657 and 1860 HU. The fit is shown in figure 8.6. This model is used to obtain a ZTE based pseudoCT for the bone pixels. The pseudo-CT image is then converted to linear attenuation coefficients (LAC) by using the bilinear model explained in section 8.2.1.

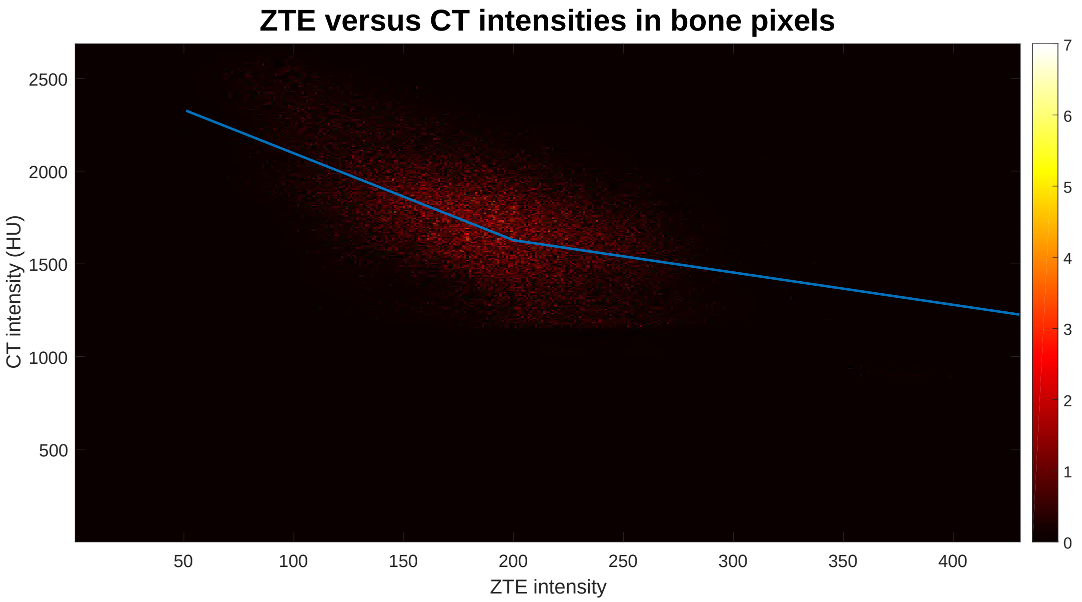

Figure 8.6: A continuous two-segment piecewise linear model is fitted to the joint histogram of the ZTE and the CT bone intensities.

8.2.4 Hybrid ZTE/Dixon attenuation map

The results from section 8.2.2 and 8.2.3 can be combined to obtain a hybrid Dixon/ZTE attenuation map. The ZTE based pseudo-CT is used to obtain the LAC of bone pixels, the Dixon-based pseudo-CT to obtain the LAC of non-bone pixels. The results are shown for one slice in figure 8.7. It is clear that the intensities of the MR-based attenuation map correspond to the intensities on the CT-based attenuation map for bone pixels, but not for soft-tissue pixels. This can be explained by the fact that the parameters used in equation 8.1 are for living humans and it cannot be assumed that these will hold for a bone of a dead pig. Therefore, a comparison between CT and MR-based attenuation maps is made only for the bone pixels. The RMSE is 12.864% and the mean of the errors is -1.66%. These errors are quite large compared to the RMSE of 4.64% and mean error of -1.22%, reported in [23]. This can be explained by the fact that in [23], 6 datasets of patients with pelvic lesions were used, which will result in more accurate fitting.

8.3 ZTE based pseudo-CT of the human pelvis

In this section, a ZTE based pseudo-CT of the human pelvis is obtained based on the dataset of one pelvic patient. Due to the limited amount of data available, the results are based on a preliminary study and cannot be used to draw general conclusions on the relation between ZTE and CT bone intensities.

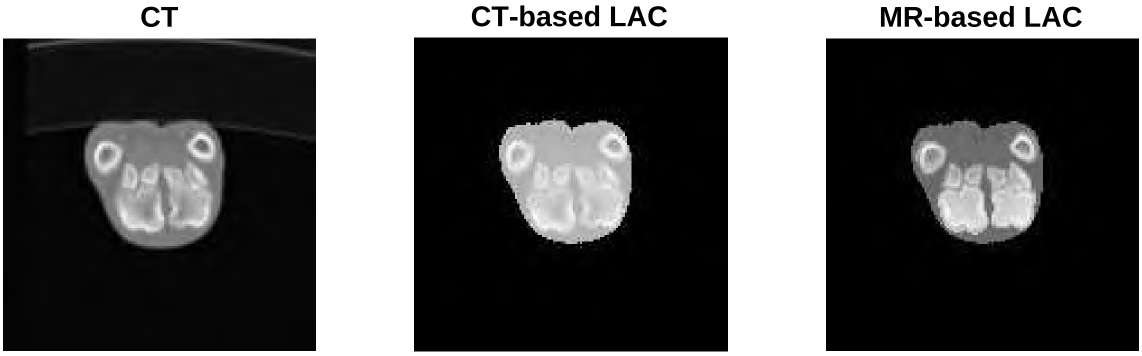

CT

CT-based LAC

MR-based LAC

Figure 8.7: The CT image, CT-based attenuation map, and MR-based attenuation map for one slice of a pig bone.

8.3.1 Results

As explained in chapter 6, 3D image registration of the ZTE and CT images was not possible. Therefore, 2D image registration is done on the bone masks of a subset of the slices. 31 slices were used to derive the relationship between ZTE and CT intensities. The ZTE-based pseudo-CT is obtained in a similar way as explained in the previous chapter. The fit is shown in figure 8.8. The two slopes are -6.133 and -1.434. The two intercepts are 2859 and 1919. Again, a comparison between CT and MR-based attenuation maps is made for the bone pixels. The LAC bone mask is shown for one slice in figure 8.9. The RMSE is 8.94% and the mean of the errors is -0.119%. As expected, these errors are quite large compared to the errors reported in [23], due to the limited set of slices the transformation is deducted from.

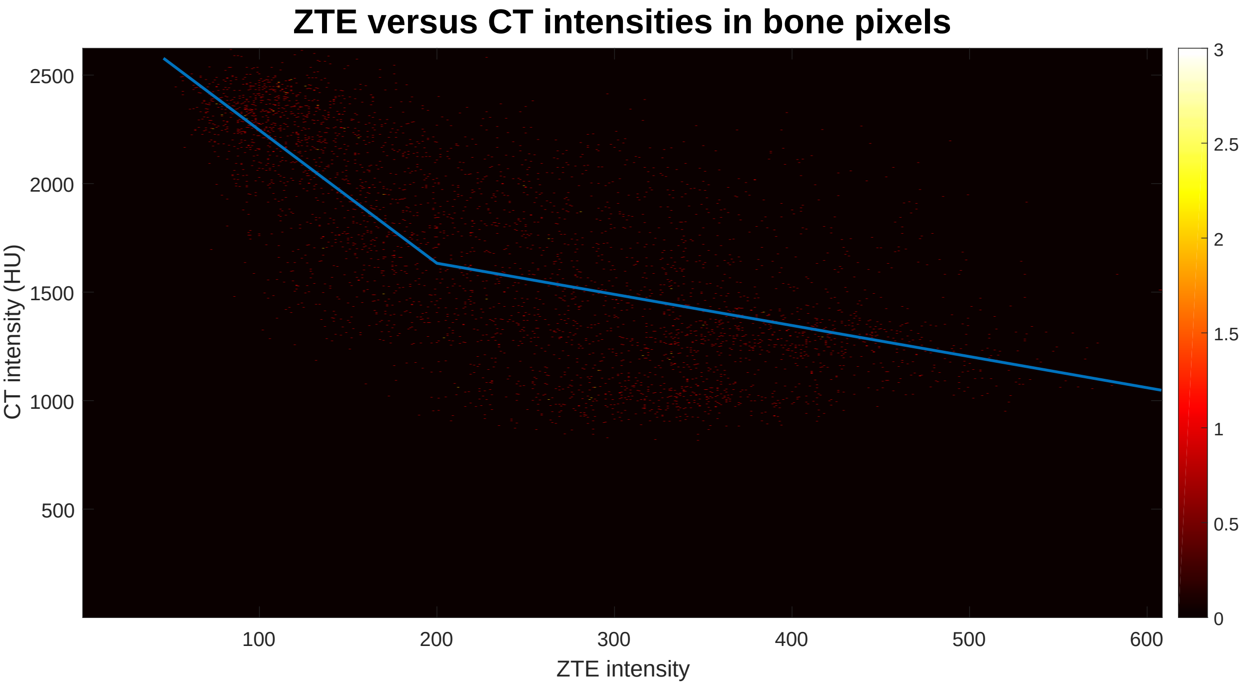

Figure 8.8: A continuous two-segment piecewise linear model is fitted to the joint histogram of the ZTE and the CT bone intensities.

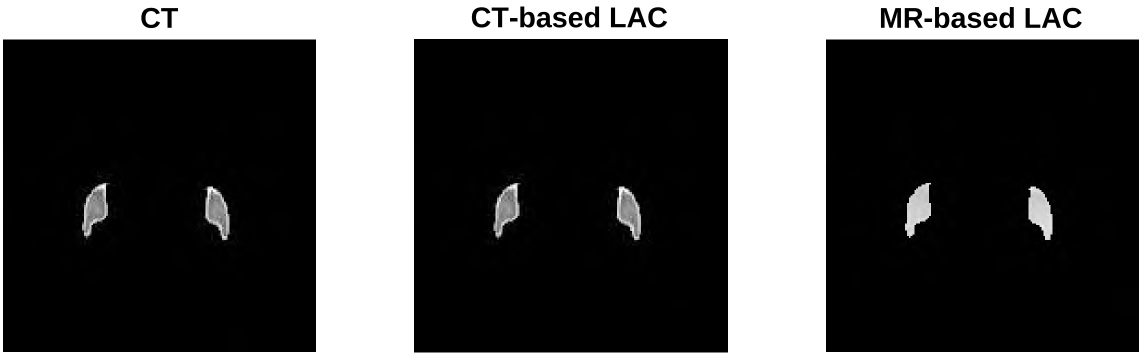

Figure 8.9: The LAC bone mask for one slice.

Chapter 9

Conclusion

We can conclude that the pelvic ZTE images obtained with the PET/MR scanner are of insufficient quality to do accurate bone segmentation. The best segmentation results were obtained by applying an algorithm based on the symmetry and similarity of bone structures in the pelvic region. In future work, other MR sequences which show potential for accurate bone segmentation could be investigated.

Secondly, we can conclude that the lack of accurate 3D image registration of the ZTE and CT images hampered the goal to obtain a ZTE based peudo-CT. In further work, this obstacle needs to be overcome by looking into more advanced image registration techniques or by facilitating the image registration by limiting the patient motion in between the two scans.

It is clear, however, that the bone intensity on the ZTE images is inversely proportional to the CT intensity and that a two-segment model can be fitted to the data. The first step in further work should be obtaining correct 3D image registration, so that an entire dataset of one patient can be used to calculate the best fit. The second step should be to normalize the ZTE data and add data of other patients. A larger patient study should be set up in collaboration with medical doctors in Leuven. This way, the two-segment model that is obtained in [23] can be verified.

Once the transformation to obtain a pseudo-CT image from MR data is derived, it should be verified by calculating the RMSE based on reconstructed PET images from MR-based and CT-based attenuation maps. This has already been done in [23], but should be verified.

The transformation can then be applied to PET/MR data without the need of reference CT data. Traditionally, intensities on an MR image are dependent on factors intrinsic to the tissue and the specifics of the experiment. Due to this non-quantitative nature of MR imaging, calibration is needed before converting a new ZTE dataset to bone density for AC purposes. One option is to include phantoms with known density in the field-of-view to obtain a calibration function.

It can be concluded that the use of the ZTE sequence can result in more accurate attenuation maps, and therefore shows a lot of potential for implementation in PET/MR pelvic imaging. Nevertheless, the sequence that is currently used in the university hospital in Leuven is optimized for brain imaging only and provides insufficient image quality when used in the pelvic region. Further collaboration with GE is needed in order to obtain good image quality to further investigate the full potential of the ZTE sequence and pelvic PET/MR imaging.

Bibliography

[1] Pieter Mollet. *Transmission-Based Attenuation Correction for Time-of-Flight Positron Emission Tomography.* PhD thesis, University of Ghent, 2014.

[2] S Vandenberghe, E Mikhaylova, E D'Hoe, P Mollet, and JS Karp. Recent developments in time-of-flight pet. *EJNMMI physics*, 3(1):1, 2016.

[3] Vincent Keereman. *MRI-based attenuation correction for emission tomography.* PhD thesis, University of Ghent, 2012.

[4] Donald W McRobbie, Elizabeth A Moore, Martin J Graves, and Martin R Prince. *MRI from Picture to Proton.* Cambridge university press, 2007.

[5] Alexander Drzezga, Michael Souvatzoglou, Matthias Eiber, Ambros J Beer, Sebastian Fürst, Axel Martinez-Möller, Stephan G Nekolla, Sibylle Ziegler, Carl Ganter, Ernst J Rummeny, et al. First clinical experience with integrated whole-body pet/mr: comparison to pet/ct in patients with oncologic diagnoses. *Journal of Nuclear Medicine*, 53(6):845–855, 2012.

[6] Stefaan Vandenberghe and Paul K Marsden. Pet-mri: a review of challenges and solutions in the development of integrated multimodality imaging. *Physics in medicine and biology*, 60(4):R115, 2015.

[7] Michel Defrise, Ahmadreza Rezaei, and Johan Nuyts. Time-of-flight pet data determine the attenuation sinogram up to a constant. *Physics in medicine and biology*, 57(4):885, 2012.

[8] Flemming Littrup Andersen, Claes Nøhr Ladefoged, Thomas Beyer, Sune Høgild Keller, Adam Espe Hansen, Liselotte Højgaard, Andreas Kjær, Ian Law, and Søren Holm. Combined pet/mr imaging in neurology: Mr-based attenuation correction implies a strong spatial bias when ignoring bone. *Neuroimage*, 84:206–216, 2014.

[9] Matthias Eiber, Axel Martinez-Möller, Michael Souvatzoglou, Konstantin Holzapfel, Anja Pickhard, Dennys Löffelbein, Ivan Santi, Ernst J Rummeny, Sibylle Ziegler, Markus Schwaiger, et al. Value of a dixon-based mr/pet attenuation correction sequence for the localization and evaluation of pet-positive lesions. *European journal of nuclear medicine and molecular imaging*, 38(9):1691–1701, 2011.

[10] Axel Martinez-Möller, Michael Souvatzoglou, Gaspar Delso, Ralph A Bundschuh, Christophe Chefd'hotel, Sibylle I Ziegler, Nassir Navab,

Markus Schwaiger, and Stephan G Nekolla. Tissue classification as a potential approach for attenuation correction in whole-body pet/mri: evaluation with pet/ct data. *Journal of nuclear medicine*, 50(4):520–526, 2009.

[11] Andrei Samarin, Cyrill Burger, Scott D Wollenweber, David W Crook, Irene A Burger, Daniel T Schmid, Gustav K von Schulthess, and Felix P Kuhn. Pet/mr imaging of bone lesions–implications for pet quantification from imperfect attenuation correction. *European journal of nuclear medicine and molecular imaging*, 39(7):1154–1160, 2012.

[12] Ilja Bezrukov, Frédéric Mantlik, Holger Schmidt, Bernhard Schölkopf, and Bernd J Pichler. Mr-based pet attenuation correction for pet/mr imaging. In *Seminars in nuclear medicine*, volume 43, pages 45–59. Elsevier, 2013.

[13] Gaspar Delso, Axel Martinez-Möller, Ralph A Bundschuh, Stephan G Nekolla, and Sibylle I Ziegler. The effect of limited mr field of view in mr/pet attenuation correction. *Medical physics*, 37(6):2804–2812, 2010.

[14] Johan Nuyts, Girish Bal, Frank Kehren, Matthias Fenchel, Christian Michel, and Charles Watson. Completion of a truncated attenuation image from the attenuated pet emission data. *IEEE transactions on medical imaging*, 32(2):237–246, 2013.

[15] Harry R Marshall, Frank S Prato, Lela Deans, Jean Théberge, R Terry Thompson, and Robert Z Stodilka. Variable lung density consideration in attenuation correction of whole-body pet/mri. *Journal of Nuclear Medicine*, 53(6):977–984, 2012.

[16] Paul J Schleyer, Tobias Schaeffter, and Paul K Marsden. The effect of inaccurate bone attenuation coefficient and segmentation on reconstructed pet images. *Nuclear medicine communications*, 31(8):708–716, 2010.

[17] Bernard D Coombs, Jerzy Szumowski, and William Coshow. Two-point dixon technique for water-fat signal decomposition with b0 inhomogeneity correction. *Magnetic resonance in medicine*, 38(6):884–889, 1997.

[18] Axel Martinez-Möller, Michael Souvatzoglou, Gaspar Delso, Ralph A Bundschuh, Christophe Chefd'hotel, Sibylle I Ziegler, Nassir Navab, Markus Schwaiger, and Stephan G Nekolla. Tissue classification as a potential approach for attenuation correction in whole-body pet/mri: evaluation with pet/ct data. *Journal of nuclear medicine*, 50(4):520–526, 2009.

[19] Florian Wiesinger, Laura I Sacolick, Anne Menini, Sandeep S Kaushik, Sangtae Ahn, Patrick Veit-Haibach, Gaspar Delso, and Dattesh D Shanbhag. Zero te mr bone imaging in the head. *Magnetic resonance in medicine*, 75(1):107–114, 2016.

[20] Peder EZ Larson, Misung Han, Roland Krug, Angela Jakary, Sarah J Nelson, Daniel B Vigneron, Roland G Henry, Graeme McKinnon, and Douglas AC Kelley. Ultrashort echo time and zero echo time mri at 7t. *Magnetic Resonance Materials in Physics, Biology and Medicine*, pages 1–12, 2015.

[21] Tetsuro Sekine, Edwin EGW ter Voert, Geoffrey Warnock, Alfred Buck, Martin W Huellner, Patrick Veit-Haibach, and Gaspar Delso. Clinical evaluation of zte attenuation correction for brain fdg-pet/mr imaging—comparison with atlas attenuation correction. *Journal of Nuclear Medicine*, pages jnumed–116, 2016.

[22] C Huang, J Ouyang, TG Reese, Y Wu, G El Fakhri, and JL Ackerman. Continuous mr bone density measurement using water-and fat-suppressed projection imaging (waspi) for pet attenuation correction in pet-mr. *Physics in medicine and biology*, 60(20):N369, 2015.

[23] Andrew P Leynes, Jaewon Yang, Dattesh D Shanbhag, Sandeep S Kaushik, Youngho Seo, Thomas A Hope, Florian Wiesinger, and Peder EZ Larson. Hybrid zte/dixon mr-based attenuation correction for quantitative uptake estimation of pelvic lesions in pet/mri. *Medical Physics*, 2017.

[24] Gaspar Delso, Florian Wiesinger, Laura I Sacolick, Sandeep S Kaushik, Dattesh D Shanbhag, Martin Hüllner, and Patrick Veit-Haibach. Clinical evaluation of zero-echo-time mr imaging for the segmentation of the skull. *Journal of Nuclear Medicine*, 56(3):417–422, 2015.

[25] J Ferlay, E Steliarova-Foucher, J Lortet-Tieulent, Sonia Rosso, JWW Coebergh, H Comber, David Forman, and Freddie Bray. Cancer incidence and mortality patterns in europe: estimates for 40 countries in 2012. *European journal of cancer*, 49(6):1374–1403, 2013.

[26] Stephen J Freedland, Joseph C Presti, Christopher L Amling, Christopher J Kane, William J Aronson, Frederick Dorey, Martha K Terris, SEARCH Database Study Group, et al. Time trends in biochemical recurrence after radical prostatectomy: results of the search database. *Urology*, 61(4):736–741, 2003.

[27] Derek B Chism, Alexandra L Hanlon, Eric M Horwitz, Steven J Feigenberg, and Alan Pollack. A comparison of the single and double factor high-risk models for risk assignment of prostate cancer treated with 3d conformal radiotherapy. *International Journal of Radiation Oncology* Biology* Physics*, 59(2):380–385, 2004.

[28] Bernd Joachim Krause, Michael Souvatzoglou, and Uwe Treiber. Imaging of prostate cancer with pet/ct and radioactively labeled choline derivates. In *Urologic Oncology: Seminars and Original Investigations*, volume 31, pages 427–435. Elsevier, 2013.

[29] Michael Souvatzoglou, Matthias Eiber, Axel Martinez-Moeller, Sebastian Fürst, Konstantin Holzapfel, Tobias Maurer, Sibylle Ziegler, Stephan Nekolla, Markus Schwaiger, and Ambros J Beer. Pet/mr in prostate cancer: technical aspects and potential diagnostic value. *European journal of nuclear medicine and molecular imaging*, 40(1):79–88, 2013.

[30] Nicolas Barry Delongchamps, Mathieu Rouanne, Thierry Flam, Frédéric Beuvon, Mathieu Liberatore, Marc Zerbib, and François Cornud. Multiparametric magnetic resonance imaging for the detection and localization of prostate cancer: combination of t2-weighted, dynamic contrast-

enhanced and diffusion-weighted imaging. *BJU international*, 107(9):1411–1418, 2011.

[31] Darko Pucar, Amita Shukla-Dave, Hedvig Hricak, Chaya S Moskowitz, Kentaro Kuroiwa, Semra Olgac, Lanie E Ebora, Peter T Scardino, Jason A Koutcher, and Kristen L Zakian. Prostate cancer: Correlation of mr imaging and mr spectroscopy with pathologic findings after radiation therapy–initial experience 1. *Radiology*, 236(2):545–553, 2005.

[32] Michael Souvatzoglou, Matthias Eiber, Toshiki Takei, Sebastian Fürst, Tobias Maurer, Florian Gaertner, Hans Geinitz, Alexander Drzezga, Sibylle Ziegler, Stephan G Nekolla, et al. Comparison of integrated whole-body [11c] choline pet/mr with pet/ct in patients with prostate cancer. *European journal of nuclear medicine and molecular imaging*, 40(10):1486–1499, 2013.

[33] Hyunjin Park, David Wood, Hero Hussain, Charles R Meyer, Rajal B Shah, Timothy D Johnson, Thomas Chenevert, and Morand Piert. Introducing parametric fusion pet/mri of primary prostate cancer. *Journal of Nuclear Medicine*, 53(4):546–551, 2012.

[34] Ivan Jambor, Ronald Borra, Jukka Kemppainen, Virva Lepomäki, Riitta Parkkola, Kirsti Dean, Kalle Alanen, Eveliina Arponen, Martti Nurmi, Hannu J Aronen, et al. Improved detection of localized prostate cancer using co-registered mri and 11 c-acetate pet/ct. *European journal of radiology*, 81(11):2966–2972, 2012.

[35] Leonardo Pace, Emanuele Nicolai, Marco Aiello, Onofrio Antonio Catalano, and Marco Salvatore. Whole-body pet/mri in oncology: current status and clinical applications. *Clinical and Translational Imaging*, 1(1):31–44, 2013.

[36] A Afshar-Oromieh, A Malcher, M Eder, M Eisenhut, HG Linhart, BA Hadaschik, T Holland-Letz, FL Giesel, C Kratochwil, S Haufe, et al. Pet imaging with a [68ga] gallium-labelled psma ligand for the diagnosis of prostate cancer: biodistribution in humans and first evaluation of tumour lesions. *European journal of nuclear medicine and molecular imaging*, 40(4):486–495, 2013.

[37] A Afshar-Oromieh, U Haberkorn, HP Schlemmer, M Fenchel, M Eder, M Eisenhut, BA Hadaschik, A Kopp-Schneider, and M Röthke. Comparison of pet/ct and pet/mri hybrid systems using a 68ga-labelled psma ligand for the diagnosis of recurrent prostate cancer: initial experience. *European journal of nuclear medicine and molecular imaging*, 41(5):887–897, 2014.

[38] Axel Wetter, Christine Lipponer, Felix Nensa, Karsten Beiderwellen, Tobias Olbricht, Herbert Rübben, Andreas Bockisch, Thomas Schlosser, Till A Heusner, and Thomas C Lauenstein. Simultaneous 18f choline positron emission tomography/magnetic resonance imaging of the prostate: initial results. *Investigative radiology*, 48(5):256–262, 2013.

[39] Susanna I Lee, Onofrio A Catalano, and Farrokh Dehdashti. Evaluation of gynecologic cancer with mr imaging, 18f-fdg pet/ct, and pet/mr imaging. *Journal of Nuclear Medicine*, 56(3):436–443, 2015.

[40] TW Yong, ZZ Yuan, Z Jun, Z Lin, WZ He, and Z Juanqi. Sensitivity of pet/mr images in liver metastases from colorectal carcinoma. *Hellenic journal of nuclear medicine*, 14(3):264–268, 2010.

[41] Graham M Treece, Andrew H Gee, PM Mayhew, and KES Poole. High resolution cortical bone thickness measurement from clinical ct data. *Medical image analysis*, 14(3):276–290, 2010.

[42] Graham M Treece, KES Poole, and Andrew H Gee. Imaging the femoral cortex: thickness, density and mass from clinical ct. *Medical image analysis*, 16(5):952–965, 2012.

[43] Hima Patel, Karthik Gurumoorthy, and Seshadri Thiruvenkadam. Automatic determination of anatomical correspondences for multimodal field of view correction. In *German Conference on Pattern Recognition*, pages 432–442. Springer, 2014.

[44] B Srinivasa Reddy and Biswanath N Chatterji. An fft-based technique for translation, rotation, and scale-invariant image registration. *IEEE transactions on image processing*, 5(8):1266–1271, 1996.

[45] Chunming Li, John C Gore, and Christos Davatzikos. Multiplicative intrinsic component optimization (mico) for mri bias field estimation and tissue segmentation. *Magnetic resonance imaging*, 32(7):913–923, 2014.

[46] M Shirin Shandiz, H Saligheh Rad, P Ghafarian, M Bakhshayesh Karam, Afshin Akbarzadeh, and Mohammad Reza Ay. Mr-guided attenuation map for prostate pet-mri: an intensity and morphologic-based segmentation approach for generating a five-class attenuation map in pelvic region. *Annals of Nuclear Medicine*, 31(1):29–39, 2017.

[47] H Tang, EX Wu, QY Ma, D Gallagher, GM Perera, and T Zhuang. Mri brain image segmentation by multi-resolution edge detection and region selection. *Computerized Medical Imaging and Graphics*, 24(6):349–357, 2000.

[48] Jonathan PJ Carney, David W Townsend, Vitaliy Rappoport, and Bernard Bendriem. Method for transforming ct images for attenuation correction in pet/ct imaging. *Medical physics*, 33(4):976–983, 2006.

[49] A Catana, A Van Der Kouwe, T Benner, M Hamm, C Michel, B Fischl, M Schmand, BR Rosen, and AG Sorensen. Is accurate bone segmentation required for mr-based pet attenuation correction. In *Proc Intl Soc Mag Reson Med*, volume 17, page 593, 2009.

[50] Thomas Beyer, PE Kinahan, DW Townsend, and D Sashin. The use of x-ray ct for attenuation correction of pet data. In *Nuclear Science Symposium and Medical Imaging Conference, 1994., 1994 IEEE Conference Record*, volume 4, pages 1573–1577. IEEE, 1994.

[51] Yannick Berker, Jochen Franke, André Salomon, Moritz Palmowski, Henk CW Donker, Yavuz Temur, Felix M Mottaghy, Christiane Kuhl, David Izquierdo-Garcia, Zahi A Fayad, et al. Mri-based attenuation correction for hybrid pet/mri systems: a 4-class tissue segmentation technique using a combined ultrashort-echo-time/dixon mri sequence. *Journal of nuclear medicine*, 53(5):796–804, 2012.